WASY Software

FEFLOW®

Finite Element Subsurface Flow
& Transport Simulation System

White Papers
Vol. II

WASY GmbH
Institute for
Water Resources Planning
and Systems Research

WASY GmbH Institute for Water Resources Planning and Systems Research,
Waltersdorfer Straße 105, D-12526 Berlin, Germany
Phone: +49-30-67 99 98-0, Fax: +49-30-67 99 98-99
E-Mail: mail@wasy.de

Contents

Contents

Variable-density flow and transport in porous media: approaches and challenges

1

H.-J. G. Diersch[a] **& O. Kolditz**[b]

[a]*WASY Institute for Water Resources Planning and Systems Research, Berlin, Germany*
[b]*University of Tübingen, Center of Applied Geosciences, Germany*

Abstract
We review the state of the art in modeling of variable-density flow and transport in porous media, including conceptual models for convection systems, governing balance equations, phenomenological laws, constitutive relations for fluid density and viscosity, and numerical methods for solving the resulting nonlinear multifield problems. The discussion of numerical methods addresses strategies for solving the coupled spatio-temporal convection process, consistent velocity approximation, and error-based mesh adaptation techniques. As numerical models for those nonlinear systems must be carefully verified in appropriate tests, we discuss weaknesses and inconsistencies of current model-verification methods as well as benchmark solutions. We give examples of field-related applications to illustrate specific challenges of further research, where heterogeneities and large scales are important.

Keywords: porous media; balance equations; phenomenological laws; constitutive relations; variable density; brine transport; saltwater intrusion; convection; thermohaline flow; fingering; Rayleigh number; instability; numerical simulation; finite element methods; adaptive methods; benchmarking;

Notation

Roman letters

$\boldsymbol{a}$		continuum state variable vector;
a	1	shape coefficient;
B		buoyancy or Turner number;
b	L	aperture;
C	$L^{1/2}T^{-1}$	Chezy roughness coefficient;
Cr		Courant number;
c	$L^2T^{-2}\Theta^{-1}$	specific heat capacity;
$\boldsymbol{D}$	L^2T^{-1}	tensor of hydrodynamic dispersion;
D	L^2T^{-1}	diffusivity;
D		dimension of problem (1,2,3);
D_d	L^2T^{-1}	coefficient of molecular diffusion;
$\boldsymbol{D}_m$	L^2T^{-1}	tensor of mechanical dispersion;
$\boldsymbol{D}_m^*$	L^2T^{-1}	modified $\boldsymbol{D}_m$;
D_s	L^2T^{-1}	saline diffusivity;
$\boldsymbol{D}_\lambda$	$ML^{-2}T^{-1}\Theta$	Soret coupling tensor;
$\boldsymbol{D}_\lambda^*$	$ML^{-2}T^{-1}\Theta$	modified $\boldsymbol{D}_\lambda$;
D_λ	L^2T^{-1}	thermal diffusivity;
$\boldsymbol{d}$	T^{-1}	strain-rate tensor;
d	L	thickness or height;

E	L^2T^{-2}	internal (thermal) energy density;
$\boldsymbol{e}$		error vector;
$\boldsymbol{F}$	$ML^{-2}T^{-2}$	interfacial drag term of momentum exchange;
$\boldsymbol{F}_f$	$ML^{-2}T^{-2}$	surface friction (viscous shear) term;
$\boldsymbol{f}$		generalized flux vector;
$\boldsymbol{g}$	LT^{-2}	external body force (e.g., gravity);
g	LT^{-2}	gravitational acceleration $\|\boldsymbol{g}\|$;
H	$ML^{-1}T^{-2}$	integral function of the gravity term;
H_e	$ML^{-1}T^{-3}$	energy (heat) sink/source term;
h	L	representative element length;
h_e	L^2T^{-2}	enthalpy;
$\boldsymbol{I}$	1	unit vector;
$\boldsymbol{J}$		Jacobian matrix;
$\Im_F$	$L^{-1}T$	Forchheimer coefficient;
$\Im_H$	$M^{-1}L^2T$	non-Fickian HC dispersion coefficient;
$\boldsymbol{j}_k$	$ML^{-2}T^{-1}$	nonadvective species flux;
$\boldsymbol{j}_e$	MT^{-3}	nonadvective energy (heat) flux;
K	LT^{-1}	effective hydraulic conductivity;
$\boldsymbol{k}$	L^2	porous medium permeability tensor;
k	L^2	isotropic permeability coefficient;
k_r	1	relative permeability;
L		partial differential equation operator;
Le		Lewis number;
l		mesh level;
M		number of phases;
M	$L^{1/3}T^{-1}$	Manning roughness coefficient;
m		nodal point;
N		number of chemical species;
N	1	finite element basis (shape) function;
NE, NE_2		number of elements of the whole and the half domain, respectively;
NN, NN_2		number of nodes of the whole and the half domain, respectively;
Pe		mesh (grid) Peclet number;
p	$ML^{-1}T^{-2}$	pressure;
p_c	$ML^{-1}T^{-2}$	capillary pressure;
Q	$ML^{-3}T^{-1}$	sink/source term;
Q_{EB}	$ML^{-3}T^{-1}$	extended Boussinesq approximation term;
Q_k	$ML^{-3}T^{-1}$	sink/source term of species k;
$\boldsymbol{q}$	LT^{-1}	Darcy velocity;
R	L	radius of tube;
$\Re^D$		D-dimensional Euclidean space;
R_k	$ML^{-3}T^{-1}$	chemical reaction rate of species k;
Ra		Rayleigh number;
r	L	hydraulic radius;
S	$L^2T^{-2}\Theta^{-1}$	entropy density;
s	1	saturation in the void space ε;
$\boldsymbol{T}$	1	porous medium tortuosity tensor;
T	Θ	temperature;
t	T	time;
t_D	1	dimensionless time;
$\boldsymbol{v}$	LT^{-1}	macroscopic phase (pore) velocity;
v	LT^{-1}	magnitude of vector $\boldsymbol{v}$;
w		weighting (test) function;
$\boldsymbol{x}$	L	spatial coordinate vector;
z	L	vertical coordinate;

Greek letters

α	1	solutal expansion coefficient;
β	Θ^{-1}	thermal expansion constant;
$\beta(T)$	Θ^{-1}	variable thermal expansion function;
β_L, β_T	L	longitudinal and transverse disper-

		sivity, respectively;
γ	L^{-1}	fluid compressibility;
δ		convergence criterion;
Δ		increment or difference;
ε	1	porosity, void space;
ε^{α}	1	volume fraction of α -phase;
ζ	1	local coordinate;
η	1	local coordinate;
$\bar{\eta}$	1	global error criterion;
$\bar{\eta}_e$	1	local error criterion;
ϑ		friction exponent;
θ		weighting coefficient;
κ		upwind parameter;
Λ	$MLT^{-3}\Theta^{-1}$	hydrodynamic thermodispersion tensor;
Λ_c	$MLT^{-3}\Theta^{-1}$	conductive part of the thermo-dispersion tensor;
Λ_d	L^4T^{-3}	Dufour coupling tensor;
Λ_m	$MLT^{-3}\Theta^{-1}$	mechanical part of the thermo-dispersion tensor;
λ	$MLT^{-3}\Theta^{-1}$	thermal conductivity;
μ	$ML^{-1}T^{-1}$	dynamic viscosity;
μ_k	L^2T^{-2}	chemical potential of species *k*;
ξ	1	local coordinate;
ρ	ML^{-3}	density function;
ρ_k	ML^{-3}	density of species *k*;
σ	$ML^{-1}T^{-2}$	viscous stress tensor;
σ'	$ML^{-1}T^{-2}$	deviatoric stress tensor;
ς	1	normalized temperature;
Υ	L^{-1}	coefficient of skeleton compressibility;
τ		generalized friction factor;
υ	$M^{-1}L^3$	specific volume $1/\rho$;
χ	T^{-1}	eigenvalue;
ω_k	1	mass fraction of species *k*;
Ω		domain;
$\partial\Omega$		boundary of the domain Ω ;
$\partial_x, \partial_y, \partial_z$		partial differentiation with respect to *x*, *y*, *z*, respectively;
∇	L^{-1}	Nabla (vector) operator;

Subscripts

c	conductive, capillary or critical;
d	dispersive;
e	energy or elemental;
k	species indicator;
λ	thermal;
m	mechanical;
m	nodal point;
n	time level;
0	reference;
p	predictor;
s	solutal;
τ	iteration number;

Superscripts

a	advective
α	phase indicator;
d	dispersive;
g	gas phase;
l	liquid phase;
n	time level;
s	solid phase;
T	transpose;

Abbreviations

AB/TR	Adams-Bashforth/trapezoid rule scheme;
AMR	adaptive mesh refinement;
BE	backward Euler;
BTD	balancing tensor diffusivity;
CFL	Courant-Friedrichs-Lewy condition;
DBF	Darcy-Brinkman-Forchheimer flow model;
DDC	double diffusive (thermohaline) convection;
EOS	equations of state;
ENO	essentially-non-oscillatory method;
FE/BE	forward Euler/backward Euler scheme;
FEM	finite element method;
FCT	flux-corrected-transport scheme;
FVM	finite volume method;
HC	high-concentration;
HDR	hot dry rock;
HRL	Horton-Rogers-Lapwood problem;
MOC	method of characteristics;
MMOC	modified method of characteristics;
OB	Oberbeck-Boussinesq approximation;
ODE	ordinary differential equation;
PGLS	Petrov-Galerkin least square method;
REV	representative elementary volume;
RHS	right-hand side;
RMS	root-mean square;
TR	trapezoid rule;
TVD	total-variation-diminishing method;

1.1 Introduction

In continuum fluid mechanics a fluid (or a fluid phase) is considered as an effectively continuous medium with a *density* ρ (fluid mass per unit volume of fluid) as a fundamental bulk property. The density of a fluid is often not uniform. In general, the fluid is composed of N miscible chemical species with a partial density ρ_k (mass of the constituent k per unit volume of fluid), so that for the mixture $\rho = \sum_k \rho_k$. Moreover, the density of a fluid can be influenced by the temperature T (e.g., density decreases when temperature increases) and by the pressure p (density increases when pressure increases due to compressibility). In a formal manner, the density is to be regarded as a dependent thermodynamic variable for which a constitutive relationship, also called *equation of state* (EOS), $\rho = \rho(\rho_k, T, p)$ holds.

Among the state variables, density merits special attention as its spatial and temporal variations are fundamental to the class of *density-driven flow problems*. Mathematically, this is expressed by the presence of ρ in the gravity (buoyancy) term in the momentum balance equation for a fluid. In systems with variable density many different, yet physically correct, flow patterns may occur. The corresponding mathematical models have interesting non-unique solutions, and issues of physical stability, oscillations and chaos arise.

In numerous natural and engineered systems, density-dependent flow processes play an important role. Besides various applications in the dynamics of pure viscous fluids, atmospheric flows, oceanography, limnology, energy technology and astrophysics, we find such phenomena in many areas of subsurface hydrol-

ogy, geophysics, reservoir mechanics, underground nuclear engineering and material science, where there is a presence of a permeable solid (usually assumed to be deformable), which is the *porous medium*. Typical applications include concentrated brine transport of pollutants or radionuclides released from a repository in a rock salt formation, saltwater intrusion in exploited coastal aquifers, infiltration of leachates from landfills and industrial waste disposals, design of geothermal energy extraction systems, large-scale convection in deep geothermal areas, convection in snow layers, permafrost or magma chambers, diagenetic processes in sedimentary basins, drying process technologies, and many others.

Density-dependent flow processes in porous media have received the attention of many researchers during the last 30 years, although, the pioneering work in this field is even older. Horton and Rogers[114], and independently Lapwood[136] first addressed the porous-medium analog of the Rayleigh-Bénard convection with regard to thermal instability in a saturated porous layer of infinite horizontal extent. Wooding[241] extended these studies, and Schneider[197] and Elder[58] performed laboratory experiments with Hele-Shaw cells. De Josselin de Jong[120] developed the vortex theory for density-driven flows in saturated porous media. While the first numerical computations of two-dimensional convection processes in porous media were given by Wooding[241] using an iterative relaxation method, Elder[58,59] was the first to fully compute the multicellular thermal convection currents in two-dimensional porous layers for both steady-state and transient situations using a finite-difference method. Since then, the number of papers on the subject of variable-density flow processes in porous media has been growing at an ever increasing rate.

Excellent reviews of prior work have been presented by Combarnous and Borries[31], Cheng[29], Bejan[18], Gebhart *et al.*[78], Tien and Vafai[220], Nield and Bejan[157] and Holzbecher[107]. Most of the earlier (pre-1960) investigations were motivated by an interest in geophysical and geothermal phenomena. As subsequent studies covered an increasing range of subjects, the importance of numerical analysis soon became obvious with the application of the various numerical techniques (finite differences, Galerkin technique, spectral method, boundary element method, multigrid technique, finite elements, finite volumes, e.g.[104,212,36,103,192]). Among the vast work we want to highlight the following basic studies: The stability of two-dimensional convection rolls in a porous medium heated from below was studied by Straus[212], who showed that at a given Rayleigh number less than 380, there is only a limited band of wave numbers in form of a balloon-shaped closed curve for which convective rolls are stable. Oscillatory convective currents in two dimensions were first reported by Combarnous and Le Fur[32], Horne and O'Sullivan[112,113] and simulated by Horne and Caltagirone[111] and Schubert and Straus[200] in a square cavity. Oscillatory convections in three-dimensional porous boxes were studied by Horne[110], Schubert and Straus[199], Straus and Schubert[213,214] and Caltagirone *et al.*[25]. The variation of the critical Rayleigh number (characterizing the onset of convection) and corresponding preferred cellular modes were analyzed by Beck[16] for an enclosed three-dimensional porous medium. Numerical computations of cellular convection at high Rayleigh numbers were performed by Aidun[3], Aidun and Steen[4], Kimura *et al.*[123,130], Caltagirone *et al.*[24] and Caltagirone and Farbie[23]. Effects of anisotropy and heterogeneity were studied by Kvern-

vold and Tyvand[132], McKibbin and O'Sullivan[145,146], McKibbin and Tyvand[147,148,149] and others. Stabilizing effects caused by hydrodynamic dispersion were modeled by Kvernvold and Tyvand[133] and Georgiadis and Catton[80]. Non-Darcian flow effects were considered by Katto and Masuoka[122], Walker and Homsy[234], Prasad and Kladias[180] and Kolditz[125]. Thermohaline (double-diffusive) convection processes in porous media were studied, among others, by Nield[153], Griffiths[87], Rubin[188], Rubin and Roth[189,190], Trevisan and Bejan[221], Murray and Chen[151], Tyvand[224], Green[85], Taunton *et al*.[215], Goyeau *et al*.[82], Oldenburg and Pruess[162], Diersch and Kolditz[49].

In hydrogeologic systems saltwater intrusion and upconing processes are a subject of specific concern. In many situations fluid-density effects are important in the vertical and horizontal displacement of saline water. Usually, the heavier saltwater underlies the lighter freshwater in a natural system and the resulting density stratification stabilizes the flow system. While the density of 'average' surface seawater ranges between 1022 and 1028 kg/m^3, brine densities exceeding 1300 kg/m^3 can occur in deep formations. The existence of high salt concentrations can give rise to large concentration gradients in the form of a narrow freshwater-saltwater transition zone. Here, the underlain salinity acts as the restoring force, while hydrodynamic dispersion and convection lead to a mixing and vertical displacement of the brine. Classically, the sharp saltwater-freshwater interface assumption is made to enable rather simple analytical and numerical solutions. This concept was used independently by Badon-Ghyben[8] and Herzberg[102] to derive a formula, today well-known as the Ghyben-Herzberg relationship, which relates the elevation of the groundwater table to the elevation of the saltwater-freshwater interface assuming a hydrostatic equilibrium. The sharp interface approach (saltwater and freshwater as two immiscible fluids) was subsequently applied and improved in numerous works, for a review see, e.g., Reilly and Goodman[185], Bear[13], and Cheng and Quazar[28]. However, if an assessment of the salt concentration in both local and regional flow systems is desired, the more rigorous miscible-fluid approach is required. The first attempts to model the density-dependent miscible saltwater-freshwater systems applied to coastal problems were made by Henry[99] and Pinder and Cooper[179]. Due to its practical importance, the numerical modeling of saltwater intrusion and upconing processes has received increased attention in the water resources literature over the last 20 years, resulting in better ways to model the advective and dispersive mechanisms with fluid density and viscosity effects. Saltwater intrusion processes were analyzed among others by Segol at al.[203], Segol and Pinder[202], Huyakorn and Taylor[116], Huyakorn *et al*.[117], Volker and Rushton[230], Frind[71], Voss[231,232], Voss and Souza[233], Putti and Paniconi[182], Diersch[41], Galeati *et al*.[76], Gambolati *et al*.[75], Kolditz *et al*.[126], Bués and Oltean[22]. Upconing below pumping wells was studied numerically by Diersch *et al*.[53], Diersch and Nillert[51], Reilly and Goodman[186] and Holzbecher[106]. Waste disposal in deep salt formations required modeling of density-dependent flow processes in the vicinity of salt domes. Studies by Herbert *et al*.[101], Oldenburg and Pruess[161], Oldenburg *et al*.[163], Johns and Rivera[119], Kolditz *et al*.[126], Konikow *et al*.[129], Holzbecher[108] and Younes *et al*.[246] contributed to a better informed discussion of this subject.

More recently, a three-dimensional saltwater upconing process in a box including the influence of salinity

on density and viscosity as well as effects of hydrodynamic dispersion was studied in the laboratory by Oswald[167]. Today, this saltpool problem is well known and has been modeled by various authors[2,118,168] with varying success. The best agreement with the measurements has been recently achieved by Johannsen *et al*.[118] who used very fine meshes (up to about 17 million nodal points). For high-concentration brine transport Hassanizadeh and Leijnse[98] and Hassanizadeh[92] have proposed extensions of the dispersion theory in form of a non-Fickian law. In high-concentration-gradient experiments Schotting *et al*.[198] have shown that the nonlinear dispersion law can achieve a better agreement with the measurements than the linear Fickian dispersion model. Boundary conditions for brine transport differ from usual formulations as shown by Hassanizadeh and Leijnse[97] for a solid rock salt interface. Instead of using a no-flow condition, the boundary fluid flux must be proportional to the density gradient at the boundary. Duijn and Schotting[56] showed that this boundary condition is compatible with the non-Boussinesq (full) brine equations and represents a natural choice.

Density-dependent flow processes in porous media are crucial in a wide spectrum of thermal and saline transport problems in many research disciplines and different fields of application. Many problems have received repeated attention, yet surprises continue to appear. For instance, new results of the Elder problem have been presented by Frolkovic and De Schepper[74] and recently by Oltean and Bués[164]. Oltean and Bués use advanced mixed hybrid and discontinuous finite element methods and confirm previous findings[1,126,161]. In contrast, Frolkovic and De Schepper found different results for the cellular convection patterns by a systematical refinement of the mesh.

Where simulation of large-scale (regional) density-dependent flow is desired, various numerical compromises are practised. In order to reduce the computational costs, coarse meshes are used, for which large dispersivities are required to achieve numerically stable solutions. The question remains, to what degree may we rely on those numerical results? How reliable are numerical models for variable-density situations and how applicable are physical benchmark tests at the scale of real-world problems?

The purpose of this paper is to describe the major lines of thought, theoretical concepts, numerical approaches, important mathematical aspects and simulations that characterize the 'state-of-the-art' of density-dependent flow modeling in porous media. Our emphasis is on a complete mathematical description, where thermal and solute density effects, double-diffusive (thermohaline) convections (DDC), fluid viscosity and compressibility effects, saturated and unsaturated porous media, non-Darcian and non-Fickian effects, influences of hydrodynamic dispersion, reactive multicomponental systems, and heterogeneous and time-dependent conditions are incorporated. We will discuss major approaches in the numerical solution of the basic balance equations with their different phenomenological laws and constitutive relationships. Numerical studies are reviewed emphasizing the importance of the Oberbeck-Boussinesq approximation and its (non-Boussinesq) extension, the physical stability and the oscillatory behavior at high Rayleigh numbers. Advanced numerical strategies for solving the coupled spatio-temporal convection processes for two- and three-dimensional problems are considered, where the

consistency problem for the velocity approximation at high density, fully adaptive techniques as well as numerical errors and stability aspects are of specific interest. Standard and newer benchmark tests for density-dependent flow are revisited and critically discussed. We conclude with impacts on real-site large-scale applications. Noting that several challenging issues are still left to be resolved, existing weaknesses in the both theoretical and experimental issues are addressed and subjects of future research will be pointed out. Clearly, the paper does not aim to be a complete review, as the vast field of density-dependent flow in porous media with its adjacent disciplines would easily fill more than a book. Our choice of subjects is mainly determined by the perspective of 'real-world' numerical modelers, and in this sense, it must to some extent remain an individual point of view.

1.2 Fundamentals

1.2.1 Continuum approach

The continuum approach is the standard and as yet most successful way to describe the fundamental processes of flow and transport in porous media. The assumption of a continuum implies that physical properties (such as velocity, pressure, concentration, temperature etc.) are continuously distributed in space and thus exist for any infinitely small *material point*. In the most practical porous-media problems, of course, mass, motion and energy-related quantities can neither be measured nor solved at a *microscopic* level due to the geometric complexity of real geologic media. These difficulties are resolved by a transformation to the *macroscopic* level by averaging over volumes, leading to measurable and solvable quantities for which the continuum assumption is then invoked. The standard approach for deriving macroscopic quantities is the spatial averaging method which has been developed over the last 25 years, with major contributions from Bear and Bachmat[14], Hassanizadeh and Gray[93,94,95,96], Hassanizadeh[90,91], Gray *et al.*[84], Gray[83], Cushman[34] and Whitaker[240]. In the spatial averaging process a macroscopic variable is referred to a *representative elementary volume* (REV), which is composed of M phases. The REV has to be sufficiently large for fluctuations of spatially averaged properties to be negligible. Phases $\alpha = 1, \ldots, M$ are regarded as material domains separated by phase interfaces (e.g., solid-solid, fluid-solid, fluid-fluid) where the system properties undergo an abrupt change (discontinuity). Each phase α is composed of N^α miscible chemical species. It represents a molecular mixture of several identifiable chemical components k. By definition a chemical species k exists in only one phase α. Species that pass through different phases are regarded as separate, phase-pertinent constituents, accordingly the relationship $N = \sum_\alpha N^\alpha$ holds.

The basis of density-dependent flow and transport models is stated by the fundamental physical principles of conservation of mass, momentum and energy. Additionally, closure of the resulting system of balance laws requires a sufficient number of equations, so that all unknowns can be determined.

1.2.2 Balance laws

The macroscopic mass conservation for a multiphase, multispecies system is

$$\frac{\partial}{\partial t}(\varepsilon^{\alpha}\rho^{\alpha}\omega_k^{\alpha}) + \nabla\cdot(\varepsilon^{\alpha}\rho^{\alpha}\boldsymbol{v}^{\alpha}\omega_k^{\alpha}) + \nabla\cdot\boldsymbol{j}_k^{\alpha} = R_k^{\alpha} + Q_k^{\alpha} \quad (1\text{-}1)$$

where ε is a volume fraction, ρ is a density, $\omega_k = \rho_k/\rho$ is a mass fraction, $\boldsymbol{j}_k$ is a nonadvective species flux vector accounting for dispersive and diffusive transport, $\boldsymbol{v}$ is a macroscopic phase velocity vector, R_k is a general reaction term, Q_k is a bulk solute mass source term incorporating both internal and external transfer, $\alpha = l, g, s$ is a phase indicator (l indicates liquid, g indicates gas, s indicates solid), and k is a species indicator.

The mass balance for each phase α is obtained by summing (1-1) over all species k, *viz.*,

$$\frac{\partial}{\partial t}(\varepsilon^{\alpha}\rho^{\alpha}) + \nabla\cdot(\varepsilon^{\alpha}\rho^{\alpha}\boldsymbol{v}^{\alpha}) = Q^{\alpha} \quad (1\text{-}2)$$

with the identities

$$\sum_{\alpha}\varepsilon^{\alpha} = 1 \qquad \sum_{k}\omega_k^{\alpha} = 1$$
$$\sum_{k}\boldsymbol{j}_k^{\alpha} = 0 \qquad \sum_{k}R_k^{\alpha} = 0 \quad (1\text{-}3)$$

and the definition

$$\sum_{k}Q_k^{\alpha} = Q^{\alpha} \quad (1\text{-}4)$$

The macroscopic momentum conservation for each phase α is

$$\frac{\partial}{\partial t}(\varepsilon^{\alpha}\rho^{\alpha}\boldsymbol{v}^{\alpha}) + \nabla\cdot(\varepsilon^{\alpha}\rho^{\alpha}\boldsymbol{v}^{\alpha}\boldsymbol{v}^{\alpha}) - \nabla\cdot\sigma^{\alpha} = \varepsilon^{\alpha}(\rho^{\alpha}\boldsymbol{g} + \boldsymbol{F}^{\alpha}) \quad (1\text{-}5)$$

where σ is a viscous stress tensor, $\boldsymbol{g}$ is an external body force (e.g., due to gravity or ionic attractions), and $\boldsymbol{F}$ is an interfacial drag term of momentum exchange.

The phase-related energy balance can be written in the general form

$$\frac{\partial}{\partial t}\left[\varepsilon^{\alpha}\rho^{\alpha}\left(E^{\alpha} + \frac{(v^{\alpha})^2}{2}\right)\right] + \nabla\cdot\left[\varepsilon^{\alpha}\rho^{\alpha}\boldsymbol{v}^{\alpha}\left(E^{\alpha} + \frac{(v^{\alpha})^2}{2}\right)\right] + \nabla\cdot(\boldsymbol{j}_e^{\alpha} - \sigma^{\alpha}\cdot\boldsymbol{v}^{\alpha}) = \varepsilon^{\alpha}(\rho^{\alpha}\boldsymbol{g} + \boldsymbol{F}^{\alpha})\cdot\boldsymbol{v}^{\alpha} + H_e^{\alpha} \quad (1\text{-}6)$$

where E is the internal (thermal) energy, $v = \|\boldsymbol{v}\|$ is the magnitude of $\boldsymbol{v}$, $\boldsymbol{j}_e$ is a nonadvective energy flux comprising dispersive and conductive components, and H_e represents the energy source term comprising internal and external energy supply.

We have the following set of balance equations: (i) For each species k there is one mass balance equation (1-1). (ii) For each phase α there are D momentum equations, one mass conservation equation (1-2) and one energy equation, where $D = 1, 2, 3$ is the dimension of the problem. Accordingly, $N + (2 + D)M$ balance equations are available for which suitable primary physical independent variables have to be designated, such as $\omega_k^{\alpha}, \boldsymbol{v}^{\alpha}, E^{\alpha}$. Additionally, there are quantities appearing in the equations, e.g., $\boldsymbol{j}_k^{\alpha}, \sigma^{\alpha}, \boldsymbol{F}^{\alpha}, \boldsymbol{j}_e^{\alpha}, \rho^{\alpha}$, that must be expressed by phenomenological laws, equa-

tions of state and constitutive functions. We note that a complete constitutive theory requires a rigorous thermodynamic approach[83,90,91]. The entropy inequality can be applied to restrict constitutive equations via the Coleman and Noll method[91,95].

1.2.3 Phenomenological laws

For the nonadvective (dispersive) fluxes of mass $\boldsymbol{j}_k^\alpha$, momentum σ^α and energy $\boldsymbol{j}_e^\alpha$ phenomenological laws are available.

The species mass flux $\boldsymbol{j}_k^\alpha$ is commonly expressed by the linear *Fickian* type equation

$$\boldsymbol{j}_k^\alpha = -\rho^\alpha \boldsymbol{D}^\alpha \cdot \nabla \omega_k^\alpha \tag{1-7}$$

where $\boldsymbol{D}$ is the hydrodynamic dispersion tensor, which is assumed to be independent of the concentration and its gradient. It is, however, considered to be a function of the velocity $\boldsymbol{v}^\alpha$ and is commonly described by the *Bear-Scheidegger* dispersion relationship[12] for a porous medium according to

$$\left.\begin{aligned} \boldsymbol{D}^\alpha &= \varepsilon^\alpha (\boldsymbol{D}_d^\alpha + \boldsymbol{D}_m^\alpha) \\ \boldsymbol{D}_d^\alpha &= D_d^\alpha \boldsymbol{T} \\ \boldsymbol{D}_m^\alpha &= \beta_T \|\boldsymbol{v}\|^\alpha \boldsymbol{I} + (\beta_L - \beta_T) \frac{\boldsymbol{v}^\alpha \otimes \boldsymbol{v}^\alpha}{\|\boldsymbol{v}\|^\alpha} \end{aligned}\right\} \tag{1-8}$$

where $\boldsymbol{D}$ is the tensor of hydrodynamic dispersion, $\boldsymbol{D}_m$ is the tensor of mechanical dispersion, D_d is a coefficient of molecular diffusion, $\boldsymbol{T}$ is the tortuosity tensor, $\boldsymbol{I}$ is the unit vector, and β_L and β_T are the longitudinal and transverse dispersivities, respectively.

For Fick's law (1-7) the dispersive mass flux of a species is proportional to the concentration gradient. However, it has been shown[98,198] that if large concentration gradients exist, nonlinear effects become important and $\boldsymbol{j}_k^\alpha$ should be replaced by an extended nonlinear (*non-Fickian*) dispersion law,

$$\boldsymbol{j}_k^\alpha (\Im_H \|\boldsymbol{j}_k^\alpha\| + 1) = -\rho^\alpha \boldsymbol{D}^\alpha \cdot \nabla \omega_k^\alpha \tag{1-9}$$

where $\Im_H$ represents an additional high-concentration (HC) dispersion coefficient and $\boldsymbol{D}$ is the Bear-Scheidegger dispersion tensor (1-8), with longitudinal and transverse dispersivities considered to be properties of the porous medium and independent of the fluid properties and transport quantities. By using the nonlinear dispersion law (1-9), laboratory experiments for high-concentrated brines could be explained and reproduced reasonably well[198].

The stress tensor σ^α applied to fluid phases is commonly split into the equilibrium (pressure) and the non-equilibrium (deviatoric) parts as

$$\sigma^\alpha = -\varepsilon^\alpha p^\alpha \boldsymbol{I} + \sigma'^\alpha \tag{1-10}$$

where p is the pressure. Assuming *Newton's viscosity law* (including the Stokes assumption) the deviatoric stress tensor can be written in the following form

$$\sigma'^\alpha = 2\varepsilon^\alpha \mu^\alpha \left[\boldsymbol{d}^\alpha - \frac{1}{3}(\nabla \cdot \boldsymbol{v}^\alpha)\boldsymbol{I}\right] \tag{1-11}$$

with the strain-rate tensor

$$\boldsymbol{d}^{\alpha} = \frac{1}{2}[\nabla \boldsymbol{v}^{\alpha} + (\nabla \boldsymbol{v}^{\alpha})^{T}] \tag{1-12}$$

where μ is the dynamic fluid viscosity.

The energy flux vector $\boldsymbol{j}_e^{\alpha}$ is usually expressed by a linear *Fourier* heat flux, given in a generalized form by

$$\boldsymbol{j}_e^{\alpha} = -\Lambda^{\alpha} \cdot \nabla T^{\alpha} \tag{1-13}$$

with the tensor of hydrodynamic thermodispersion Λ defined by

$$\left.\begin{aligned} \Lambda^{\alpha} &= \varepsilon^{\alpha}(\Lambda_c^{\alpha} + \Lambda_m^{\alpha}) \\ \Lambda_c^{\alpha} &= \lambda^{\alpha} \boldsymbol{I} \\ \Lambda_m^{\alpha} &= c^{\alpha} \rho^{\alpha} \boldsymbol{D}_m^{\alpha} \end{aligned}\right\} \tag{1-14}$$

where T is the temperature, Λ_c is the conductive part of the thermodispersion tensor, λ is the heat conductivity, Λ_m is the mechanical part of the thermodispersion tensor, and c is a heat capacity. Note that the mechanical thermodispersion Λ_m is described by the Scheidegger-Bear relationship (1-8).

In the phenomenological laws stated above, the fluxes are driven by their corresponding extensive quantities (mass, momentum, heat gradients). However, *cross-effects* sometimes occur in which other extensive quantities may also contribute to the fluxes[14]. It is exemplified by the *Soret (thermodiffusion) effect*, in which the mass flux $\boldsymbol{j}_k^{\alpha}$ is additionally influenced by a temperature gradient ∇T^{α},

$$\boldsymbol{j}_k^{\alpha} = -\rho^{\alpha} \boldsymbol{D}^{\alpha} \cdot \nabla \omega_k^{\alpha} - \boldsymbol{D}_{\lambda}^{\alpha} \cdot \nabla T^{\alpha} \tag{1-15}$$

and the *Dufour effect*, in which the energy (heat) flux $\boldsymbol{j}_e^{\alpha}$ is additionally caused by a concentration gradient $\nabla \omega_k^{\alpha}$

$$\boldsymbol{j}_e^{\alpha} = -\Lambda^{\alpha} \cdot \nabla T^{\alpha} - \rho^{\alpha} \Lambda_d^{\alpha} \cdot \nabla \omega_k^{\alpha} \tag{1-16}$$

The Soret coupling $\boldsymbol{D}_{\lambda}$ between temperature and concentration can be positive or negative. Bifurcation behavior appears for a negative Soret coupling as found by Barten *et al.*[11] analyzing pure fluid mixtures. While Dufour cross-coupling effects are often negligible for liquids, this is not necessarily the case for gas flows.

Another example for cross-coupling effects is the modeling of *chemico-osmosis phenomena*, in which pressure and external body forces (gravity or electromagnetic fields) can affect the mass flux $\boldsymbol{j}_k^{\alpha}$ as thoroughly discussed in[97].

1.2.4 Equations of state

Equations of state (EOS) represent fundamental thermodynamic relationships between volume, concentration, and temperature. EOS arise for the internal energy E^{α} and the density ρ^{α}.

The internal energy E^{α} is a state function of entropy S^{α}, specific volume $\upsilon^{\alpha} = 1/\rho^{\alpha}$, and concentration ω^{α}:

$$dE^\alpha = T^\alpha dS^\alpha - p^\alpha d\upsilon^\alpha + \sum_k \mu_k^\alpha d\omega_k^\alpha \tag{1-17}$$

where the following thermodynamic variables appear

$$\left.\begin{aligned} T^\alpha &= \left.\frac{\partial E^\alpha}{\partial S^\alpha}\right|_{\upsilon^\alpha,\,\omega_k^\alpha} && \text{temperature} \\ p^\alpha &= -\left.\frac{\partial E^\alpha}{\partial \upsilon^\alpha}\right|_{S^\alpha,\,\omega_k^\alpha} && \text{pressure} \\ \mu_k^\alpha &= \left.\frac{\partial E^\alpha}{\partial \omega_k^\alpha}\right|_{S^\alpha,\,\upsilon^\alpha} && \text{chemical potential} \end{aligned}\right\} \tag{1-18}$$

It yields (e.g.,[14])

$$dE^\alpha = \left(T^\alpha \left.\frac{\partial p^\alpha}{\partial T^\alpha}\right|_{\upsilon^\alpha,\,\omega_k^\alpha} - p^\alpha\right) d\upsilon^\alpha + c^\alpha dT^\alpha + \sum_k \mu_k^\alpha d\omega_k^\alpha \tag{1-19}$$

with the *heat capacity* defined by

$$c^\alpha = \left.\frac{\partial E^\alpha}{\partial T^\alpha}\right|_{\upsilon^\alpha,\,\omega_k^\alpha} \tag{1-20}$$

The relation (1-19) is used in a general case to express the internal energy E^α in the energy balance statement (1-6). Practically, if both pressure and temperature effects are important it is convenient to introduce the *enthalpy* in form of

$$h_e^\alpha = E^\alpha + p^\alpha \upsilon^\alpha = E^\alpha + \frac{p^\alpha}{\rho^\alpha} \tag{1-21}$$

where h_e^α has to be developed by constitutive relationships. In general, the chemical potential $\mu_k^\alpha = \mu_k^\alpha(p^\alpha, \omega_k^\alpha, T^\alpha)$ is a dependent variable, and further constitutive relations are required. However, in most applications the pressure and chemical effects on the internal energy are negligible, so that E^α becomes only dependent on the temperature T^α

$$dE^\alpha \approx c^\alpha dT^\alpha \tag{1-22a}$$

If the heat capacity c^α is independent of the temperature T^α, the internal energy E^α can be given explicitly

$$E^\alpha = c^\alpha (T^\alpha - T_0^\alpha) \tag{1-22b}$$

Generally, the density ρ^α can be regarded as a function of pressure p^α, concentration ω_k^α and temperature T^α

$$\rho^\alpha = \rho^\alpha(p^\alpha, \omega_k^\alpha, T^\alpha) \tag{1-23}$$

The total differential then yields

$$d\rho^{\alpha} = \left.\frac{\partial \rho^{\alpha}}{\partial p^{\alpha}}\right|_{\omega_k^{\alpha},\, T^{\alpha}} dp^{\alpha} + \left.\frac{\partial \rho^{\alpha}}{\partial \omega_k^{\alpha}}\right|_{p^{\alpha},\, T^{\alpha}} d\omega_k^{\alpha} + \left.\frac{\partial \rho^{\alpha}}{\partial T^{\alpha}}\right|_{p^{\alpha},\, \omega_k^{\alpha}} dT^{\alpha} \qquad (1\text{-}24)$$

$$= \underbrace{\left(\frac{1}{\rho^{\alpha}}\frac{\partial \rho^{\alpha}}{\partial p^{\alpha}}\right)}_{\gamma} \rho^{\alpha} dp^{\alpha} + \underbrace{\left(\frac{1}{\rho^{\alpha}}\frac{\partial \rho^{\alpha}}{\partial \omega_k^{\alpha}}\right)}_{\alpha} \rho^{\alpha} d\omega_k^{\alpha} + \underbrace{\left(\frac{1}{\rho^{\alpha}}\frac{\partial \rho^{\alpha}}{\partial T^{\alpha}}\right)}_{-\beta} \rho^{\alpha} dT^{\alpha}$$

where γ is the phase (fluid) *compressibility*, and α and β are the volumetric solutal and thermal *expansion coefficient*, respectively. If we assume that γ, α and β are constant, the integration of (1-24) immediately leads to the EOS for the density in the common form

$$\rho^{\alpha} = \rho_0^{\alpha} e^{\gamma(p^{\alpha} - p_0^{\alpha}) + \alpha(\omega_k^{\alpha} - \omega_{k0}^{\alpha}) - \beta(T^{\alpha} - T_0^{\alpha})} \qquad (1\text{-}25)$$

where suitable reference values appear for the density $\rho_0^{\alpha} = \rho^{\alpha}_{p_0^{\alpha}, \omega_{k0}^{\alpha}, T_0^{\alpha}}$ at reference pressure p_0^{α}, reference concentration ω_{k0}^{α} and reference temperature T_0^{α}.

The EOS for the fluid density (1-24) is often linearly approximated in the form

$$\rho^{\alpha} = \rho_0^{\alpha}[1 + \gamma(p^{\alpha} - p_0^{\alpha}) + \alpha(\omega_k^{\alpha} - \omega_{k0}^{\alpha}) - \beta(T^{\alpha} - T_0^{\alpha})] \qquad (1\text{-}26)$$

and commonly γ, α and β are considered constant[157]. While for most practical applications this assumption is valid for compressibility γ and solutal expansion α, a constant thermal expansion coefficient β may become inappropriate for geothermal applications where a larger temperature range has to be considered and thermal anomalies in ρ^{α} (such as the $4°C$ anomaly for water) can also play a role (Fig. 1.1).

Significant discrepancies can then arise from the linear approach in both magnitude and slope. For temperatures within the range from 0 to 100 $°C$, the thermal expansion coefficient of freshwater ($\omega_k^l = \omega_{k0}^l = 0$, $p^l = p_0^l$) actually varies from $-0.68 \cdot 10^{-4}$ up to $7.5 \cdot 10^{-4}$ K^{-1}, and is zero at $4°C$ (e.g., Marsily[143]). To improve the relationship (1-26), Perrochet and Tacher[178] introduced a 6th order polynomial $\rho^l = \rho^l(T^l)$ with high accuracy. A Taylor series expansion of the polynomial about its reference values p_0^l, ω_{k0}^l, T_0^l up to the 6th order term can be reformed to an expression according to the state equation (1-26), see[44] for more. In doing so, β takes now the role of a function being dependent on the temperature T^l. It defines a nonlinear *variable thermal expansion* $\beta = \beta(T^l)$, which is applied to the state equation in form of (1-26) and reads as follows (dropping the phase indicator here for sake of simplicity)

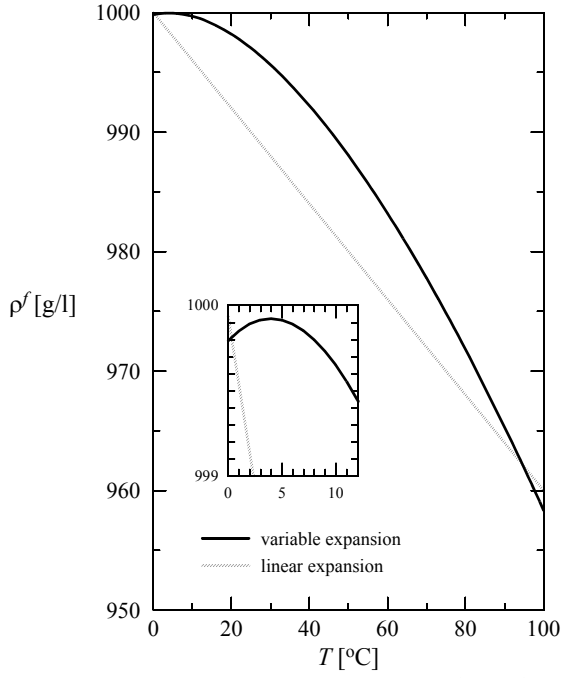

Figure 1.1 Density of freshwater ρ^f (at $\omega_k^f = \omega_{k0}^f$, $p^f = p_0^f$) as a function of temperture T in a range of 0 and 100 $°C$, close-up view indicates density anomaly[44].

$$\begin{aligned}\beta(T) = -\frac{1}{\rho_0}\,[\;&(b + 2cT_0 + 3dT_0^2 + 4eT_0^3 + 5fT_0^4 + 6gT_0^5) + \\ &(c + 3dT_0 + 6eT_0^2 + 10fT_0^3 + 15gT_0^4)(T - T_0) + \\ &(d + 4eT_0 + 10fT_0^2 + 20gT_0^3)(T - T_0)^2 + \\ &(e + 5fT_0 + 15gT_0^2)(T - T_0)^3 + \\ &(f + 6gT_0)(T - T_0)^4 + \\ &g(T - T_0)^5\;]\end{aligned} \tag{1-27}$$

with ρ_0 corresponding to ω_{k0}, p_0 and T_0, where b, c, d, e, f, g are new coefficients listed in[44,178]. As a consequence of the nonlinear (variable) expansion function (1-27) the term $1/\rho^\alpha \partial\rho^\alpha/\partial T^\alpha$ in (1-24) is not longer constant because we find

$$\frac{1}{\rho^\alpha}\frac{\partial\rho^\alpha}{\partial T^\alpha} = -\frac{\beta(T^\alpha) + \dfrac{\partial\beta(T^\alpha)}{\partial T^\alpha}(T^\alpha - T_0^\alpha)}{1 + \gamma(p^\alpha - p_0^\alpha) + \alpha(\omega_k^\alpha - \omega_{k0}^\alpha) - \beta(T^\alpha)(T^\alpha - T_0^\alpha)} \tag{1-28}$$

1.2.5 Constitutive equations

Constitutive relations are required to close the system of equations by expressing unknown quantities in the balance and phenomenological laws in terms of accessible (measurable) parameters. Constitutive relationships, however, are usually of approximate and empirical nature. For density-dependent flow processes they are required for the interfacial drag term $\boldsymbol{F}^\alpha$, dynamic viscosity μ^α, enthalpy h_e^α or heat capacity c^α, thermal conductivity λ^α, volume fraction ε^α and other dependent variables.

The interfacial drag term of momentum exchange $\boldsymbol{F}^\alpha$ in a porous medium appearing in (1-5) can be developed for both linear and quadratic drag of a fluid phase

$$\boldsymbol{F}^\alpha = -\mu^\alpha(\boldsymbol{k}^\alpha)^{-1}\cdot\boldsymbol{q}^\alpha - \mu^\alpha(\boldsymbol{k}^\alpha)^{-1}\Im_F\|\boldsymbol{q}\|^\alpha\cdot\boldsymbol{q}^\alpha \qquad \text{for} \quad \alpha = l, g \tag{1-29}$$

with the volumetric flux density (Darcy or filtration velocity) given by

$$\boldsymbol{q}^{\alpha} = \varepsilon^{\alpha}(\boldsymbol{v}^{\alpha} - \boldsymbol{v}^{s}) \qquad \text{for} \quad \alpha = l, g \tag{1-30}$$

where $\boldsymbol{k}$ is a permeability tensor and $\Im_F$ is a Forchheimer coefficient. In (1-29) the linear part is the *Darcy* term, while the quadratic drag is known as the *Forchheimer* term. Generalizations of the quadratic drag for anisotropic conditions can be found in[210]. For the solid phase, the drag term $\boldsymbol{F}^{s}$ must be equal to the negative of the sum of $\boldsymbol{F}^{\alpha}$'s in (1-29) if neglecting fluid-fluid momentum interactions.

The dynamic viscosity of a fluid phase μ^{α} appearing in (1-11) and (1-29) is typically regarded as a function of concentration ω_k^{α} and temperature, *viz.*,

$$\mu^{\alpha} = \mu^{\alpha}(\omega_k^{\alpha}, T^{\alpha}) \tag{1-31}$$

Combining the high-concentration dependency as given by Lever and Jackson[140] with an empirical temperature dependency over a range of $T^{\alpha} = 0°C$ to $300°C$, the following relationship holds as proposed in[44]

$$\frac{\mu_0^{\alpha}}{\mu^{\alpha}} = \frac{1 + 0.7063\varsigma - 0.04832\varsigma^3}{1 + 1.85\omega_k - 4.1\omega_k^2 + 44.5\omega_k^3} \tag{1-32}$$

$$\varsigma = \frac{T^{\alpha} - 150}{100}\ °C \qquad \omega_k = \omega_k^{\alpha}$$

where μ_0 is a reference viscosity at $\omega_k = 0$, $T = 150°C\ (\varsigma = 0)$. It is easy to relate (1-32) to arbitrary reference values T_0, ω_{k0} by expanding $\frac{\mu^{\alpha}(T_0, \omega_{k0})}{\mu^{\alpha}} = \left(\frac{\mu_0^{\alpha}}{\mu^{\alpha}}\right) \Big/ \left(\frac{\mu_0^{\alpha}}{\mu^{\alpha}(T = T_0, \omega_k = \omega_{k0})}\right)$. Further relationships are given in[107,166].

If the enthalpy h_e^{α} is to be used as the primary variable, appropriate constitutive functions are required. Typically, h_e^{α} is considered a function of pressure $h_e^{\alpha} = h_e^{\alpha}(p^{\alpha})$, while the temperature T^{α} is considered a function of both, enthalpy and pressure: $T^{\alpha} = T^{\alpha}(h_e^{\alpha}, p^{\alpha})$. Such a description can be useful for geothermal steam-water two-phase flow systems where phase transitions occur (e.g., Faust and Mercer[64]), but the enthalpy-pressure formulation is not satisfactory for more complex (e.g., multispecies) transport situations and formulations in pressure, temperature and saturation are today preferred for simulating nonisothermal multiphase systems[100]. Mostly, and particularly in one-phase energy transport the pressure effects are negligible, and the temperature T^{α} can be directly used as the primary variable in the energy balance equation (1-6) with (1-22a). Here the heat capacity c^{α} (1-20) is a parameter which is practically constant in a temperature regime below $100°C$. However, for large temperatures the heat capacity c^{α} becomes temperature-dependent $c^{\alpha} = c^{\alpha}(T^{\alpha})$ [107].

Thermal conductivities λ^{α} appearing in (1-14) can often be considered as constant material parameters. In a high-temperature regime, however, λ^{α} can also become dependent on temperature for fluid phases[107].

The volume fraction ε^{α} appears as a geometry-dependent variable resulting from the volume averaging process over a REV. It is convenient to express ε^{α} for fluid phases $\alpha = l, g$ and one solid phase $\alpha = s$ in

a porous medium as

$$\varepsilon^l = \varepsilon s^l \qquad \varepsilon^g = \varepsilon s^g \qquad \varepsilon^s = 1 - \varepsilon \tag{1-33}$$

with

$$s^l + s^g = 1 \qquad 0 \le s^l \le 1 \qquad 0 \le s^g \le 1 \tag{1-34}$$

where ε is the porosity, s is a saturation referring to liquid (l) and gas (g) phases. Assuming that the liquid phase is the wetting phase, the relationship between the quantity of a wetting liquid (l) and a nonwetting gas (g) in the void space ε is recorded by the macroscopic *capillary pressure* p_c, defined as

$$p_c = p^g - p^l \tag{1-35}$$

for which constitutive relationships are required, e.g.,

$$p_c = p_c(s^l, T^l, T^g, \omega_k^l, \omega_k^g) \tag{1-36}$$

Commonly, the capillary pressure p_c is considered to be dependent on the wetted liquid phase (l) only, *viz*.,

$$p_c = p^g - p^l = p_c(s^l) \tag{1-37}$$

where numerous empirical relationships exist to express $p_c(s^l)$ for two- and three-fluid-phase systems. Well known are the Brooks-Corey and the van Genuchten relationships, applied to two immiscible fluid phases, see e.g.[12,14]. More complex parametric models for three-fluid-phase systems have been developed by different authors, see[150] for a review.

The presence of more than one fluid phase in a porous medium has consequences on other variables too. Particularly, the interfacial momentum exchange terms in (1-29) depend on the fluid saturations s^l, s^g. This is expressed by postulating a saturation-dependency in the intrinsic permeability $\boldsymbol{k}^\alpha$ in the following form:

$$\boldsymbol{k}^\alpha = \boldsymbol{k}^\alpha(s^\alpha) = k_r^\alpha(s^\alpha)\boldsymbol{k} \qquad 0 < k_r^\alpha \le 1 \qquad \alpha = l, g \tag{1-38}$$

where k_r is a relative permeability and $\boldsymbol{k}$ is the fluid-independent permeability tensor of the porous medium, which is anisotropic in general. Various empirical relationships for $k_r^\alpha = k_r^\alpha(s^\alpha)$ exist for two- and three-fluid-phase systems, the Brooks-Corey and van Genuchten relations being the most common[12,14,150].

In changing the porosity ε (1-33) of a porous medium, the compression work of the solid skeleton (deformation) is to be taken into account, while concentration and temperature effects are considered negligible. Thus,

$$\varepsilon = \varepsilon(p^\alpha)$$
$$d\varepsilon = \frac{\partial \varepsilon}{\partial p^\alpha} dp^\alpha = \left(\frac{1}{\varepsilon^s}\frac{\partial \varepsilon}{\partial p^\alpha}\right)\varepsilon^s dp^\alpha = \Upsilon(1-\varepsilon)dp^\alpha \tag{1-39}$$

where Υ denotes the coefficient of skeleton compressibility.

1.2.6 Complete equations

In the practical modeling of density-dependent flow

processes in porous media the above balance laws with their phenomenological and constitutive relations are further simplified. Most important are restrictions in the number of phases α and related simplifications. The major assumptions are listed as follows:

Phase assumptions: The solid phase s is assumed deformable, but solid grains are incompressible. Inserting (1-30) into (1-2) and using the definition (1-33) the mass conservation equation for the liquid phase l reads

$$\varepsilon s^l \frac{\partial \rho^l}{\partial t} + \rho^l s^l \frac{\partial \varepsilon}{\partial t} + \rho^l \varepsilon \frac{\partial s^l}{\partial t} + \nabla \cdot (\rho^l \boldsymbol{q}^l) + \nabla \cdot (\varepsilon s^l \rho^l \boldsymbol{v}^s) = Q^l \quad (1\text{-}40)$$

Assuming very slowly deformable media and slightly compressible fluids the approximation holds[14]

$$\nabla \cdot (\varepsilon s^l \rho^l \boldsymbol{v}^s) \approx \varepsilon s^l \rho^l (\nabla \cdot \boldsymbol{v}^s) \quad (1\text{-}41)$$

The expression $\nabla \cdot \boldsymbol{v}^s$ is obtained from the solid mass balance (1-2) for $(\alpha = s)$:

$$\frac{\partial [(1-\varepsilon)\rho^s]}{\partial t} + \nabla \cdot [(1-\varepsilon)\rho^s \boldsymbol{v}^s] = 0 \quad (1\text{-}42)$$

where $Q^s \equiv 0$ is assumed. For incompressible solid grains, equation (1-42) becomes[14]

$$\nabla \cdot \boldsymbol{v}^s \approx \left(\frac{1}{1-\varepsilon}\right) \frac{\partial \varepsilon}{\partial t} \quad (1\text{-}43)$$

With (1-43) and (1-41) the mass conservation of the liquid phase (1-40) results in the following form

$$\varepsilon s^l \frac{\partial \rho^l}{\partial t} + \rho^l s^l \left(\frac{1}{1-\varepsilon}\right) \frac{\partial \varepsilon}{\partial t} + \rho^l \varepsilon \frac{\partial s^l}{\partial t} + \nabla \cdot (\rho^l \boldsymbol{q}^l) = Q^l \quad (1\text{-}44)$$

A liquid phase l (e.g., water) and a gas phase g (e.g., air) coexist in the void space, where the gas phase is considered stagnant. This is the basis of unsaturated-saturated density-dependent flow and transport processes. For the sake of simplicity we can drop all phase superscripts because the only dynamic phase is the liquid phase. Note that geothermal flows can represent true multiphase systems (e.g., steam-water two-phase flow), for which the assumption of a stagnant gas phase is not appropriate.

Momentum assumptions: The inertial terms in the momentum balance are neglected by assuming slow movements in the porous medium. Compression and deformation work may be excluded in the momentum balance.

Energy assumptions: Kinetic energy effects in the energy balance are negligible. Furthermore, local thermal equilibrium is assumed between all phases, *viz*.,

$$(T^\alpha - T) = 0 \qquad \text{for} \quad \alpha = s, l, g \quad (1\text{-}45)$$

which enables the introduction of the system temperature T. Additionally, for the gas phase g the thermal capacity and conductivity can be neglected with respect to the solid and liquid phases.

In using these major assumptions the following balance equations result for the liquid phase (phase indicators will be omitted in the following to keep the notation simple):

mass conservation

$$\varepsilon s\frac{\partial \rho}{\partial t}+\rho\left(s\Upsilon\frac{\partial p}{\partial t}+\varepsilon\frac{\partial s}{\partial t}\right)+\nabla\cdot(\rho\boldsymbol{q})\;=\;Q \tag{1-46}$$

$$\frac{\partial}{\partial t}(\varepsilon s\rho\omega_k)+\nabla\cdot(\rho\boldsymbol{q}\omega_k)+\nabla\cdot\boldsymbol{j}_k\;=\;R_k+Q_k \tag{1-47a}$$

$$\varepsilon s\rho\frac{\partial \omega_k}{\partial t}+\rho\boldsymbol{q}\cdot\nabla\omega_k+\nabla\cdot\boldsymbol{j}_k\;=\;R_k+Q_k-Q\omega_k \tag{1-47b}$$

momentum conservation

$$0\;=\;-\nabla p+\rho\boldsymbol{g}+\underbrace{\mu\nabla^2\boldsymbol{q}}_{\text{Brinkmann}}\;\underbrace{-\mu(k_r\boldsymbol{k})^{-1}\cdot\boldsymbol{q}}_{\text{Darcy}}\;\underbrace{-\mu(k_r\boldsymbol{k})^{-1}\Im_F\|\boldsymbol{q}\|\cdot\boldsymbol{q}}_{\text{Forchheimer}} \tag{1-48}$$

or

$$\boldsymbol{q}(\Im_F\|\boldsymbol{q}\|+1)\;=\;-\frac{k_r\boldsymbol{k}}{\mu}\cdot(\nabla p-\rho\boldsymbol{g})+k_r\boldsymbol{k}\cdot\nabla^2\boldsymbol{q} \tag{1-49}$$

energy conservation

$$\frac{\partial}{\partial t}[(\varepsilon s\rho c^l+(1-\varepsilon)\rho^s c^s)T]+\nabla\cdot(\rho c^l\boldsymbol{q}T)+\nabla\cdot\boldsymbol{j}_e\;=\;H_e \tag{1-50a}$$

$$[\varepsilon s\rho c^l+(1-\varepsilon)\rho^s c^s]\frac{\partial T}{\partial t}+\rho c^l\boldsymbol{q}\cdot\nabla T+\nabla\cdot\boldsymbol{j}_e\;=\;H_e-Qc^l(T-T_0) \tag{1-50b}$$

which are solved for p, ω_k, $\boldsymbol{q}$ and T with the following constitutive and phenomenological relations

$$\left.\begin{aligned}
\rho\;&=\;\rho_0[1+\gamma(p-p_0)+\alpha(\omega_k-\omega_{k0})-\beta(T-T_0)]\quad\text{with}\quad\beta\;=\;\begin{cases}\text{const}\\ \beta(T)\end{cases}\\
p_c\;&=\;-p\;=\;p(s)\qquad\text{and}\qquad s\;=\;s(p)\\
k_r\;&=\;k_r(s)\\
\boldsymbol{j}_k(\Im_H\|\boldsymbol{j}_k\|+1)\;&=\;-\rho\boldsymbol{D}\cdot\nabla\omega_k-\boldsymbol{D}_\lambda^*\cdot\nabla T\\
\boldsymbol{j}_e\;&=\;-\Lambda\cdot\nabla T-\rho\Lambda_d\cdot\nabla\omega_k\\
\boldsymbol{D}\;&=\;\varepsilon sD_d\boldsymbol{T}+\boldsymbol{D}_m^*\\
\Lambda\;&=\;[\varepsilon s\lambda^l+(1-\varepsilon)\lambda^s]\boldsymbol{I}+\rho c^l\boldsymbol{D}_m^*\\
\boldsymbol{D}_m^*\;&=\;\beta_T\|\boldsymbol{q}\|\boldsymbol{I}+(\beta_L-\beta_T)\frac{\boldsymbol{q}\otimes\boldsymbol{q}}{\|\boldsymbol{q}\|}
\end{aligned}\right\} \tag{1-51}$$

The balance statements (1-47a) and (1-50a) are the basic *divergent forms* of the transport equations which

are transformed into the *convective* (or *advective*) *forms* (1-47b) and (1-50b) by inserting (1-46). Due to the relation (1-22a) the temperature T appears as the explicit variable for the convective form of the energy equation (1-50b). The divergent form (1-50a) can only be derived explicitly for T as the primary variable if we assume temperature-independent heat capacities c^{α} according to (1-22b). The momentum balance in form of (1-49) is a general non-Darcy law involving nonlinear Forchheimer and linear viscous Brinkman effects, termed as *Darcy-Brinkman-Forchheimer* (DBF) flow model. There are situations where Forchheimer and Brinkman effects can be important[125,157,180]. Traditionally, however, they are neglected, which leads to the well-known Darcy equation in the form

$$\boldsymbol{q} = -\frac{k_r \boldsymbol{k}}{\mu} \cdot (\nabla p - \rho \boldsymbol{g}) \tag{1-52}$$

The assumption that the linear Darcy law (1-52) holds in case of high-concentration brine transport, while the nonlinear (non-Fickian) dispersion law (1-9) is required, is shown in Watson *et al*.[235,236].

REMARK 1: There is an analogy in the resulting momentum equations (1-48) derived for flows in fractures, and in fissured materials, e.g.[15,45,124]. Neglecting inertial terms and averaging the momentum law over the fracture, where an external momentum exchange at the external (top and bottom) surfaces appears, it is

$$0 = -\nabla p + \rho \boldsymbol{g} + \boldsymbol{F}_f \tag{1-53}$$

where $\boldsymbol{F}_f$ is a surface friction (viscous shear) term. A linear expression can be derived for a laminar *Hagen-Poiseuille* flow of linear nature as

$$\boldsymbol{F}_f = -a\mu r^{-2}\boldsymbol{v} \quad \text{with} \quad \begin{cases} r = b/2, a = 3 & \text{plane} \\ r = R/2, a = 2 & \text{axisymmetry} \end{cases} \tag{1-54}$$

where r is the hydraulic radius, b is an aperture, and R is a radius of a tube. Channel flow can be modeled by a quadratic friction approach according to

$$\boldsymbol{F}_f = -\frac{\rho g}{\tau^2 r^{\vartheta}} \|\boldsymbol{v}\| \boldsymbol{v} \quad \text{with} \quad \begin{cases} \tau = C, \vartheta = 1 & \text{Chezy} \\ \tau = M, \vartheta = 4/3 & \text{Manning-Strickler} \end{cases} \tag{1-55}$$

where different friction laws can be useful, e.g., the Chezy or the Manning-Strickler approaches (C is the Chezy, and M the Manning friction coefficient). Using (1-54) and (1-55) Darcy-type and Forchheimer-type equations similar to (1-52) and (1-49), respectively, can be found resulting in a mathematically unified handling of both porous and fracture flow conditions.

REMARK 2: The viscosity μ related to the Brinkman term is only approximately equal to the viscosity used in the Darcy drag term in (1-48) or (1-49). However, their relations are generally dependent on the porosity ε, as described by Prasad and Kladias[180] for non-Darcy convection problems. A rigorous theoretical development of the Forchheimer equations has been presented by Whitaker[239]. Misleading definitions of the Forchheimer constant in (1-29) have been pointed out by Nield[156].

REMARK 3: The EOS and constitutive equations introduced above describe correlations for density ρ, enthalpy h_e, and viscosity μ, which are applicable for temperatures of water below its critical value, i.e., $T \leq 374.15$ °C. For flow modeling of deep geothermal

brines in hot, high-pressure, supercritical regimes, extended and more general relationships are required, which are described by Palliser and McKibbin[170,171,172].

1.3 Convection Phenomena

1.3.1 Double-diffusive (thermohaline) convection

Double-diffusive convection (DDC) is a fundamental fluid dynamic process[20] and can also be recognized in porous-media problems[157]. It represents a buoyancy-driven transport process, which is simultaneously coupled by more than one diffusing property (chemical substances, thermal energy). For the DDC phenomenon to occur, the following three conditions must be met: (1) there should be a vertical gradient in two or more properties affecting the fluid density (e.g., concentrations of chemical species, temperature), (2) the resulting gradients in the fluid density must have opposing signs, and (3) the diffusivities of the properties must be different. In Fig. 1.2, ρ_1 and ρ_2 denote the distribution of density components to the two different properties mentioned above, and $\rho = \rho_1 + \rho_2$ denotes the total density distribution.

A striking feature of DDC is that instabilities can arise even when the total density is increasing downwards. A class of DDC phenomena is of particular practical interest in the subsurface: the so-called *thermohaline flows* where the stratifying properties are heat and salt (one component $\omega = \omega_k$ for $k = 1$). Here, heat is associated with the larger diffusivity value.

The most surprising and often counter-intuitive features of DDC phenomena are[223]: (a) they often occur in systems which are hydrostatically stable, i.e., the total density of the fluid increases with depth, (b) large vertical fluid motions can be produced, and (c) the potential energy always decreases and therefore the vertical density gradient increases. Commonly two different main scenarios can be distinguished. Either a *diffusive regime* develops if the destabilizing potential results from the component with the larger diffusivity (e.g., a stable salinity gradient is heated from below, Fig. 1.3a), or a *finger regime* forms if the driving (destabilizing) forces are caused by the more slowly diffusing component (e.g., a heated saline fluid on top of a stable temperature gradient, Fig. 1.3b). Both regimes can also emerge in a different form denoted as *mixed DDC regime* if both properties can destabilize (Fig. 1.3c), or completely stabilize (Fig. 1.3d) the fluid motion. For such thermohaline processes with four property ranges (hot-cold/light-heavy) and two (top-bottom) configurations there are $4^2 = 16$ combinations, of which the cases shown in Fig. 1.3 are the most typical.

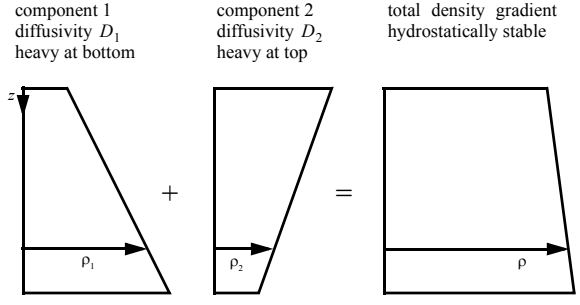

Figure 1.2 Two density components ρ_1 and ρ_2 (with different diffusivities $D_1 \neq D_2$) and total density ρ as a function of depth (modifiedfrom Turner[223]).

The diffusive and finger regimes can be further subdivided into the *subcritical* and *supercritical* categories. Supercriticality means that the driving (destabilizing) force exceeds the restoring (stabilizing) force[89]. For instance, in a diffusive regime a destabilizing, thermal influence would overcome the stabilizing influence of a heavy saline fluid. In contrast, in a subcritical configuration the restoring forces are dominant, i.e., the total density of the system remains stably stratified. However, it is a fascinating feature that DDC flow can in fact take place under statically stable circumstances because of the possibilities for subcritical instabilities. These instabilities can occur because of the phase lag between salt and thermal influences on the flow field, which are due to the difference in the diffusivities. The subcritical mechanism is described in detail by Turner[222]. A typical DDC phenomenon in a subcritical regime represents a staircase pattern, which is shown further below.

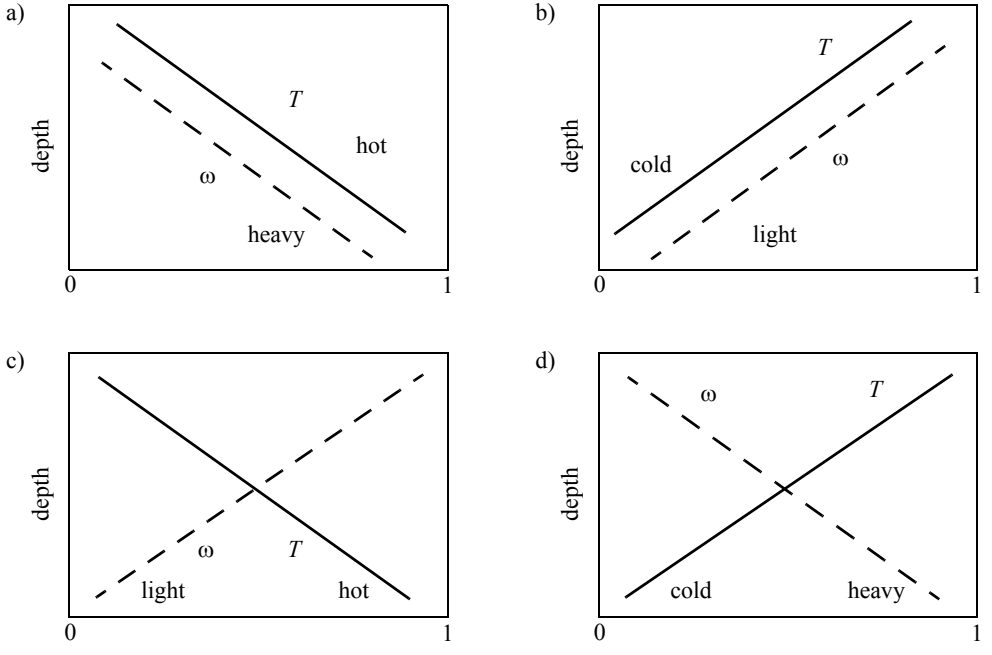

Figure 1.3 Depth profiles of temperature T and salt ω for different DDC regimes: a) diffusive regime, b) finger regime, c) mixed regime: both components acting in destabilizing manner, d) mixed regime: completely stabilized situation (from Hansen and Yuen[89]).

From a dimensional analysis of the governing balance equations (1-46) to (1-50b), the following characteristic numbers can be derived for the Darcy flow to characterize the convection processes:

Rayleigh number Ra:

$$Ra = \frac{\Delta\rho k_r k g d}{\mu D} \tag{1-56a}$$

where $\Delta\rho$ is a density difference, k is the permeability, d is a characteristic length (height), and D is the diffusivity as defined below. Assuming a linear equation of state for ρ (i.e., no variable density expansion, $\beta = \text{const.}$), and neglecting pressure effects ($\gamma = 0$), the following definitions of the Rayleigh number for solutes and thermal energy are useful:

solutal Rayleigh number Ra_s

$$Ra_s = \frac{\alpha\Delta\omega K d}{D_s} \qquad \text{with} \qquad D_s = \|\boldsymbol{D}\| \tag{1-56b}$$

thermal Rayleigh number Ra_t

$$Ra_t = \frac{\beta\Delta T K d}{D_\lambda} \qquad \text{with} \qquad D_\lambda = \|\Lambda\|/(\rho c^l) \tag{1-56c}$$

where $\Delta\omega$ and ΔT are differences of mass fraction and temperature, respectively, and $K = k_r k \rho_0 g/\mu_0$ corresponds to an effective hydraulic conductivity. According to (1-51), K, D_s and D_λ are considered as dependent on the saturation s for unsaturated porous media.

Lewis number Le

$$Le = \frac{D_\lambda}{D_s} \tag{1-57}$$

Buoyancy or Turner number B

$$B = \frac{Ra_s}{Le Ra_t} = \frac{\alpha\Delta\omega}{\beta\Delta T} \tag{1-58}$$

Applications of thermohaline flow in porous media can be found in the field of geothermics or waste disposal in salt formations[68,61,162]. Thermohaline effects are important, in particular, for the production of mineralized thermal water, the re-injection of cooled brine into warm deep aquifer layers as part of geothermal extraction technologies, and groundwater movement near salt domes.

DDC in the subcritical regime can lead to layering from an initially unlayered state. Such a phenomenon, also known as a staircase pattern, mainly depends on the Turner number B. Figure 1.4 illustrates a thermohaline flow situation in a square, two-dimensional porous cavity for a case with $Ra_t = 400$, $B = 2$ and $Le = 100$ revealing a typical staircase in the vertical salinity distribution with its accompanying temperature and streamline patterns.

REMARK 4: The Rayleigh number is derived under the assumption of homogeneous parameters. As pointed out by Schincariol[193] and Simmons *et al.*[206], a representative Rayleigh number which qualifies the convection process for heterogeneous or layered porous media does not exist. They addressed the inap-

propriateness of averaging spatially variable properties into single-valued parameters. Furthermore, the characteristic length d is difficult to determine in real-world situations. However, for rough calculations an effective Rayleigh number can be introduced as given by Nield[155].

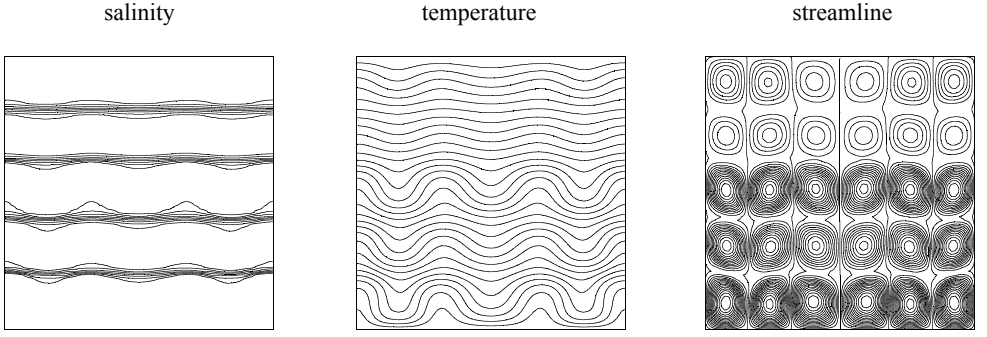

Figure 1.4 Salinity, temperature and streamline fields for a staircase situation of a thermohaline flow in a two-dimensional square cavity at $Ra_t = 400, B = 2, Le = 100$ simulated by FEFLOW[44]. Salinity consists of five distinct layers with the heavy material on the bottom. The hot temperature is on the bottom too.

1.3.2 Oberbeck-Boussinesq (OB) approximation and its extension

The system of balance equations (1-46) to (1-50b) is coupled by the nonlinearity in ρ. Its analysis can be substantially simplified by the so-called Oberbeck-Boussinesq (OB) approximation, sometimes termed only as Boussinesq approximation. As pointed out in[107,157] the term OB approximation seems more appropriate because Oberbeck (1879) addressed this problem before Boussinesq (1903).

The OB approximation consists in neglecting all density dependencies in the balance terms, except for the crucial buoyancy term $\rho \boldsymbol{g}$ which is retained in the momentum equation (1-48) (or (1-52) and (1-53)). Referring to saturated and nondeformable porous media and considering no sinks/sources, the fluid mass conservation (continuity equation) (1-46) reduces to $\nabla \cdot \boldsymbol{q} = 0$ and the velocity $\boldsymbol{q}$ becomes *solenoidal*, or divergenceless. This incompressibility assumption is common in most analytical and stability analyses of convection problems. The OB approximation is valid if density changes $\Delta\rho$ remain small in comparison to the reference density ρ_0. Obviously, the OB approximation becomes invalid for large density variations, e.g., at high-concentration brines and/or high temperature gradients. However, it is often not clear what consequences practically result if the full dependencies are incorporated (so-called *non-Boussinesq effects*).

Usually, extensions to non-Boussinesq formulations can be introduced by 'correction' terms written, for instance, for the continuity equation (1-46) in the following form

$$\rho \nabla \cdot \boldsymbol{q} = Q_{EB}$$
$$Q_{EB} = Q - \boldsymbol{q} \cdot \nabla \rho - \left[\varepsilon s \frac{\partial \rho}{\partial t} + \rho \left(s \Upsilon \frac{\partial p}{\partial t} + \varepsilon \frac{\partial s}{\partial t} \right) \right] \quad (1\text{-}59)$$

where Q_{EB} is the extended Boussinesq approximation term (sink/source) as used in[44,49] for saturated porous media. Kolditz *et al.*[126] compared OB solutions and some extended forms for the Elder cellular convection problem at a Rayleigh number of 400. For this case, OB solutions became similar to non-Boussinesq ones. However, there were differences in pressure and salinity distributions in parts of the model domain. Gartling and Hickox[77] studied adjustments for the variation of fluid properties in the heat transport equation numerically, while assuming the constraint of incompressibility, $\nabla \cdot \boldsymbol{q} = 0$. They found that the OB and their extended solutions can be sufficiently 'close' for integrated quantities over large temperature ranges. However, differences can occur for local quantities. The accurate prediction of the flow field has been shown to be of major concern, and they concluded that the 'goodness' of the OB solutions depends on what quantities are of interest in the problem solution.

Non-Boussinesq solutions require accurate numerical strategies. It is particularly important how the incompressibility terms in the continuity equations (1-46) (or (1-59)) are actually approximated. A small lack in discrete conservativity can mimic a non-Boussinesq influence, which is higher than in the real physical system, i.e., non-Boussinesq terms are overestimated. The numerical accuracy of the local velocity field obviously plays a dominant role, as will be discussed in section 1.4.3.

1.3.3 Stability analysis of the Horton-Rogers-Lapwood (HRL) problem

The Horton-Rogers-Lapwood (HRL) problem is the porous-medium analog of the Rayleigh-Bénard cellular convection problem, which was first analyzed by Horton and Rogers[114] and independently by Lapwood[136]. It refers to an infinite horizontal porous layer which is uniformly heated from below. In the original HRL problem formulation the porous medium is assumed homogeneous and isotropic. It is further assumed that the Darcy law and the OB approximation are valid. The HRL problem is the paradigm for the stability analysis of natural (free) convection in porous media. Nield[154] and Nield and Bejan[157] review the most important works in this field. We only extract the major outcome from the HRL analysis, which is important for our further discussion in the context of numerical works and benchmarks.

From a linear stability analysis a critical Rayleigh number $Ra_c = 4\pi^2$ is determined for which the conductive state remains stable (i.e., no convection) if $Ra < Ra_c$. Physical instability appears as convective flows when Ra is raised to Ra_c. Then, cellular motions with a horizontal wavenumber π result. The DDC (thermohaline) generalization of the HRL problem was studied by Nield[153]. The onset of free convection is similarly characterized by a critical Rayleigh number, which is given here as $Ra_c = Ra_s + Ra_t = 4\pi^2$. The

HRL problem was extended by Beck[16] to finite lengths in a three-dimensional porous box, showing dependencies of the convection criteria on the geometric aspect ratio. Other extensions refer to influences on boundary conditions, mechanical dispersion, anisotropic media, layered and sloped structures[29,31,107,157].

1.3.4 Oscillatory convection and bifurcation

The nonlinear theory in using perturbation approaches gives further insight into the behavior of the free convection process at higher Rayleigh numbers. The stability of the finite-amplitude two-dimensional rolls in square cross-sections was investigated by Straus[212], who showed that at a given Rayleigh number of less than 380, there is a limited band of wave numbers for which two-dimensional rolls are stable. A balloon shaped curve, displayed in a Rayleigh number versus wavenumber plane, separates regions of stable and unstable two-dimensional rolls. A stable roll represents a steady convection while an unstable roll indicates bifurcation to unsteady (oscillatory) two-dimensional or steady three-dimensional convection. From Straus' analysis the Rayleigh number of 380 can be considered as an upper limit of a second critical Rayleigh number.

Numerous numerical studies have been performed to examine the criteria for the onset of convection and to analyze the behavior at high Rayleigh numbers; for a review see, e.g.,[107,154,157]. The main results can be summarized as follows:

* For Rayleigh numbers $Ra < Ra_{c1} = 4\pi^2$ a pure conduction (diffusion) solution results and there is no convection. Ra_{c1} is the first critical Rayleigh number, where the motionless solution loses stability and stationary convection takes over when the Rayleigh number crosses this limit.

* In a range between $4\pi^2 < Ra < (240 \text{ to } 300)$ a stable convergent solution develops and various steady-state flows have been observed: two-dimensional rolls rotating in clockwise or counter-clockwise direction, three-dimensional rolls and three-dimensional polyhedral cells. A second critical Rayleigh number $Ra_{c2} \approx 240 \text{ to } 300$ is identified as an upper limit.

* For $Ra > Ra_{c2}$ the convection regime is unstable and characterized by a transition to an oscillatory (fluctuating) and transient convection behavior. The oscillations arise from instabilities of boundary layers as modeled in[112,113]. They can be interpreted as the continuous creation and disappearance of convective cells. We note that the numerical studies predicted a lower second critical Rayleigh number for the transition to unstable convection in comparison to Straus' result. Perturbations can result in manifold solutions (bifurcations). Possibly, the convection possesses different solutions and a numerical simulation converges to only one solution. As already observed by Horne and O'Sullivan[112] there is a possibility of either a steady multicellular structure or a fluctuating unicellular structure. Once formed, these two structures are not easily interchangeable, but the system may be assisted into either mode by a suitable perturbation during its early development. Higher-order transitions have been studied by Caltagirone *et al.*[24] and Caltagirone and Fabrie[23] for a two-dimensional square porous cavity. They showed that a second bifurcation exists, occurring at $Ra = 390$. At this Rayleigh number the flow becomes periodic.

Between 390 and 600 the process is single-periodic. Increasing Ra further, the flow is again periodic up to $Ra = 1000$. A quasi-periodic regime can maintain up to $Ra = 1500$, after which the single convecting roll splits into two unsteady cells by entering a chaotic restructuring (i.e. fluctuating) regime. Techniques of bifurcation theory have been used in two dimensions, among others, by Riley and Winters[187], Vadasz[226] and Vadasz and Olek[227,228,229]. Vadasz and Olek[229] pointed out the significance of including a time derivative term in the Darcy equation when studying wave (oscillatory) phenomena.

For sufficiently high Rayleigh numbers the flow regime can become physically unstable. This is triggered and controlled by perturbations. Such perturbations can have true physical meaning or can be purely numerical. Leijnse and Oostrom[139] have shown the influence of the numerical scheme, and the spatial and temporal discretization on the onset of instabilities and the final solution. It becomes clear, that accuracy and stability of the numerical solution approach are essential here. The conflict that arises from a certain mathematical solution of such a class of problems was already indicated by Horne and Caltagirone[111] who concluded: '*This nonlinear problem has a plethora of possible alternative flow regimes and histories depending on the conditions applied initially and subsequently. Therefore the too-perfect conditions that are achieved using analytical or numerical techniques (paradoxically the most accurate ones in particular) may give rise to other artificial solutions that are divorced from the flow observed in noisy physical systems. ... It is perhaps time to admit that mathematical solutions to nonlinear problems must of necessity include non-deterministic forcing effects in order to avoid solutions mathematically correct but physically unlikely.*' The more it is important, first, to take into account all relevant processes that occur in the physical system and, second, to fully explore the structure of the solution to the mathematical model, which enables the possible states of the system to be determined.

1.4 Numerical Approach

1.4.1 Finite elements and finite volumes

The conservation law system (1-46) to (1-50a) constitutes a nonlinear coupled set of initial-value partial differential equations which can be expressed in the general form

$$L(\boldsymbol{a}) = \boldsymbol{m}^T \frac{\partial(\boldsymbol{c}^T \boldsymbol{a})}{\partial t} + \nabla \cdot (\boldsymbol{f}^a + \boldsymbol{f}^d) - \boldsymbol{b} = 0 \qquad \text{(1-60)}$$

$$\text{on} \qquad \Omega \subset \Re^D, t \geq t_0$$

where $L(\boldsymbol{a})$ is a differential equation system written in terms of the state variable $\boldsymbol{a}(\boldsymbol{x}, t)$. It is expressed on the (physical) domain Ω, with the bounding closure $\partial\Omega$, lying on D-dimensional Euclidean space $\Re^D$, and for time t starting at, and proceeding from some initial time t_0. For the solution, appropriate boundary conditions are required on the entirety of $\partial\Omega$, and an initial condition on $\Omega \cup \partial\Omega$ is necessary. In (1-60) the following definitions are used

$$\boldsymbol{a} = \begin{Bmatrix} p \\ \omega_k \\ T \end{Bmatrix} \qquad \boldsymbol{c} = \begin{Bmatrix} 1 \\ \varepsilon s \rho \\ \varepsilon s \rho c^l + (1-\varepsilon)\rho^s c^s \end{Bmatrix} \qquad \boldsymbol{m} = \begin{Bmatrix} \rho_0 \gamma + \rho s \Upsilon (1-\varepsilon) \\ 1 \\ 1 \end{Bmatrix}$$

$$\boldsymbol{f}^a = \begin{Bmatrix} 0 \\ \rho \boldsymbol{q} \omega_k \\ \rho c^l \boldsymbol{q} T \end{Bmatrix} \qquad \boldsymbol{f}^d = \begin{Bmatrix} \rho \boldsymbol{q} \\ \boldsymbol{j}_k \\ \boldsymbol{j}_e \end{Bmatrix} \qquad \boldsymbol{b} = \begin{Bmatrix} Q - \rho_0 \left(\alpha \frac{\partial \omega_k}{\partial t} - \beta \frac{\partial T}{\partial t} \right) - \rho \varepsilon \frac{\partial s}{\partial t} \\ R_k + Q_k \\ H_e \end{Bmatrix} \tag{1-61}$$

where $\boldsymbol{f}^a$ and $\boldsymbol{f}^d$ are the advective and dispersive flux vectors. The fluxes $\boldsymbol{q}$, $\boldsymbol{j}_k$ and $\boldsymbol{j}_e$ contained in $\boldsymbol{f}^a$ and $\boldsymbol{f}^d$ are expressed in terms of (1-49) and (1-51) derived from the state variable $\boldsymbol{a}$. Their treatment is a specific point of consideration further below.

The coupled equation system (1-60) has to be solved for $\boldsymbol{a}$ by numerical methods. Popular and powerful strategies are the finite element method (FEM)[9,27,86,115,141,184,247], and the finite volume method (FVM)[65,174]. Both methods have the same mathematical basis starting from a weighted-integral formulation of the governing balance equations, *viz.*,

$$\int_\Omega w(\boldsymbol{x}, t) L(\tilde{\boldsymbol{a}}) d\tau = 0 \qquad \forall w \tag{1-62}$$

where $w(\boldsymbol{x}, t)$ is an arbitrary weighting (or test) function and $\tilde{\boldsymbol{a}}$ corresponds to an approximation of the state variable. The *weighted-residual statement* (1-62) represents a continuum form for constraining the errors in the state variable $\tilde{\boldsymbol{a}}$. The simplest choice for w is any constant which can be recognized as a subdomain collocation yielding the standard FVM expressions. More generally, Galerkin, Petrov-Galerkin and least-square statements are formulations in the FEM, where the Galerkin weighting is standard. In this methodology the FVM appears as a subclass and low-order realization of a FEM. Gresho and Sani[86] discuss the similarities, advantages, and disadvantages of the FEM and FVM in greater detail for fluid dynamic processes. In practice, however, there are many varieties in the numerical implementation of both FVM and FEM. Their comparison cannot be simply reduced to the ambiguous subject of 'local conservation'. As shown in[86], a Galerkin-based FEM exemplified for advection-dispersion equations does, indeed, display local conservation, both at the nodal level and at element level. The subject yields different viewpoints and it is important to recognize that local conservation does not imply local accuracy. [Note, while the FVM satisfies element-level (local) conservation even on a coarse and accordingly poor mesh, the solutions and the accompanying fluxes are here inexact obviously.] In general, local accuracy (and, therefore, the local conservation) is an important aspect that can significantly influence the overall solution. Accordingly, we prefer techniques and numerical resolutions, which provide the best local

accuracy even for complex geometries. In this paper we will focus on the FEM in more detail.

The finite-element formulation of the balance equation system (1-60) finally leads to a discrete matrix system written in the compact form

$$\boldsymbol{M}^T\dot{\boldsymbol{A}} + \boldsymbol{F}^T\boldsymbol{A} - \boldsymbol{B} = 0 \tag{1-63}$$

with the vectors of the discrete state variable

$$\dot{\boldsymbol{A}} = \begin{Bmatrix} \dot{\boldsymbol{p}} \\ \dot{\omega}_k \\ \dot{\boldsymbol{T}} \end{Bmatrix} \qquad \boldsymbol{A} = \begin{Bmatrix} \boldsymbol{p} \\ \omega_k \\ \boldsymbol{T} \end{Bmatrix} \qquad (k = 1, \ldots, N) \tag{1-64a}$$

and the submatrices

$$\boldsymbol{M} = \begin{Bmatrix} \boldsymbol{M}_\rho \\ \boldsymbol{M}_\omega(\boldsymbol{p}, \omega_k, \boldsymbol{T}) \\ \boldsymbol{M}_e(\boldsymbol{p}, \omega_k, \boldsymbol{T}) \end{Bmatrix} \qquad \boldsymbol{F} = \begin{Bmatrix} \boldsymbol{F}_\rho(\boldsymbol{q}, \boldsymbol{p}, \omega_k, \boldsymbol{T}) \\ \boldsymbol{F}_\omega(\boldsymbol{q}, \omega_k, \boldsymbol{T}) \\ \boldsymbol{F}_e(\boldsymbol{q}, \omega_k, \boldsymbol{T}) \end{Bmatrix} \tag{1-64b}$$

$$\boldsymbol{B} = \begin{Bmatrix} \boldsymbol{B}_\rho(\boldsymbol{q}, \boldsymbol{p}, \dot{\boldsymbol{p}}, \omega_k, \dot{\omega}_k, \boldsymbol{T}, \dot{\boldsymbol{T}}) \\ \boldsymbol{B}_\omega(\omega_k) \\ \boldsymbol{B}_e(\boldsymbol{T}) \end{Bmatrix}$$

revealing the inherent nonlinearities in parenthesis. The state vector $\boldsymbol{A}(t)$ contains vectors of pressure $\boldsymbol{p}$, mass ω_k and temperature $\boldsymbol{T}$ to be solved at discrete points. The dot indicates differentiation with respect to time t. The matrices $\boldsymbol{M}$, $\boldsymbol{F}$ and vectors $\boldsymbol{B}$ result from the spatial semi-discretization of the fluid mass, species mass and energy balance conservation equations, identified by the subscripts ρ, ω, and e, respectively.

The spatial semi-discretization resulting in the form of the combined matrix problem (1-63) assumes the separability of space $\boldsymbol{x}$ and time t, which is the usual approximation in the FEM and the FVM. It partitions the continuum domain Ω in local regions (finite elements, finite volume cells) of triangular, quadrilateral, tetrahedral and/or hexahedral shapes. The approach leads to a first-order ordinary differential equation (ODE) in time which can practically only be solved by numerical ODE schemes. Alternatively, we note that the time variable may be embedded in the trial space, which leads to discrete time-continuous space approximation, see e.g.[86] for a review and discussion. Such space-time formulations can have advantages in numerical accuracy and stability[175,176]; however, due to the complexity and increased numerical effort their application is clearly restricted. In practice, ODE strategies are common where for stability and efficiency reasons implicit (or explicit) two-stage techniques are preferred. The combination of ODE strategies with appropriate iterative methods for solving the nonlinear matrix system (1-63) is discussed next.

1.4.2 Strategies for solving the coupled spatio-temporal convection processes

Referring to two-stage transient ODE strategies we consider $\boldsymbol{A}(t)$ within the finite interval $(t_n, t_n + \Delta t_n)$, where the subscript n denotes the time level and Δt_n is a variable time step length. The solution state variable $\boldsymbol{A}(t)$ is defined as

$$\boldsymbol{A}^n = \boldsymbol{A}(t_n) \tag{1-65}$$

at the previous (old) time level and

$$\boldsymbol{A}^{n+1} = \boldsymbol{A}(t_n + \Delta t_n) \tag{1-66}$$

at the new time level. Introducing a weighting coefficient $(0 \le \theta \le 1)$ we find for the state variable and RHS in (1-63)

$$\left.\begin{aligned} \boldsymbol{A}(t_n + \theta\Delta t_n) &= \theta\boldsymbol{A}(t_n + \Delta t_n) + (1-\theta)\boldsymbol{A}(t_n) \\ \boldsymbol{B}(t_n + \theta\Delta t_n) &= \theta\boldsymbol{B}(t_n + \Delta t_n) + (1-\theta)\boldsymbol{B}(t_n) \\ \dot{\boldsymbol{A}}(t_n + \theta\Delta t_n) &= \theta\dot{\boldsymbol{A}}(t_n + \Delta t_n) + (1-\theta)\dot{\boldsymbol{A}}(t_n) = \frac{\boldsymbol{A}^{n+1} - \boldsymbol{A}^n}{\Delta t_n} \end{aligned}\right\} \tag{1-67}$$

where a backward difference approximation for $\dot{\boldsymbol{A}}(t_n + \Delta t_n)$ and a forward difference for $\dot{\boldsymbol{A}}(t_n)$ are used. Common time stepping schemes result if θ is chosen in an appropriate manner: $\theta = 1$ yields the (fully) implicit scheme, which is 1st order accurate in time, $\theta = \frac{1}{2}$ is the trapezoid rule (or Crank-Nicolson scheme), which is 2nd order accurate in time, and for $\theta = 0$ the scheme becomes (fully) explicit, only 1st order accurate in time. Inserting (1-67) into (1-63) the θ-implicit/explicit solution of the matrix equation results

$$\boldsymbol{R}^{n+1} = \left(\frac{\boldsymbol{M}^T}{\Delta t_n} + \boldsymbol{F}^T\theta\right)\boldsymbol{A}^{n+1} - \left(\frac{\boldsymbol{M}^T}{\Delta t_n} - \boldsymbol{F}^T(1-\theta)\right)\boldsymbol{A}^n \tag{1-68}$$

$$-(\boldsymbol{B}^{n+1}\theta + \boldsymbol{B}^n(1-\theta)) = \boldsymbol{0}$$

where $\boldsymbol{R}^{n+1}$ is the residual for the conservation law system at time stage $n+1$.

A powerful alternative to the two-stage θ-implicit/explicit solution (1-68) is the predictor-corrector method which is thoroughly described elsewhere[41,49,86,184]. In the context of convection problems, the fully implicit backward Euler (BE) scheme with 1st order accuracy, and the semi-implicit trapezoid rule (TR) with 2nd order accuracy are preferred. The time derivatives are approximated for the BE scheme by

$$\dot{\boldsymbol{A}}^{n+1} = \frac{\boldsymbol{A}^{n+1} - \boldsymbol{A}^n}{\Delta t_n} \tag{1-69a}$$

and for the TR scheme by

$$\dot{\boldsymbol{A}}^{n+1} = \frac{2}{\Delta t_n}(\boldsymbol{A}^{n+1} - \boldsymbol{A}^n) - \dot{\boldsymbol{A}}^n \tag{1-69b}$$

Inserting (1-69a) and (1-69b) into (1-63) yields the corrector solution in form of

$$\boldsymbol{R}^{n+1} = \left(\frac{\boldsymbol{M}^T}{\theta\Delta t_n} + \boldsymbol{F}^T\right)\boldsymbol{A}^{n+1} \tag{1-70}$$

$$-\boldsymbol{M}^T\left[\frac{\boldsymbol{A}^n}{\theta\Delta t_n} + \left(\frac{1}{\theta} - 1\right)\dot{\boldsymbol{A}}^n\right] - \boldsymbol{B}^{n+1} = \boldsymbol{0}$$

with $\theta = \frac{1}{2}$ for the TR scheme and $\theta = 1$ for the BE scheme. For automatic time stepping, predictor solutions are required that are explicit in time. Usually, an explicit forward Euler (FE) scheme of first order accuracy and an explicit Adams-Bashforth (AB) scheme of second order accuracy are used[49]. The resulting predictor-corrector methods are termed as forward Euler/

backward Euler (FE/BE) and Adams-Bashforth/trapezoid rule (AB/TR) schemes.

The spatial and temporal discretization result in a coupled system of algebraic equations (1-68) or (1-70), that must be solved iteratively due to its nonlinearity. As a simple and computational cheap method the successive substitution scheme, known as Picard or fix-point method, is often applied. When writing (1-68) or (1-70) in a compact form as

$$\boldsymbol{R}^{n+1} = \boldsymbol{K}(\boldsymbol{A}^{n+1})\boldsymbol{A}^{n+1} - \boldsymbol{Z}(\boldsymbol{A}^{n}) = \boldsymbol{0} \tag{1-71}$$

the Picard method linearizes the matrix system (1-71) at iteration τ as

$$\boldsymbol{R}_{\tau}^{n+1} = \boldsymbol{K}(\boldsymbol{A}_{\tau}^{n+1})\boldsymbol{A}_{\tau+1}^{n+1} - \boldsymbol{Z}(\boldsymbol{A}_{\tau}^{n}) \tag{1-72}$$

where the system matrix $\boldsymbol{K}$ and the RHS vector $\boldsymbol{Z}$ are evaluated from the previous iteration. The linearized problem is solved for $\boldsymbol{A}_{\tau+1}^{n+1}$ at a given time stage $n+1$ and iteration $\tau+1$. The iteration procedure is terminated if a convergence criterion is satisfied. Such a criterion can be a deviatoric (change) error measure, which is a standard test, in form of

$$\left\| \Delta \boldsymbol{A}_{\tau}^{n+1} \right\|_{L_p} < \delta \tag{1-73}$$

by checking the solution difference

$$\Delta \boldsymbol{A}_{\tau}^{n+1} = \boldsymbol{A}_{\tau+1}^{n+1} - \boldsymbol{A}_{\tau}^{n+1} \tag{1-74}$$

where δ is a chosen error tolerance and L_p identifies the error norm with $p = 2$ for the root-mean square (RMS) and $p = \infty$ for the maximum norm. Instead of testing deviatoric error measures, the reduction of the residual $\boldsymbol{R}_{\tau}^{n+1}(\boldsymbol{A})$ may be directly controlled[1,161], such as

$$\left\| \boldsymbol{R}_{\tau}^{n+1} \right\|_{L_p} < \delta \left\| \boldsymbol{B}^{n+1} \right\|_{L_p} \tag{1-75}$$

where an appropriate normalization of the residual (here with respect to the external sink/source term $\boldsymbol{B}^{n+1}$) is required.

The Picard iteration method converges linearly at best. For large systems it is not often a cost-effective method. Instead, for large and highly nonlinear systems the Newton (or Newton-Raphson) method that converges quadratically can be a more appropriate choice, e.g.,[182]. The Newton method constitutes the following iterative cycle,

$$\boldsymbol{A}_{0}^{n+1} = \boldsymbol{A}^{n} \qquad \boldsymbol{R}_{0}^{n+1} = \boldsymbol{R}^{n} \tag{1-76}$$

for $\tau = 0, 1, 2, \ldots$ until convergence

$$\boldsymbol{J}(\boldsymbol{A}_{\tau}^{n+1})\Delta \boldsymbol{A}_{\tau}^{n+1} = -\boldsymbol{R}_{\tau}^{n+1} \tag{1-77}$$

with the Jacobian $\boldsymbol{J}$ as

$$\boldsymbol{J}(\boldsymbol{A}_{\tau}^{n+1}) = \frac{\partial \boldsymbol{R}_{\tau}^{n+1}(\boldsymbol{A}_{\tau}^{n+1})}{\partial \boldsymbol{A}_{\tau}^{n+1}} \tag{1-78}$$

The iteration process at a time stage $n+1$ is terminated if a convergence in form of either (1-73) or (1-75) is achieved, where the residual criterion (1-75) appears as

a natural test for the Newton scheme. Modified or Quasi-Newton approximations[60] amount to the use of simplified forms of the Jacobian $\boldsymbol{J}(\boldsymbol{A}_{\tau}^{n+1})$, that are, however, no longer quadratically convergent.

Convergence of an iteration procedure requires initial estimates $\boldsymbol{A}_0^{n+1}$ not too far from the actual solution $\boldsymbol{A}^{n+1}$. The Picard method has a reasonably large convergence radius, but the rate of convergence is generally fairly slow. On the other hand, the Newton method is rather sensitive with respect to the initial guess. For steady-state problems and problems with strong nonlinearities a good initial guess is often not available and the iterative algorithm can completely fail. Sometimes relaxation in the variables can overcome these difficulties as shown in[41,50]. In the context of convection problems, steady-state solutions may not exist, making the full transient solution procedure necessary. In time-dependent simulations it is possible to find an initial guess close enough to the solution, so that the Newton iterations converge quadratically to the solution. This is feasible with a proper adaptation of the timestep size Δt_n to the evolving flow characteristics. In this way, the nonlinear solution process becomes dependent on, and controlled by, the timestep. Unfortunately, the iteration and timestep controls are often performed fully empirically, where heuristic rules are employed to increase or decrease the timestep according to an iteration success (e.g.,[1]). In contrast, an automatic and error-controlled adaptive time selection strategy based on a predictor-correction scheme can follow the 'physics' more intelligently and has been shown to be powerful and efficient for the present class of nonlinear problems, see, e.g.,[41,49]. The adaptive predictor-corrector scheme monitors the solution process via a local time truncation error estimate in which the timestep size Δt_n is cheaply and automatically varied in accordance with temporal accuracy requirements. In this procedure the timestep is increased whenever possible and decreased only if necessary. Mathematical details can be found in[41,49,52,86,184] and the references listed there.

The matrix system written in form of Eqs. (1-63) and (1-71) is fully *coupled* and the algebraic equations have to be solved *simultaneously* for pressure $\boldsymbol{p}$, mass $\boldsymbol{\omega}_k$ and temperature $\boldsymbol{T}$. An advantage of such a simultaneous solution is the strong coupling for high-density flow which leads to an improved rate of convergence, provided that Newton techniques are incorporated. Such a coupled iterative strategy has been preferred by Herbert *et al*.[101] and Oldenburg and Pruess[161] for transient two-dimensional density-dependent solute (one-species) convection problems. However, the solution of (1-71) in a direct and simultaneous manner is still not generally applicable to large, mass (multi-species) and heat-dependent, geometrically complex, three-dimensional problems because of the significant memory and/or computational burden of the formulation. The resulting system matrix for a simultaneous solution can be ill-conditioned due to the significantly different scales of the processes involved. In order to reduce the computational requirement, a *decoupled* solution strategy is considered, in which the equations are solved *sequentially* in a staggered or cyclic iteration between the equation sets for pressure $\boldsymbol{p}$, species mass ω_k and temperature $\boldsymbol{T}$, such as

$$\left.\begin{aligned}
\boldsymbol{R}_{\rho}^{n+1}(\boldsymbol{p},\omega_k,\boldsymbol{T}) &= \boldsymbol{K}_{\rho}(\boldsymbol{p}^{n+1},\omega_k^{n+1},\boldsymbol{T}^{n+1})\boldsymbol{p}^{n+1}-\boldsymbol{Z}_{\rho}(\boldsymbol{p}^{n},\omega_k^{n+1},\boldsymbol{T}^{n+1}) &&= \boldsymbol{0}\\
\boldsymbol{R}_{\omega}^{n+1}(\boldsymbol{p},\omega_k,\boldsymbol{T}) &= \boldsymbol{K}_{\omega}(\boldsymbol{p}^{n+1},\omega_k^{n+1},\boldsymbol{T}^{n+1})\omega_k^{n+1}-\boldsymbol{Z}_{\omega}(\boldsymbol{p}^{n},\omega_k^{n+1},\boldsymbol{T}^{n+1}) &&= \boldsymbol{0}\\
\boldsymbol{R}_{e}^{n+1}(\boldsymbol{p},\omega_k,\boldsymbol{T}) &= \boldsymbol{K}_{e}(\boldsymbol{p}^{n+1},\omega_k^{n+1},\boldsymbol{T}^{n+1})\boldsymbol{T}^{n+1}-\boldsymbol{Z}_{e}(\boldsymbol{p}^{n},\omega_k^{n+1},\boldsymbol{T}^{n+1}) &&= \boldsymbol{0}
\end{aligned}\right\} \tag{1-79}$$

One particular disadvantage of (1-79) is obvious: While the Newton method can be applied separately for each of the three subsystems of equations, the quadratic-convergence property of the Newton scheme is lost for the overall system solution. In the decoupled/iterative strategy Picard-type iterations are usually applied to linearize the complete equations (1-79), e.g.,[1,109,117,126,164,232]. Alternatively, a mixed Newton-Picard iteration scheme is also possible, as implemented in the FEFLOW simulator[44], where the nonlinear dependence on the main variable is subjected to a Newton method, while the dependency on the remaining variables is linearized by a cyclic Picard-type approximation. It can be considered as a partial Newton scheme[182], which reads as

$$\left.\begin{aligned}
\boldsymbol{J}_{\rho}(\boldsymbol{p}_{\tau}^{n+1},\omega_{k\tau}^{n+1},\boldsymbol{T}_{\tau}^{n+1})\Delta\boldsymbol{p}_{\tau}^{n+1} &= -\boldsymbol{R}_{\rho\tau}^{n+1} \qquad \boldsymbol{J}_{\rho}(\boldsymbol{p}_{\tau}^{n+1},\omega_{k\tau}^{n+1},\boldsymbol{T}_{\tau}^{n+1}) = \frac{\partial \boldsymbol{R}_{\rho\tau}^{n+1}(\boldsymbol{p}_{\tau}^{n+1},\omega_{k\tau}^{n+1},\boldsymbol{T}_{\tau}^{n+1})}{\partial \boldsymbol{p}_{\tau}^{n+1}}\\
\boldsymbol{J}_{\omega}(\boldsymbol{p}_{\tau}^{n+1},\omega_{k\tau}^{n+1},\boldsymbol{T}_{\tau}^{n+1})\Delta\omega_{k\tau}^{n+1} &= -\boldsymbol{R}_{\omega\tau}^{n+1} \qquad \boldsymbol{J}_{\omega}(\boldsymbol{p}_{\tau}^{n+1},\omega_{k\tau}^{n+1},\boldsymbol{T}_{\tau}^{n+1}) = \frac{\partial \boldsymbol{R}_{\omega\tau}^{n+1}(\boldsymbol{p}_{\tau}^{n+1},\omega_{k\tau}^{n+1},\boldsymbol{T}_{\tau}^{n+1})}{\partial \omega_{k\tau}^{n+1}}\\
\boldsymbol{J}_{e}(\boldsymbol{p}_{\tau}^{n+1},\omega_{k\tau}^{n+1},\boldsymbol{T}_{\tau}^{n+1})\Delta\boldsymbol{T}_{\tau}^{n+1} &= -\boldsymbol{R}_{e\tau}^{n+1} \qquad \boldsymbol{J}_{e}(\boldsymbol{p}_{\tau}^{n+1},\omega_{k\tau}^{n+1},\boldsymbol{T}_{\tau}^{n+1}) = \frac{\partial \boldsymbol{R}_{e\tau}^{n+1}(\boldsymbol{p}_{\tau}^{n+1},\omega_{k\tau}^{n+1},\boldsymbol{T}_{\tau}^{n+1})}{\partial \boldsymbol{T}_{\tau}^{n+1}}
\end{aligned}\right\} \tag{1-80}$$

with increments

$$\Delta\boldsymbol{p}_{\tau}^{n+1} = \boldsymbol{p}_{\tau+1}^{n+1}-\boldsymbol{p}_{\tau}^{n+1} \qquad \Delta\omega_{k\tau}^{n+1} = \omega_{k(\tau+1)}^{n+1}-\omega_{k\tau}^{n+1} \qquad \Delta\boldsymbol{T}_{\tau}^{n+1} = \boldsymbol{T}_{\tau+1}^{n+1}-\boldsymbol{T}_{\tau}^{n+1} \tag{1-81}$$

In combination with an adaptive predictor-corrector time-stepping control, a one-step Newton method appears as a cost-effective alternative in solving the system (1-80)[49]. It can be argued that the required degree of convergence has to be satisfied in just one full Newton iteration $\tau = 0$ per timestep. In doing so, the time-discretization error can also be used as the Newton convergence criterion δ for the iterate τ. Equations (1-80) are then linearized by using the corresponding predictors, *viz.*,

$$\boldsymbol{p}_{\tau=0}^{n+1} = \boldsymbol{p}_{p}^{n+1} \quad \omega_{k(\tau=0)}^{n+1} = \omega_{kp}^{n+1} \quad \boldsymbol{T}_{\tau=0}^{n+1} = \boldsymbol{T}_{p}^{n+1} \tag{1-82}$$

where the subscript p indicates the predictor values at the new time level $n+1$. Note, that the predictor linearization refers to both the Newton and Picard expressions in (1-80), which further improves the decoupled/iterative partial Newton solution.

In the above spatio-temporal discrete formulation and its solution we implicitly assumed that the fluxes $\boldsymbol{q}$, $\boldsymbol{j}_k$, and $\boldsymbol{j}_e$ can be derived from the state variables $\boldsymbol{A}(t)$ for pressure $\boldsymbol{p}$, species mass ω_k and temperature $\boldsymbol{T}$. Various numerical strategies are possible but only a small subset of techniques appears to be practicable and numerically satisfactory for density-coupled processes. Particularly, at a high-density coupling the numerical accuracy of the fluxes is essential for a physically correct modeling of a convection. A rigorous method would be an incorporation of the flux equations (1-49) and (1-51) for $\boldsymbol{q}$, $\boldsymbol{j}_k$, and $\boldsymbol{j}_e$ into the weighted-residual form (1-62), where the state variable $\boldsymbol{a}$ has to be extended by the corresponding flux entities. The flux components then appear as additional primary variables. Indeed, there have been such attempts for two dimensions and coupled solute (one-species) transport by Segol and Pinder[202], Segol *et al.*[203], Huyakorn and Taylor[116], Diersch[38,39,40] and Herbert *et al.*[101]. Due to the increased numerical effort and the inherent difficulties in formulating boundary conditions for flux components (q_x, q_y, q_z) on general (curved) geometries, the coupled strategy with a full set of primary flux variables is now considered as widely impractical and computationally too expensive.

A more efficient and widely practiced alternative is the evaluation of the fluxes in a decoupled manner. The standard technique is to *directly differentiate* the solution at points of interest. For instance, the local Darcy fluxes $\boldsymbol{q}$ from (1-49) or (1-52) are calculated by differentiating the pressure p and using the appropriate constitutive relations (1-51). It results, however, in discontinuous derivatives with a lower-order accuracy (compared to the accuracy of the pressure) across element (volume cell) boundaries, and at interelement local points (nodes), where accurate values of fluxes are usually desired. However, the order of accuracy of the fluxes obtained from different schemes depends on the particular schemes. Direct differentiation with a FEM scheme in which the pressure is interpolated with high-order polynomials, e.g. Herbert et al.[101], could lead to fluxes that have a higher order of accuracy than a scheme in which the fluxes are treated as primary variables, but are interpolated linearly. Note that although the derivatives of the pressure are discontinuous normal to an interface between elements, they are generally continuous tangential to the interface.

To achieve accurate derivatives, local and global *projection* (smoothing) techniques[86] are applied which lead to a continuous representation of the fluxes throughout the solution domain $\Omega \cup \partial\Omega$. As further discussed in[47,49] for the FEM the local projection procedure consists of an extrapolation from the appropriate Gaussian points and a subsequent averaging at nodes. Derivatives at Gauss points are known to be superconvergent, e.g. as in[142], where the accuracy in the first derivative of the finite element solution is better by an order than in a general point. Global projection assumes a continuous interpolation of the derivatives of the same form as that used for the finite-element basis functions. This is identical with a Galerkin-

weighting formulation of the momentum balance equation (1-49) or (1-52), as proposed by Yeh[245], and used by Galeati *et al*.[76] and Herbert *et al*.[101] for density-dependent groundwater flows. Diersch[41,43] and Diersch and Kolditz[49] used projection techniques successfully in various benchmark tests; however, recently a critical revision of the derivative computation became necessary[47], which will be discussed separately in the following section.

A promising alternative in computing fluxes of higher accuracy is given by *mixed FEM* as recently applied to two-dimensional density-dependent solute (one-species) transport in porous media by Ackerer *et al*.[1], Bués and Oltean[22], Oltean and Bués[164], and Mazzia *et al*.[144]. Holstad[105] used a mixed FEM and FVM for two-dimensional temperature-driven flow in porous media. A mixed form of the governing flow and transport equations is constructed by a weighted-integral formulation with vectorial test and basis functions having the properties of the so-called Raviart-Thomas space[21,183]. A mixed FEM naturally results in a directly coupled matrix system with fluxes as primary variables which significantly increases the number of unknowns. The fluxes are approximated across the edges of each finite element for a better control of the (local) conservativity. Applying lowest-order Raviart-Thomas elements and averaged quantities at edges, the flux field is constant over each element[164]. The normal flux component at the edges can be discontinuous. The greatest limitation of mixed FEMs is their higher computational effort in comparison to standard FEM and the non-positive definite matrix property which is not amenable to iterative equation solvers. To overcome these drawbacks, hybrid formulations are introduced which decouple the flux equations and lead to a symmetric and positive definite matrix system[17,27,57]. By hybridization the direct coupling of the flux degrees of freedom between elements along the edges is removed. The fluxes remain indirectly coupled through an extra set of explicit constraints. The overall approach is termed as *mixed hybrid FEM*.

The above procedures (direct differentiation, local/global projection, mixed hybrid FEM) can be applied not only to compute the Darcy fluxes $\boldsymbol{q}$, but also for the mass fluxes $\boldsymbol{j}_k$ and heat fluxes $\boldsymbol{j}_e$, which are driven by the mass ω_k and temperature T variables. If the equations are nonlinear, particularly in form of the DBF flow model (1-49) and the non-Fickian dispersion law (1-9), the decoupled formulation requires a suitable iterative treatment. For instance, an iterative scheme is used in[44] for evaluating the non-Fickian fluxes (without Soret effects $\boldsymbol{D}_\lambda^* \equiv \boldsymbol{0}$) in the following way:

$$\left.\begin{array}{ll} \text{0. initial} & \boldsymbol{j}_{k0}^{n+1} = \boldsymbol{0} \\ \tau\text{. step} & \boldsymbol{j}_{k\tau}^{n+1} = -\dfrac{\rho \boldsymbol{D}}{\Im_H \left\| \boldsymbol{j}_{k\tau-1}^{n+1} \right\| + 1} \cdot \nabla \omega_{k\tau}^{n+1} \end{array}\right\} \qquad (1\text{-}83)$$

The iteration (1-83) has to be performed at each timestep $n+1$. For an adaptive predictor-corrector time marching scheme the nonlinear solution is fully controlled by the timestep itself, where the nonlinear dispersion is linearized in time according to

$$\boldsymbol{j}_k^{n+1} = -\frac{\rho \boldsymbol{D}}{\Im_H \left\| \boldsymbol{j}_k^n \right\| + 1} \cdot \nabla \omega_k^{n+1} \qquad (1\text{-}84)$$

If the fluxes are represented by linear relationships, as

by the standard Darcy law (1-52), the Fickian law (1-7) and the Fourier law (1-13), they can be substituted in the balance equation set and explicitly expressed by their state variables of the pressure p, species mass ω_k and temperature T. However, the Darcy flux $\boldsymbol{q}$ also appears in the advective and mechanical dispersion terms of the mass and heat transport equations and must be evaluated separately. Its computations have to be done carefully for density-dependent processes and need further specific considerations.

1.4.3 Consistent velocity approximation

In the Darcy law (1-52) the discretization of the fluxes (velocities) $\boldsymbol{q}$ is nontrivial if density effects become important. Specifically, a lower-order approximation attainable for the pressure gradients ∇p can conflict with a high-order spatial variation in the gravity (buoyancy) term $\rho \boldsymbol{g}$ due to the following reasons. There may be significant parts of the domain where the Darcy velocity should be zero (or very small). In these regions, there should be a balance between two contributions to the Darcy velocity: the pressure gradient term and the density term. However, if the pressure and the concentration are approximated using finite-element approximations based on the same order of polynomials, then the pressure gradient term is a lower-order polynomial in position, and therefore cannot in general match the variation with position of the gravity term, which varies with position in the same way as the concentration. As a result, although the Darcy velocity may be zero in some average sense over an element, it varies on the scale of the elements. These artificial variations may have a major effect on the calculated solute transport, both because they may lead to advection of solution and also because they may lead to increased dispersion.

This problem has been addressed by Voss[231], Voss and Souza[233], Herbert *et al.*[101] and Leijnse[137] who proposed modified schemes, termed *consistent velocity approximation*, for evaluation of the discontinuous derivatives. In Voss and Souza's approach the spatial variation in the gravity term is reduced to the same spatial variation as occurring in the pressure gradient, i.e., for linear finite elements the pressure gradient is constant (piecewise constant per element) and accordingly, the gravity term should be also piecewise constant. Leijnse extends this procedure and prefers averages of the buoyancy term only in the appropriate gravity direction. While Voss and Souza[233] and Leijnse[137] tried to overcome the problem of consistency by precision reduction, Herbert *et al.*[101] solved it by introducing a second-order approximation for the pressure (quadratic basis functions) and a linear-order approximation for the solute (linear basis functions). Unfortunately, their approach significantly raises the computational expense.

1.4.3.1 The hydrostatic condition: The requirement of consistency

Consider the following hydrostatic situation as proposed by Knabner and Frolkovic[131] for a finite element shown in Fig. 1.5. For the sake of simplicity, the interval Δz is [0,1]. We assume the density ρ is varying linearly in the z-direction of gravity, *viz*,

$$\rho = \rho_o + (\rho_1 - \rho_o) z \qquad z \in [0, 1] \tag{1-85}$$

For the simple vertical problem the Darcy velocity for saturated conditions ($k_r \equiv 1$) is

$$\left.\begin{aligned} q_x &= -\frac{k_{xx}}{\mu}\partial_x p \\ q_y &= -\frac{k_{yy}}{\mu}\partial_y p \\ q_z &= -\frac{k_{zz}}{\mu}(\partial_z p + \rho g) \end{aligned}\right\} \qquad (1\text{-}86)$$

Under a hydrostatic equilibrium the velocity vector $\boldsymbol{q}$ is (must be) zero everywhere. This is known as the *requirement of consistency*:

$$\boldsymbol{q} \equiv \mathbf{0}; \qquad \nabla p = \rho \boldsymbol{g} \qquad (1\text{-}87)$$

For the above example (Fig. 1.5) with a vertical density gradient we require

$$\partial_x p = \partial_y p = 0; \qquad \partial_z p = -\rho g \qquad (1\text{-}88)$$

while the pressure p has to satisfy the following relationship

$$p = p(z) = -g\int_{z_o}^{z} \rho(\theta)\, d\theta \qquad (1\text{-}89)$$

which yields

$$p = p_0 - g\left(\rho_o z + \frac{\rho_1 - \rho_o}{2} z^2\right) \qquad (1\text{-}90)$$

Equation (1-90) indicates that for a *linear* density ρ, a *quadratic* shape of the pressure p is required to maintain a hydrostatic equilibrium for all z in the interval.

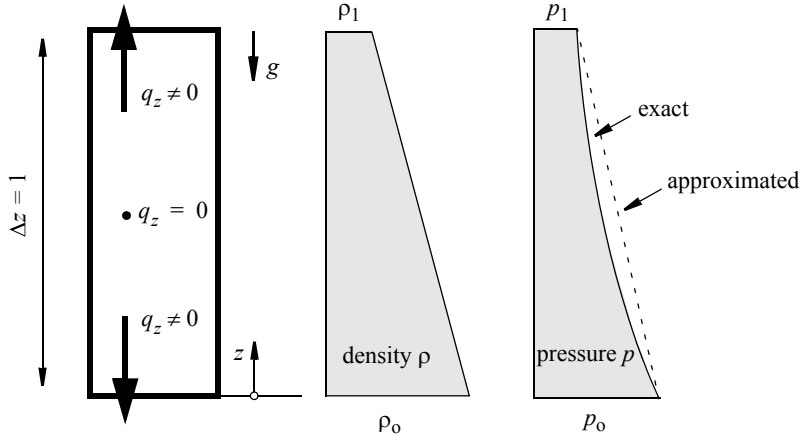

Figure 1.5 Hydrostatic conditions in a finite element of length $\Delta z = 1$ under a linear density gradient $\rho = \rho_o + (\rho_1 - \rho_o)z$; spurious vertical fluxes q_z caused by an inexact pressure approximation.

1.4.3.2 The artifact: Spurious nonconsistent velocities and possible solutions

Typically, in a discretization algorithm the mass fraction ω_k and the temperature T are linearly approximated in a finite element. This leads to a corresponding linear relationship for the density ρ as presented above. The pressure p is also approximated by a linear function in an element. This is (in the example of Fig. 1.5)[131]

$$p \to \tilde{p} = p_o + (p_1 - p_o)z \qquad z \in [0, 1] \qquad (1\text{-}91)$$

Inserting (1-91) in the Darcy equation (1-52) and using the exact nodal values p_o and $p_1 = p_o - g(\rho_o + \rho_1)/2$ from (1-90) we obtain for the z-component of the approximated velocity

$$q_z = -\frac{k_{zz}}{\mu} g(\rho_o - \rho_1)\left(\frac{1}{2} - z\right) \qquad z \in [0, 1] \qquad (1\text{-}92)$$

It clearly indicates that the approximated velocity only vanishes at the middle point ($z = 1/2$) while at the other points *artificial nonzero quantities* occur which take maximum values with opposite signs at the upper and lower point (*cf.* Fig. 1.5). Such *spurious nonconsistent velocities* can spoil the computational results in form of an overestimation of the mixing processes at strong density coupling. In the advective terms they may have only a minor effect as the averaging involved in the integration over elements and the assembly of adjacent elements tends to eliminate those nonconsistent velocities. However, if such spurious velocities are used to evaluate the dispersion tensor at the element level an artificial increase of hydrodynamic dispersion (mixing) will result[137].

The most common solution to the problem is reducing the spatial variation in the gravity term. The gravity term is averaged in the appropriate direction as proposed by Voss[231], Voss and Souza[233] and Leijnse[137]. In the above example we would have to use $\rho = (\rho_o + \rho_1)/2$ so as to find with the exact nodal values p_o and $p_1 = p_o - g(\rho_o + \rho_1)/2$:

$$v_z = -\frac{k_{zz}}{\mu}\left(\underbrace{p_o - g\frac{(\rho_o + \rho_1)}{2} - p_o}_{\partial_z p} + \underbrace{g\frac{(\rho_o + \rho_1)}{2}}_{\rho g} \right) = 0 \qquad (1\text{-}93)$$

which satisfies the equilibrium condition at all points.

Another possibility is to average the nonconsistent velocities at nodal points by local or global projection (smoothing) techniques as mentioned above. It smooths out the spurious velocities. Let us consider the following examples for a node m which is shared by two elements as shown in Fig. 1.6.

The smoothing procedure for the nonconsistent velocity (1-92) leads to a velocity at the node m of

$$q_z = \frac{k_{zz}}{\mu} g \frac{1}{2}\left[\frac{(\rho_o + \rho_2)}{2} - \rho_1\right] \qquad (1\text{-}94)$$

If we can assume that the density ρ_1 at the node m is an average of the upper and lower density values, i.e., $\rho_1 = (\rho_o + \rho_2)/2$, then the nodal velocity (1-94) becomes consistent $q_z = 0$. Obviously, this is true (or approximately true) for typical density profiles as

shown as case 1 in Fig. 1.6. However, if the density profile is strongly variable over a short distance (e.g., a narrow saltwater-freshwater interface with a high density contrast) the nonconsistent velocities do not vanish by averaging. This can be seen for case 2 in Fig. 1.6 at the node *m* where an upward spurious velocity remains on the order of

$$q_z = \frac{k_{zz}}{\mu} g \frac{1}{2}\left[\frac{(\rho_o - \rho_1)}{2}\right] \tag{1-95}$$

i.e., the consistency is no longer guaranteed at this node under those circumstances.

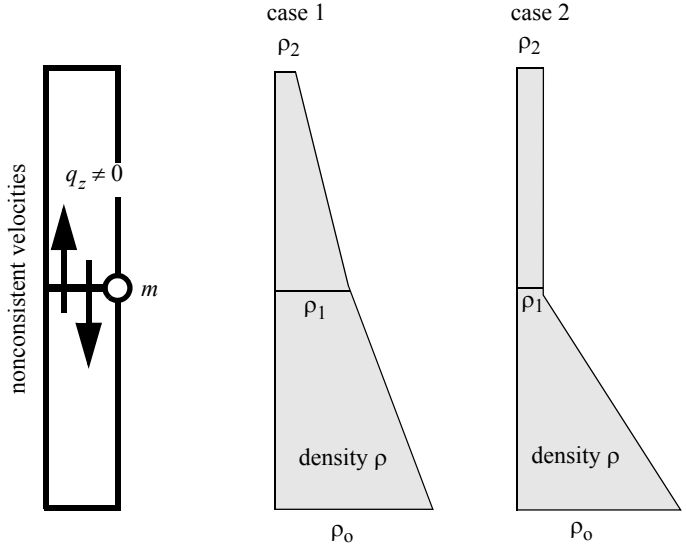

Figure 1.6 Continuous nodal velocity by averaging (smoothing) nonconsistent velocities for two cases of vertical density profiles.

We can summarize and conclude the following:
(i) Consistency is the requirement of a zero velocity under hydrostatic conditions for an arbitrary stable density gradient. A consistent velocity approximation satisfies the relationship (1-87) at the local evaluation points.
(ii) Averaging of the gravity term for each element yields a consistent velocity approximation; however, the accuracy in the spatial variation of the gravity term is reduced.
(iii) Smoothing of nonconsistent velocities derived at the Gaussian evaluation points averages out spurious velocities in most cases. However, if the density gradients become very large, spurious velocities at local points can remain. Thus, smoothing is a procedure to derive continuous nodal velocities which are often, but not always, *consistent* in the sense of statement (1-87).
(iv) There is a substantial need for a more general,

accurate and robust procedure for a consistent velocity approximation in density-dependent mass and heat transport problems. A promising algorithm was recently proposed by Frolkovic[72,73] and Knabner and Frolkovic[131] to approximate consistent velocities in two- and three-dimensional finite elements in a more general manner.

The *Frolkovic-Knabner algorithm* is described for affine and isoparametric families of finite elements, where the computations are realized on generalized (local) coordinates (ξ, η, ζ). The idea is the introduction of integral functions for the gravity term in a form such as

$$\left.\begin{aligned} H_\xi &= H_\xi(\xi,\eta,\zeta) = \int_0^\xi \rho(\theta,\eta,\zeta) g_\xi(\theta,\eta,\zeta) d\theta \\ H_\eta &= H_\eta(\xi,\eta,\zeta) = \int_0^\eta \rho(\xi,\theta,\zeta) g_\eta(\xi,\theta,\zeta) d\theta \\ H_\zeta &= H_\zeta(\xi,\eta,\zeta) = \int_0^\zeta \rho(\xi,\eta,\theta) g_\zeta(\xi,\eta,\theta) d\theta \end{aligned}\right\} \quad (1\text{-}96)$$

Since

$$\begin{Bmatrix} \partial_\xi H_\xi \\ \partial_\eta H_\eta \\ \partial_\zeta H_\zeta \end{Bmatrix} = \rho \boldsymbol{g}_{(\xi,\eta,\zeta)} \quad (1\text{-}97)$$

one can write the Darcy velocity (1-52) in an equivalent and consistent form

$$\boldsymbol{q} = -\frac{k_r \boldsymbol{k}}{\mu} \cdot \boldsymbol{J}^{-1} \cdot \begin{Bmatrix} \partial_\xi (p - H_\xi) \\ \partial_\eta (p - H_\eta) \\ \partial_\zeta (p - H_\zeta) \end{Bmatrix} \quad (1\text{-}98)$$

where $\boldsymbol{J}^{-1}$ is an inverse Jacobian. These new integral functions H_ξ, H_η, H_ζ allow us to obtain the same spatial variation for both, the pressure and the gravity term. The consistency of (1-98) in the definition of (1-87) can be proved. Assuming the gravity acts in the z-direction, i.e., $\rho(x, y, z) = \rho(x_o, y_o, z)$ we can write

$$\begin{aligned} H_\xi &= \int_0^\xi \rho(x_o, y_o, z(\theta,\eta,\zeta)) g_\xi d\theta \\ &= g_z \int_{z_0}^{z(\xi,\eta,\zeta)} \rho(x_o, y_o, \theta) d\theta \end{aligned} \quad (1\text{-}99)$$

where $(x_0, y_0, z_0) = (x(0,0,0), y(0,0,0), z(0,0,0))$ and similarly for H_η and H_ζ.

In the FEM the functions $p, H_\xi, H_\eta, H_\zeta$ are interpolated by their nodal basis functions:

$$\left.\begin{aligned} p &= \sum_m p_m N_m(\xi,\eta,\zeta) \\ H_\xi &= \sum_m H_{\xi m} N_m(\xi,\eta,\zeta) \\ H_\eta &= \sum_m H_{\eta m} N_m(\xi,\eta,\zeta) \\ H_\zeta &= \sum_m H_{\zeta m} N_m(\xi,\eta,\zeta) \end{aligned}\right\} \quad (1\text{-}100)$$

and we obtain the velocity (1-98) in the discretized for-

mulation

$$\boldsymbol{q} = -\frac{k_r \boldsymbol{k}}{\mu} \cdot \boldsymbol{J}^{-1} \cdot \sum_m \begin{Bmatrix} (p_m - H_{\xi m}) \partial_\xi N_m(\xi, \eta, \zeta) \\ (p_m - H_{\eta m}) \partial_\eta N_m(\xi, \eta, \zeta) \\ (p_m - H_{\zeta m}) \partial_\zeta N_m(\xi, \eta, \zeta) \end{Bmatrix} \quad (1\text{-}101)$$

which represents a fully consistent approximation of the Darcy fluxes $\boldsymbol{q}$. We solve (1-101) for given pressures p and the values of the H_ξ, H_η, H_ζ-functions at the nodes m. The nodal quantities $H_{\xi m}, H_{\eta m}, H_{\zeta m}$ are dependent on the finite element types and are listed in[47,131] for triangular and quadrilateral elements, and in[47] for pentahedral and hexahedral elements. In[73] Frolkovic proposes modifications in the consistent velocity algorithm for triangle and tetrahedra elements.

The computation of the consistent velocities (1-101) is performed element-wise in a standard manner, where the Jacobian $\boldsymbol{J}$ and the global derivatives $\nabla(.) = \boldsymbol{J}^{-1} \cdot \nabla_{(\xi, \eta, \zeta)}(.)$ are evaluated at Gauss points for each element. The element-by-element computation leads naturally to a consistent velocity field, which is in general discontinuous at nodes. To obtain continuous velocities a projection (smoothing) technique can be applied. Obviously, a smoothing procedure has no effect on the consistency of the velocity. This can be proven in an elemental patch test, where a node sharing a number of elements is considered. If the velocity contributions from the adjacent elements at this node are consistent, i.e., they are zero in the hydrostatic case, an average of zeros is always zero

1.4.4 Fully adaptive strategies

A successful use of numerical methods (FEM, FVM) requires significant expertise and cost. This is particularly true for the present coupled nonlinear problem class. The accuracy and reliability of the computations are of theoretical as well as of practical interest and represent a central problem in the numerical analysis[7]. Promising *adaptive strategies* for an automatic quantitative control of the discretization error(s) have been developed[159,160,237,247] and applied to convection problems[48,70,121]. Ideally, an adaptive method should be *reliable* in the sense that the discretization-error control should be guaranteed, and also *efficient* in the sense that the computational effort should remain within acceptable bounds. Although there are intense activities in numerical mathematics and computational mechanics, there are today only few applications of adaptive techniques for convection problems in practice. For this class of coupled problems, a quantitative error control is complicated, and analytical error estimates do not exist. Nevertheless, adaptive finite-element algorithms can be constructed on the basis of *a-posteriori* error estimates. They postulate that a finite-element solution can indicate which regions in a given domain need refinement or allow coarsening.

An adaptive procedure is divided into two phases: error estimation and mesh refinement/coarsening. Since the exact solution is not known, a method to approximate the error of a numerical solution is needed. Thus an appropriate measure, a norm, or seminorm, of the error has to be defined. Commonly, the error energy norm

$$\|\boldsymbol{e}\|^2 = \int_\Omega \boldsymbol{e}^T L(\boldsymbol{e}) d\Omega \quad (1\text{-}102)$$

is used[248], where L is a differential operator and $\boldsymbol{e}$ is a

local error measure. Denoting the exact and the finite element solution by $\boldsymbol{a}$ and $\tilde{\boldsymbol{a}}$, respectively, $\boldsymbol{e}$ is defined as

$$\boldsymbol{e} = \boldsymbol{a} - \tilde{\boldsymbol{a}} \tag{1-103}$$

For finding a physically appropriate energy expression for the coupled system (1-60) Diersch and Kolditz[48] used the internal Clausius-Duhem entropy production, which quantifies the irreversible thermodynamic process of the system and must be always positive according to the second law of thermodynamics. We can determine an equivalent energy functional, if the differential operator L in (1-102) is expressed by the dispersive flux vector $\boldsymbol{f}^d$ from (1-61), *viz*.,

$$L(\boldsymbol{e}) = \nabla \cdot (\boldsymbol{f}^d - \tilde{\boldsymbol{f}}^d) \tag{1-104}$$

Inserting (1-103) and (1-104) into (1-102), integrating by parts, and noting that the error vanishes on the boundary $\partial\Omega$ because $\boldsymbol{a}$ or $\boldsymbol{f}^d$ are prescribed there, the error estimator becomes

$$\|\boldsymbol{e}\|^2 = -\int_\Omega (\nabla(\boldsymbol{a} - \tilde{\boldsymbol{a}})) \cdot (\boldsymbol{f}^d - \tilde{\boldsymbol{f}}^d) d\Omega \tag{1-105}$$

where the dispersive fluxes $\boldsymbol{f}^d$ and $\tilde{\boldsymbol{f}}^d$ are expressed by the exact and finite element solutions according to the constitutive relations (1-51), which depend on the state variable $\boldsymbol{a}$ and $\tilde{\boldsymbol{a}}$, respectively. In fact, (1-105) forms a functional of the pressure p, mass ω_k and temperature T variables.

While (1-105) characterizes the error, a measure for the exact solution is also needed. Such a norm can be similarly derived as

$$\|\boldsymbol{a}\|^2 = \int_\Omega \boldsymbol{a}^T L(\boldsymbol{a}) d\Omega = -\int_\Omega (\nabla \boldsymbol{a}) \cdot \boldsymbol{f}^d d\Omega \tag{1-106}$$

We recognize from (1-105) and (1-106), that exact values of pressure, mass and temperature gradients (derivatives), which are generally unknown, are required. Therefore, these values must be approximated. A usual way is to compute these derivatives by a higher-order approximation. Fluxes (velocities) of higher-order accuracy can be easily obtained by using local and global projection (smoothing) techniques, such as already discussed above in the context of Darcy velocities. They can also be obtained by adequate flux recovery techniques, as proposed by Zienkiewicz and Zhu[249]. In doing so, we compute $\nabla \boldsymbol{a}$ by a projection, or recovery technique and $\nabla \tilde{\boldsymbol{a}}$ is then obtained by direct differentiation. The norms $\|\boldsymbol{e}\|$ and $\|\boldsymbol{a}\|$ are evaluated as the sum of their respective element contributions, *viz*.,

$$\|\boldsymbol{e}\|^2 = \sum_e \|\boldsymbol{e}\|_e^2 \qquad \|\boldsymbol{a}\|^2 = \sum_e \|\boldsymbol{a}\|_e^2 \tag{1-107}$$

From the above procedure we can introduce global and local error criteria as relative quantities, such as

$$\bar{\eta} = \frac{\|\boldsymbol{e}\|}{\|\boldsymbol{a}\|} \qquad \bar{\eta}_e = \frac{\|\boldsymbol{e}\|_e}{\|\boldsymbol{a}\|_e} \tag{1-108}$$

Two different optimality criteria are typically employed: (a) the equal distribution of the global error as proposed by Zienkiewicz and Zhu[248] and (b) the equal distribution of the specific error as introduced by Onate and Bugeda[165], in which both, global and local

error criteria are satisfied. The local error indicates elements which are above or below a permissible error measure. To meet the required accuracy according to the chosen optimality criterion, there are three strategies: (i) the *h*-adaptation, where the mesh is refined or coarsened locally, (ii) the *p*-adaptation, in which the order in the trial functions is increased or decreased, while the mesh is not changed, and (iii) the *hp*-adaptation representing a combination of the *h*- and *p*-adaptations.

For the present problem class the *h*-method is usually preferred. The *h*-refinement strategy is hierarchic. The finer mesh has to be created within the coarser mesh, and vice versa. Triangles in two dimensions and tetrahedra in three dimensions are particularly convenient and flexible in contrast to quadrilateral and hexahedral elements. For the latter, non-conformal meshes can overcome the topological difficulties in constructing transitional elements. They introduce hanging (or pinch) nodes and additional constraints, for which a specific treatment is required. However, hanging nodes do not necessarily satisfy balance statements. In contrast, conformal meshes formed by triangles or tetrahedra potentially possess better properties and provide a maximum of flexibility for a completely unstructured meshing. Most common is the *red-green* refinement/coarsening strategy for triangular and tetrahedral elements in two and three dimensions, respectively, as proposed by Bank *et al.*[10]. Higher mesh densities are achieved by subdividing elements into 4 (two-dimensional) or 8 (three-dimensional) so-called red elements, while the transition between refined and unrefined mesh regions is formed by so-called green elements to avoid hanging nodes. Green elements are transient and can be transformed into red elements after a further refinement. The adaptive mesh refinement can be combined with nodal movement and mesh smoothing techniques[79]. Löhner[141] reviews appropriate mesh refinement/coarsening strategies in two and three dimensions.

For transient problems the spatial adaptation has to be embedded in an appropriate time-stepping cycle. In using an automatic time-stepping control as outlined above, the overall solution becomes fully adaptive for the proposed predictor-corrector technique. Obvious, the computational effort can increase substantially and an efficient monitoring of the temporal and spatial refinement/coarsening is necessary. Ideally, the spatial adaptation is performed at each time level $n+1$. Alternatively, one can check the error criteria (1-108) only after a certain step number of advances in time and remesh if necessary. By also computing the variation of the error (1-108) with respect to time

$$\dot{\bar{\eta}} = \frac{\left|\bar{\eta}^{n+1} - \bar{\eta}^{n}\right|}{\Delta t_n} \tag{1-109}$$

remeshing can be avoided if the error is still decreasing at a reasonable rate[69].

The adaptive mesh refinement (AMR) technique in combination with adaptive time stepping monitors the actual spatial and temporal discretization requirements (‘watching physics’). We illustrate the use of such a fully adaptive solution procedure for the solution of Elder’s long-heater problem[59] in Fig. 1.7. Taking into account that the overall solution process was controlled by only two error criteria (one for each, time and space), the adaptive strategy is promising in reducing

'user-defined' (discretization) influences from the solu- tions for the buoyancy-driven convection problems.

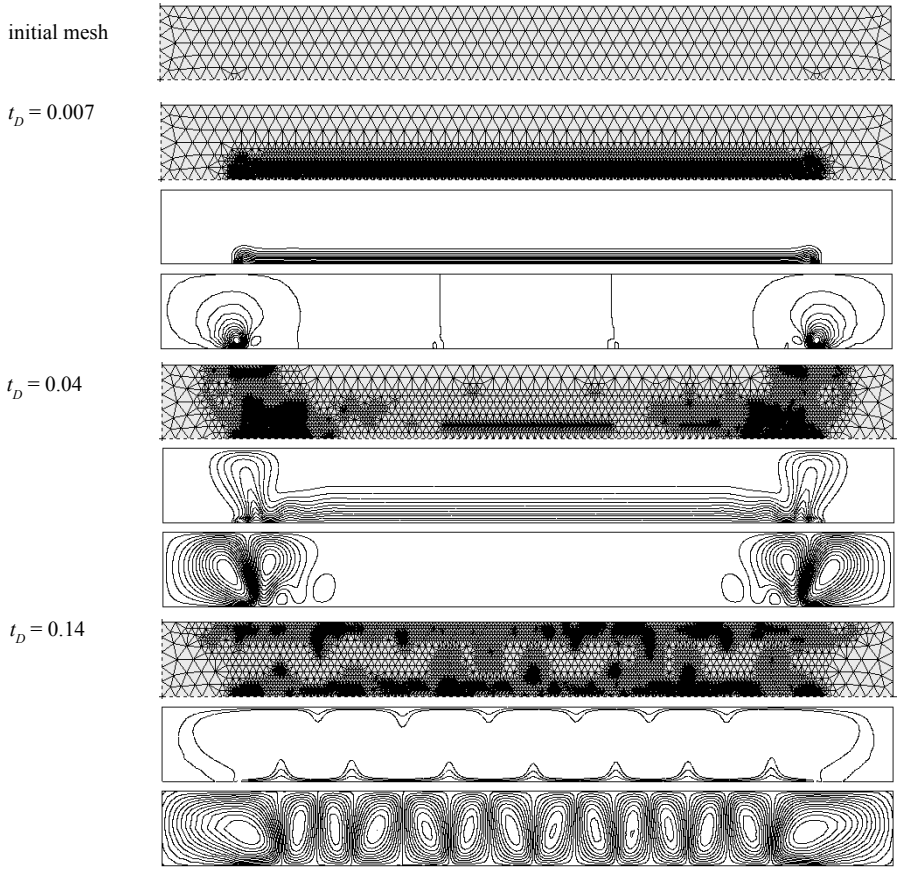

Figure 1.7 Elder's long-heater problem for Rayleigh number of 200 at different dimensionless times t_D simulated with FEFLOW by a fully adaptive strategy (Galerkin-FEM, Onate-Bugeda error criterion): meshes (range 18,000 - 23,000 triangles), isotherms and streamlines.

1.4.5 Remarks on numerical stability and accuracy

From the above discussion we can now state: If we are able to measure (and control) the discretization errors at an optimally small level, we can eliminate, or at least reduce the influences of numerical errors on the model simulations. Comparing our model results to experiments and observations, we could be sure that any differences are not caused by improper discretization. Indeed, it is an important goal in numerical mathematics to develop *reliable and robust* schemes.

An important point refers to stability and boundedness of a solution. Note that stability does not imply accuracy - although it is true that instability implies inaccuracy. Numerical solutions should lie within proper bounds. Physically, non-negative quantities (e.g., density, concentration) should always be positive. However, boundedness is difficult to guarantee. Unbounded solutions can occur on too coarse meshes or too large time steps in form of *wiggles*, i.e., overshooting and undershooting of the solution. Wiggles are usually a signal that the spatial or temporal discretization is too coarse and some refinements (at least locally) are required. Stability and convergence problems can result if the solutions contain too many wiggles. A positive aspect of wiggles is that in signalling improper discretization they present a *self-diagnosis property*[86]. A method with such a self-diagnostic property is often superior to schemes which give smooth, and totally wiggle-free, but inaccurate and overdamped solutions for any discretization.

It is well-known for the two-stage transient ODE approximation (1-68) and (1-70), e.g.[86,184,247], that the fully implicit scheme ($\theta = 1$) with a first-order accuracy in time is unconditionally stable and the semi-implicit Crank-Nicolson (or TR) scheme ($\theta = \frac{1}{2}$) with a second-order accuracy in time is stable, but unbounded and can produce oscillatory solutions unless

$$\Delta t_n \leq \frac{2}{\chi_{\max}^{n+1}} \tag{1-110}$$

where $\chi_{\max}^{n+1}$ is the largest eigenvalue associated with the matrix system (1-68) and (1-70). However, in using the maximum eigenvalue in (1-110), the timestep constraint is often overestimated and can be relaxed in practice[177]. In contrast, the explicit scheme ($\theta = 0$) with a first-order accuracy in time absolutely require (1-110) for stability reasons. It is a strong limit which is associated with the famous Courant-Friedrichs-Lewy (CFL) condition

$$Cr = \|\boldsymbol{v}\| \frac{\Delta t}{h} \leq 1 \tag{1-111}$$

derived for hyperbolic partial differential equations, where Cr is the Courant number and h corresponds to a characteristic element length.

If the advective (first-order derivative) part in the transport equations becomes dominant, wiggles in the solutions can occur and the spatial discretization with standard methods (e.g., Galerkin-FEM) is insufficient. Those wiggles are of nonphysical nature and signal that serious deficiencies in the mesh exist. They are caused by sharp gradients, which are insufficiently resolved by the mesh. To avoid oscillations the typical constraint is given by

$$Pe = \frac{\|\boldsymbol{v}\| h}{D} \leq 2 \tag{1-112}$$

derived for linear elements and (one-dimensional) linear transport equations, where Pe is the mesh Peclet number. The inequality (1-112) does not generally apply and is required only at locations with steep gradients, if any.

There are many ways to cope with the wiggle problem, broadly categorized by two basic 'philosophies', (i) those which improve the mesh design by enrichment or adaptation, and (ii) those which prefer (or resort to) methods capable of damping out the wiggles. A long history of research and development has lead to *stabilized* formulations that produce wiggle-free (smooth) solutions on virtually any mesh, *cf.*[86,184,247]. A common method is the streamline-upwind Petrov-Galerkin (SUPG) scheme, which introduces a balancing tensor diffusivity (BTD) term to stabilize the solution. It is equivalent to modifying the mechanical dispersion tensor (1-51) according to

$$\boldsymbol{D}_m^* = \beta_T \|\boldsymbol{q}\| \boldsymbol{I} + (\beta_L + \beta_L^{\text{num}} - \beta_T) \frac{\boldsymbol{q} \otimes \boldsymbol{q}}{\|\boldsymbol{q}\|} \tag{1-113}$$

with a numerical dispersivity

$$\beta_L^{\text{num}} = \kappa \frac{h}{2} \tag{1-114}$$

derived for linear elements, where the upwind parameter $\kappa \in (0, 1)$ appears as an additional free parameter. Note, $\kappa = 0$ corresponds to the Galerkin-FEM and $\kappa = 1$ corresponds to the upwind scheme. The 'tricky' Petrov-Galerkin least square method (PGLS) with appropriate operator splitting[46] leads to symmetric matrix systems and possesses a built-in streamline-like upwind characteristic without any free parameter that produces a timestep-dependent damping equivalent to a numerical dispersivity of

$$\beta_L^{\text{num}} = \frac{\Delta t_n}{\varepsilon s} \|\boldsymbol{q}\| \tag{1-115}$$

A similar 'upwind-in-time' technique is used in the Taylor-Galerkin FEM[54,126,247]. If using schemes of second-order accuracy in time (e.g., Crank-Nicolson scheme), the temporal upwind term is also of second order and the Taylor-Galerkin FEM becomes more precise. Shock capturing is a nonlinear upwind method[42] and depends itself on the numerical solution. It attempts to damp out the wiggles only in the vicinity of sharp fronts and does not introduce numerical dispersion in regions where the solution is already sufficiently smooth. This principle (damping only near steep gradients) is widely followed in modern upwind strategies, such as the flux-corrected-transport (FCT) scheme, the essentially-non-oscillatory (ENO) method and the total-variation-diminishing (TVD) method[63,66,67,141], which are usually explicit strategies and naturally suffer from the strong CFL condition (1-111)[1,164]. FCT attempts to keep a front sharp on a fixed mesh, where an anti-diffusion step is employed to overcome the effects of excessive smearing. This idea is closely related to the idea of TVD and ENO. These methods also employ flux-correction to limit the introduction of oscillations.

The method of characteristics/trajectories (MOC), e.g.[66], represents a traditional explicit and decoupled strategy, which is also CFL-affected ('forward-looking'

characteristics). Modified, or backward methods of characteristics (MMOC or BMOC) exist. They are implicit by using a 'single step reverse' algorithm ('backward-looking' characteristics) as described by Neuman[152]. MMOC or BMOC represent Eulerian-Lagrangian methods with operator-splitting usually applied to the decoupled matrix systems, whereby the advective part of the transport equations is treated by a backward MOC, while the dispersive part is handled via standard finite elements (or finite volumes). A comparison of second-order MOC approaches to most of the other techniques was presented by Al-Lawatia *et al*.[6] for the one-dimensional advection-diffusion equation. The MOC strategies can be very efficient and accurate and have even been successfully applied to density-dependent problems[76,129,191,209]; however, they are difficult to implement in two and three dimensions and are often limited to special cases.

The selected temporal and spatial (upwind) discretization strategies affect the accuracy of the solution. We consider the truncation errors for linear elements (volumes), which can be expressed in terms of numerical (nonphysical) diffusivity/dispersion as

$$\left.\begin{aligned} D^{\text{num}} &= D^{\text{num}}_{\text{spatial}} + D^{\text{num}}_{\text{temporal}} \\ D^{\text{num}}_{\text{spatial}} &= \kappa \frac{\|\boldsymbol{v}\| h}{2} + O(h^2) \\ D^{\text{num}}_{\text{temporal}} &= (\theta - \tfrac{1}{2}) \Delta t_n \|\boldsymbol{v}\|^2 + O(\Delta t_n{}^2) \end{aligned}\right\} \qquad (1\text{-}116)$$

As (1-116) shows, first-order upwind schemes and a first-order implicit temporal approximation introduce a maximum numerical dispersion. Small element (volume) sizes h and timesteps Δt_n are required to reduce D^{num}. (Note, the temporal numerical dispersion in explicit schemes is small, because the timestep is usually small due to the CFL condition (1-111)). The original (physical) diffusivity D is artificially raised by D^{num} consequently a convection process is simulated with changed parameters, as quantified by an effective Rayleigh number

$$Ra^{\text{eff}} = \frac{Ra}{1 + \frac{\kappa}{2} Pe + (\theta - \frac{1}{2}) CrPe} \qquad (1\text{-}117)$$

From (1-117) the danger from upwind schemes and/or fully implicit (or explicit) becomes obvious: the solution can evolve to a point rather far from the real physics of a flow problem, if first-order accurate upwinding on coarse meshes, and/or fully implicit time marching schemes with large step sizes are used. We thus like to conclude in agreement with J. Ferziger (noted in[86]): '*The greatest disaster one can encounter in computation is not instability or lack of convergence, but results that are good enough to be believable but bad enough to cause trouble*'.

1.5 Benchmarking

A numerical model should work accurately if both the discretization and the convergence errors are sufficiently small[65]. Unfortunately, in many practical applications conceptual model errors additionally have to be taken into account. The separation of the modeling errors from the 'true' numerical errors appears as an important (and often difficult) task, because various errors may even cancel each other out. To quantify the order of accuracy, models and algorithms have to be tested under different aspects. Such tests are categorized

as follows[9]:

- *Verification:* A comparison to a model problem, which is sufficiently elementary, so that the exact (e.g. analytical) solution is known.
- *Benchmark:* A comparison to a model problem, which possesses the intrinsic physical and mathematical character (e.g., nonlinearity) of the basic model, but has a simplified geometry so that comparable numerical solutions of accepted quality are available.
- *Validation:* A comparison to a genuine problem, for which quality experimental data are available.

The traditional verification procedure by use of analytical solutions is not generally applicable due to the nonlinear nature of variable-density problems. In general, there are no exact solutions for this problem class, except a rather limited number of analytical and semi-analytical solutions for specific cases[28,55,99,198,201,211]. As a consequence, modelers must rely on benchmark tests, which thus obtain a key role in proving density-dependent models and simulation codes. Benchmarking covers asymptotic and mesh (grid) convergence tests, as well as comparative studies between different numerical solutions (mainly obtained with different simulators). What are the characteristics of a valuable benchmark for variable density problems? It should have a real, practically and/or physically relevant background. It should be mathematically correct, definite, and well-posed. Benchmark solutions should be predictable (nonrandom), both in the physical and mathematical sense. Ideally, the benchmark should have a physical model equivalent, for which qualified laboratory data are available. Those measurements can form reference solutions for a comparative analysis. In this context, numerical solutions are required to understand the physical process and its causal dependencies. This is what we would define as a *physical benchmark* that provides a physically reliable basis for further comparisons. Those benchmarks were often missed in the past. Only recently, there are increasing efforts and remarkable progress in qualified experimental investigations of density-dependent systems which challenge numerical simulations and code competitors (e.g., Schincariol and Schwartz[194], Oswald[167], Thorenz *et al*.[219], Simmons *et al*.[208]).

Physical benchmarks are frequently based on Hele-Shaw cell experiments, e.g.,[58,59,208,242,243]. A Hele-Shaw cell provides an analogue of flow in a porous medium to some extent, in that the equations that characterize flow in a Hele-Shaw cell (to a good approximation) are the same as the equations that characterize flow in a porous medium. However, the equations that characterize transport of salinity and heat in a Hele-Shaw cell are not quite the same as those that characterize transport of salinity and heat in a porous medium. For instance, dispersion and instabilities associated with three-dimensional disturbances are different in a Hele-Shaw cell[134].

1.5.1 Hydrostatic test

This type of benchmark is quite simple, but very instructive. It is a test of the velocity consistency (1-87) under hydrostatic and sharp density transition conditions as originally proposed by Voss and Souza[233]. Recently, Taylor *et al*.[216] benchmarked a number of variable-density model codes against this test problem

and concluded that none of the codes could match the hydrostatic condition. Consider a rectangular closed domain as shown in Fig. 1.8. Initially, a stable saltwater layer with a salinity of $\omega = \omega_s$ exists below freshwater with $\omega = \omega_0 = 0$, separated by a sharp horizontal interface in the middle of the domain. The domain is impervious with respect to both the flow, and the mass. The fluid density contrast α is defined by

$$\alpha = \frac{\rho_s - \rho_0}{\rho_0 \omega_s} \quad \text{with} \quad \rho_s = \rho(\omega_s), \quad \rho_0 = \rho(\omega_0) \qquad (1\text{-}118)$$

The α-parameter is to be varied in a numerical study whereby the density coupling increases with α. We illustrate the results for an α-value of $0.03/\omega_s$.

The problem is hydrostatic at all times and the fluid motion within the box should be zero, or in the numerical sense, negligibly small. Due to the molecular diffusion D_d the saltwater mixes (Fickian law (1-7) is assumed) and the initially sharp saltwater interface (narrow transition zone) spreads in time. This process must be independent of the density. Accordingly, we have to compare the results of the saltwater interface spreading for the case without density coupling, against the cases where density effects are included. As a reference solution we compute the problem for $\alpha \equiv 0$, based on a fine temporal and spatial discretization. We have simulated the density-dependent problem for quadrilateral and triangular meshes both in two and three dimensions by using the different velocity approximations (Frolkovic-Knabner method, local projection/smoothing technique), as discussed above. The findings are similar to those depicted in Fig. 1.9 for the two-dimensional quadrilateral elements.

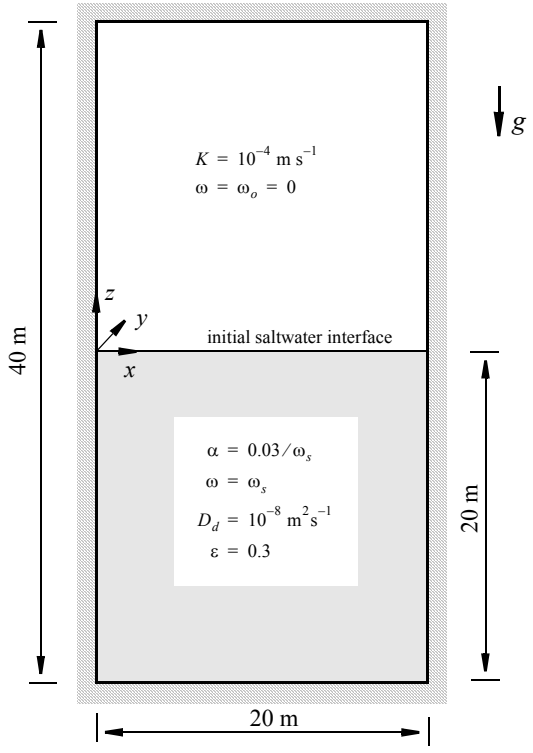

Figure 1.8 Cross-sectional view of the initially stratified saltwater below freshwater problem in a closed porous box.

The projection method causes an artificially increased spreading of the salinity much like numerical dispersion. This is caused by spurious local velocities at the interface nodes, that locally violate the consistency requirement. The smearing in the density profile increases, if dispersion ($\beta_L = 5\text{m}, \beta_T = 0.5\text{m}$) is additionally taken into account. In contrast, the consistent velocity approximation by the Frolkovic-Knabner

method avoids any spuriousness in the velocity field. These results agree very well with the reference solution, independent of dispersion effects.

This benchmark reveals the weakness of the projection methods, which normally work satisfactorily. However, these techniques cannot guarantee the local consistency in the velocity field for problems involving sharp transition zones in the density contrast and, therefore, advanced evaluation techniques such as the Frolkovic-Knabner method are to be preferred. This benchmark can be extended by imposing a horizontal uniform flow at hydrostatic conditions. In such a test a density profile should not be smeared if transverse dispersivity and diffusion are set to zero[216,232].

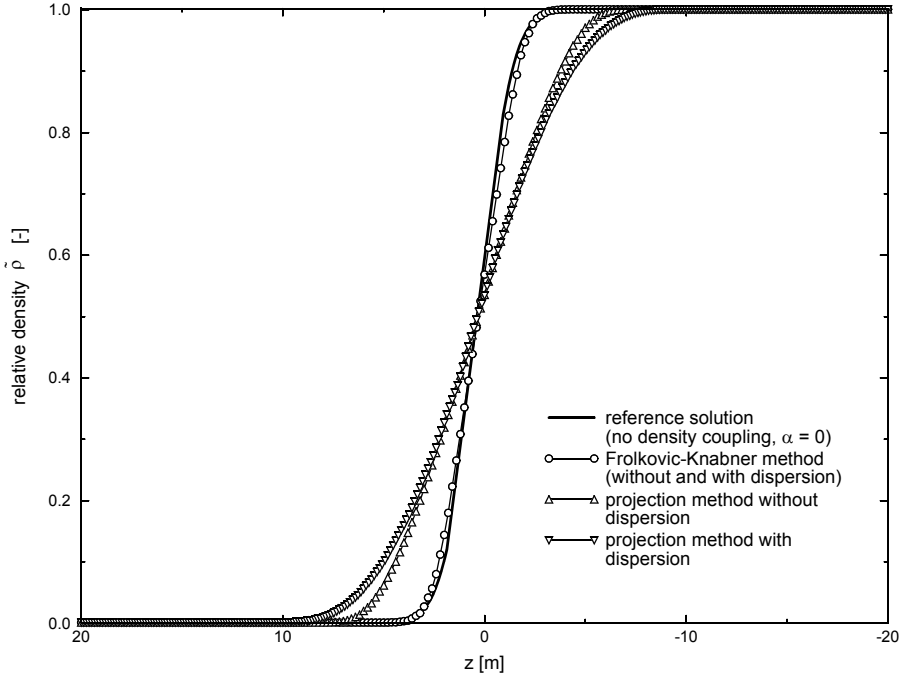

Figure 1.9 Computed density profiles $\tilde{\rho}(x,z) = (\rho - \rho_0)/\rho_0$, x = 10m, 20m $\leq z \leq$ -20m at time $t = 10^3$ days for different solutions using quadrilateral elements: Reference solution is obtained without density effects for a fine vertical mesh; the other solutions are simulated on a uniform 32x64 mesh of quadrilateral elements.

1.5.2 Henry problem

The Henry problem describes the advance of a saltwater front in a confined aquifer which was initially saturated with uncontaminated freshwater. Henry[99] developed a semi-analytical solution technique for this problem. Based on the OB approximation he derived analytical expressions for the stream function and the salt concentration in the form of Fourier series. The resulting algebraic equations for determining the coefficients of the Fourier series must be solved by numerical techniques. Using quite different approximation methods, a number of authors obtained similar results (e.g., Pinder and Cooper[179], Segol *et al.*[203], Desai and Contractor[37], Frind[71], Voss and Souza[233], Galeati *et al.*[76], Oldenburg and Pruess[161], Croucher and O'Sullivan[33], Bués and Oltean[22]). The 'mystery' of Henry's solution is that to date no numerical model has been able to reproduce closely his semi-analytical results[201] (*cf.* dashed line in Fig. 1.10). Nevertheless, as there exists no other non-numerical technique for this kind of nonlinear problem, Henry's solution has become one of the standard tests of variable-density groundwater models. The idealized aquifer for the simulation of Henry's problem is shown in Fig. 1.10. The boundary conditions for flow consist of impermeable borders along the top and the bottom. Hydrostatic pressure is assumed along the vertical boundary of the sea side. The aquifer is charged with freshwater at a constant flux from the left side. At the inland side, the concentration is zero, which corresponds to a freshwater condition. At the coastal side the normalized concentration of brine is imposed. Instead of velocity-dependent dispersion a correspondingly large diffusivity was used by Henry[99] in order to allow a semi-analytical solution. The simulation parameters for the Henry problem are given in Tab. 1.1.

Table 1.1 Simulation parameters for the Henry problem

Symbol	Quantity	Value	Unit
D_d	coefficient of molecular diffusion	$6.6 \cdot 10^{-6}$	$m^2 s^{-1}$
β_L	longitudinal dispersivity	0	m
β_T	transverse dispersivity	0	m
g	gravitational acceleration	9.81	ms^{-2}
k	permeability of porous medium	$1.019368 \cdot 10^{-9}$	m^2
q	specific discharge on the left side	$6.6 \cdot 10^{-2}$	$kgm^{-1}s^{-1}$
Ra_s	solutal Rayleigh number	250	-
ε	porosity	0.35	-
μ	dynamic viscosity	10^{-3}	$kgm^{-1}s^{-1}$
ρ_0, ρ_s	density of water and solute	$(1.0, 1.026) \cdot 10^3$	kgm^{-3}

Figure 1.10 summarizes some former findings for the Henry problem obtained by several authors, who used quite different computation methods. Comparing these results, it has to be kept in mind that slightly different parameter values were chosen by the authors.

There have been some discrepancies in the use of the diffusion coefficients. Note that the effective diffusivity is the product of the molecular diffusion coefficient and the porosity. Further solutions and comparisons for the Henry problem have been presented by Kolditz *et al.*[126]. Recently, Kaiser[121] and Thorenz[218] revisited this benchmark using an error-based AMR technique to improve the numerical accuracy. They confirmed the prior findings (Fig. 1.11). The mesh adaptation algorithm refines meshes automatically in areas with large salinity gradients.

The Henry problem is often used as a benchmark for variable-density flow and transport although it has some deficiencies. An unrealistically large amount of diffusion is introduced which results in a widely dispersed transition zone. It makes the solution smooth and rather nonproblematic. The Henry problem is not appropriate for verifying purely density-driven flow situations. Additional benchmark tests are necessary to examine the numerical models for free convection problems (such as the Elder problem) and situations with narrow transition zones (such as the salt dome problem) which will be considered next. In a section further below we will also discuss a new variant of Henry's problem for variably saturated porous media.

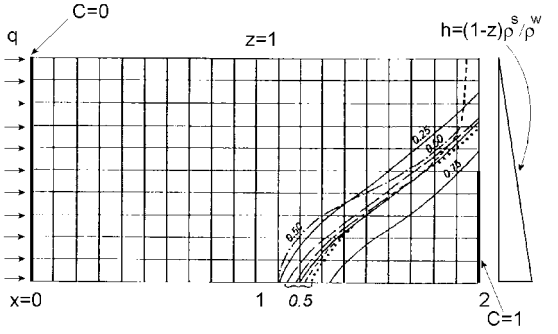

Figure 1.10 Definition of the Henry problem and prior results by Henry[99] - dashed line, Pinder and Cooper[179] - dashed-dotted line, Segol *et al.*[203] - dotted line, Desai and Contractor[37] - long-dashed line, Frind[71] - short-long-dashed line, and Voss and Souza[233] - solid line; positions of the 25, 50, and 75 percent isochlors of the steady-state solution (modified from Voss and Souza[233]).

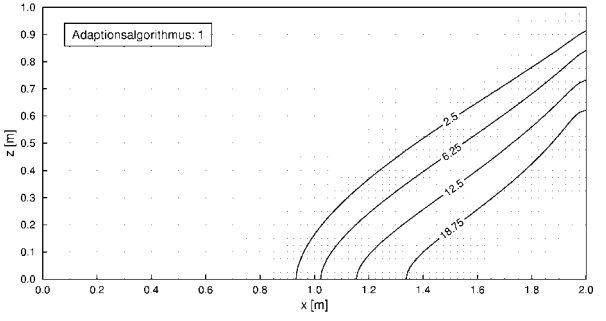

Figure 1.11 Positions of the 10, 25, 50, and 75 percent isochlors of the steady-state solution for the Henry problem - mesh adaptive solution (Kaiser[121]).

1.5.3 Elder problem

1.5.3.1 Elder's short-heater problem and its saline analogue

The Elder problem serves as an example of free convection phenomena, where the bulk fluid flow is driven purely by fluid density differences. Elder[58,59] presented experimental and numerical studies concerning the thermal convection produced, by heating a part of the base of a porous layer. The original experiment, which was performed in a Hele-Shaw cell, was called the 'short-heater problem'. Elder conducted these studies mainly to verify the finite difference model he used for the two-dimensional numerical analysis of thermal-driven convection. Furthermore, he suggested criteria for preventing numerical instabilities. Since then, Elder's short-heater problem become a very popular and often stressed benchmark problem in the water resources literature. It is rich in physical and numerical implications, and its cellular flow characteristic is fascinating. The Elder problem has been modified, extended, and remains a topic of, sometimes controversial, discussion.

Diersch[38] and later Voss and Souza[233] transformed the thermal Elder problem into a solute-analogous convection problem, where heavy saltwater is placed on top. Voss and Souza 'blew up' the geometry so that Elder's problem can now be deemed a large-scale, density-driven saltwater intrusion process in a cross-sectional aquifer schematization. The original Elder problem of the thermal convection in a Hele-Shaw cell and the solute-analogous convection problem are mathematically equivalent (via the Rayleigh number). However, we note that the problem in this formulation is completely imaginary and hypothetical. Dispersion, which can play a very important role in a real aquifer, is not included. Usually, this saline analogue is also termed the Elder problem. The simulation parameters and boundary conditions for the saline Elder problem are summarized in Tab. 1.2 and Fig. 1.12.

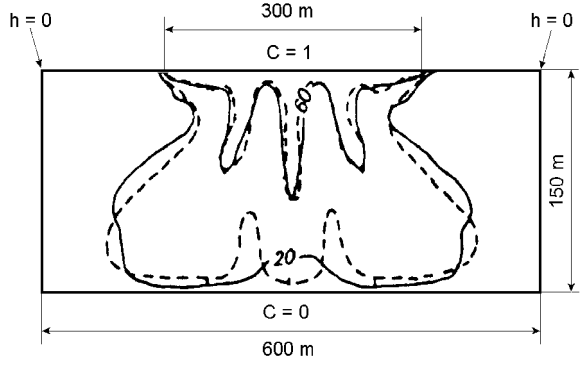

Figure 1.12 Definition of the Elder problem and prior results by Elder[59] - solid line and Voss and Souza[233] - dashed line; positions of the 20 and 60 percent isochlors at 10 years simulation time (adapted from Voss and Souza[233]).

Table 1.2 Simulation parameters for the saline Elder problem

Symbol	Quantity	Value	Unit
L	base length	600	m
d	cell (aquifer) height	150	m
e	extent of intrusion	300	m

Table 1.2 Simulation parameters for the saline Elder problem (continued)

Symbol	Quantity	Value	Unit
μ	dynamic viscosity	10^{-3}	$kgm^{-1}s^{-1}$
g	gravitational acceleration	9.81	ms^{-2}
I	symmetric intrusion ratio	0.5	-
k	permeability of porous medium	$4.845 \cdot 10^{-13}$	m^2
K	hydraulic conductivity	$4.753 \cdot 10^{-6}$	ms^{-1}
Ra_s	solutal Rayleigh number	400	-
α	solutal expansion coefficient	0.2	-
D_d	coefficient of molecular diffusion	$3.565 \cdot 10^{-6}$	m^2s^{-1}
ε	porosity	0.1	-
β_L	longitudinal dispersivity	0	m
β_T	transverse dispersivity	0	m
ρ_0, ρ_s	density of water and solute	$(1.0, 1.2) \cdot 10^3$	kgm^{-3}

1.5.3.2 Previous and recent studies, and some surprises

Neither exact solutions nor qualified measurements (!) exist for the Elder problem. Consequently, the (currently) only way to compare is with numerical solutions. Figure 1.12 depicts Elder's finite-difference solutions[59] and Voss and Souza's Galerkin-FEM results[233] for a simulation time of ten years. Using a similar spatial discretization in a Galerkin-FEM, we can reproduce these salinity patterns very well (Fig. 1.13a). However, strong discretization effects were observed by using different meshes. Kolditz *et al.*[126] conducted a mesh convergence study, where the meshes were consecutively refined until a supposed mesh convergence was achieved. Figure 1.13b exhibits their solutions obtained for the highest refinement. They tested both the OB and the extended OB approximation. The most important outcome of this study was, that for fine meshes there is a central upwelling flow rather than the central downwelling flow found for coarse meshes, as shown in Fig. 1.13 at the time of 20 years. This high-resolution results compare very well with those already given by Oldenburg and Pruess[161]. Kolditz *et al.*[126] concluded that at least 4400 bilinear finite elements (4539 nodes) are required on the whole domain, to model an upwelling flow characteristic (deemed the correct solution). These observations gave rise to various numerical studies by other authors. Ackerer *et al.*[1] used a mixed hybrid FEM with a TVD stabilized scheme. They confirmed the upwelling solution. In their study, upwelling flow appeared already at coarser meshes. A similar mixed hybrid FEM was used by Mazzia *et al.*[144] who found a central downwelling flow on coarse meshes. A detailed study was recently presented by Oltean and Bués[164] who used a mixed

hybrid and discontinuous FEM stabilized by TVD. They found a close similarity to the prior results by Kolditz *et al.*[126] with the central upwelling flow field. Conservative and non-conservative approaches were compared. It was shown that the maximum differences between them occur at a time of about 6 years (we will see later that this time level is obviously the most critical for the process evolution).

Recently, Frolkovic and De Schepper[74] presented new results for the Elder problem, based on a strict mesh convergence study using FVM, where the mesh size is consecutively refined. They achieved mesh convergence by a systematical mesh refinement for a mesh level l. For a uniform discretization by quadrilateral square elements the number of elements (NE) and the number of nodes (NN) for the whole and the half domain are given by

$$\begin{aligned} NE &= 2 \cdot NE_2 & NE_2 &= 2 \cdot 4^l \\ NN &= 2 \cdot NN_2 - (4^{l/2} + 1) & NN_2 &= 2 \cdot (4^{l/2} + 1)^2 - (4^{l/2} + 1) \end{aligned} \qquad (1\text{-}119)$$

Frolkovic and De Schepper[74] performed their simulations on the symmetric half domain in a range of the mesh levels l up to 8. (Note, for $l = 8$ they no longer used a uniform refinement. Instead they used an AMR technique for local refinement with mixed triangular and quadrilateral elements, based on an a-posteriori error estimator). Their results are highly interesting, and there are surprises: When l is small, the flow downwells, and at increasing l an upwelling flow appears as expected. But if l is increased above $l > 6$, a central downwelling characteristic develops again.

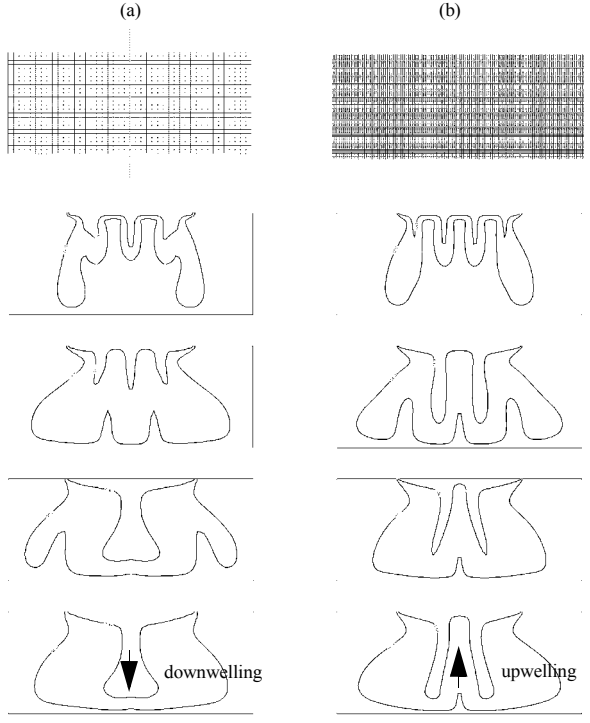

Figure 1.13 Effect of spatial discretization on the computed salinity evolution at 4, 10, 15, and 20 years simulation time; positions of the 20 and 60 percent isochlors: (a) coarse mesh (1170 nodes, 1100 quadrilateral elements), comparable with the discretization used by Elder[59] and Voss and Souza[233], (b) fine mesh (10108 nodes, 9900 quadrilateral elements).

This has prompted our own simulations which we have performed with the FEFLOW simulator[44], tackling mesh levels l up to 9 (this is a rather fine mesh with NN_2 equal to 525,825 for the half domain solved). In using a half domain model, an additional symmetry

condition is imposed. Our results are depicted in Fig. 1.14 and confirm Frolkovic and De Schepper's observations. Up to a mesh with resolution of $l = 5$, a central upwelling is seen which agrees with the previous findings reported by Oldenburg and Pruess[161], Kolditz *et al.*[126], Ackerer *et al.*[1], and Oltean and Bués[164]. From $l \geq 6$ onward the flow turns back to a downwelling pattern. This is shown in Fig. 1.14 for levels 6 and 9; levels 7 and 8 (not shown) are comparable with level 6. As revealed in the streamline pattern of Fig. 1.14, the flow behavior in the upper central location at a time between 2.5 and 5 years appears to be most critical for the further evolution of the convection process. Various eddies begin to mutually interact, to fuse and to disappear, and the local velocities control which rotation of the merged vortices finally prevails. At that location and time, the solution evolves either to an upwelling or to a downwelling flow regime. We can now summarize in Tab. 1.3 all of the findings relating to the form of the flow direction in the central section, qualified by the degree of mesh refinement.

Table 1.3 Flow direction in the central section with respect to the mesh discretization (modified from Oltean and Bués[164])

Discretization Number of unknowns[a]	Very coarse < 800	Coarse 1000-2000	Fine 3500-5000	Very fine 6000-10,000	Extremely fine 15,000 - 1,000,000
Diersch[38]	↓	-	-	-	-
Voss and Souza[233]	-	↓	-	-	-
Oldenburg and Pruess[161]	-	↓	↑	↑	-
Kolditz *et al.*[126]	-	↓	↑	↑	-
Ackerer *et al.*[1]	↑	↑	↑	↑	-
Mazzia *et al.*[144]	-	↓			
Oltean and Bués[164]	↑↓	↑↓	↑	↑	-
Frolkovic and De Schepper [74,b]	-	↓ ($l = 4$)	↑ ($l = 5$)	-	↑ ($l = 6$) ↓ ($l = 7$)

Table 1.3 Flow direction in the central section with respect to the mesh discretization (modified from Oltean and Bués[164]) (continued)

Discretization Number of unknowns[a]	Very coarse < 800	Coarse 1000-2000	Fine 3500-5000	Very fine 6000-10,000	Extremely fine 15,000 - 1,000,000
present[c]	-	↓ ($l = 4$)	↑ ($l = 5$)	-	↓ ($l = 6,7,8,9$)

a. related to the whole domain
b. unperturbed solutions, uniform mesh
c. no upwind, AB/TR time stepping, uniform quadrilaterals, unperturbed solutions

Diersch[47] has made comparisons between the projection and the Frolkovic-Knabner method for evaluating the velocity fields using mesh levels l in the range from 4 to 9. There were no remarkable differences and the resulting flow characteristics were always the same. He found that the projection method is accurate for the Elder problem.

We evaluated Frolkovic and De Schepper's results in Tab. 1.3 only for their unperturbed solutions obtained on uniform meshes up to $l = 7$. It is to be expected that uniform and aligned meshes with square elements are 'free' of perturbations, except 'noise' of numerical round-off and discretization errors. Furthermore, Frolkovic and De Schepper[74] also perturbed the problem by slightly modifying initial conditions for one of the vertices of the square element at the upper right corner of the half domain, i.e., setting $\omega = 0.01$. For smaller times ($t < 4$ yr) there were no remarkable changes in the solutions, but at later times the solution evolves in different directions. They observed three directional behaviors which convert to three different stationary solutions in form of a downwelling, an upwelling, and a modified downwelling pattern. All three solutions could be reproduced for various mesh levels. They concluded that non-unique stationary solutions exist for the Elder problem. It is suggested that unaligned (unstructured) meshes can cause a perturbation which, eventually, may determine the character of the numerical solution.

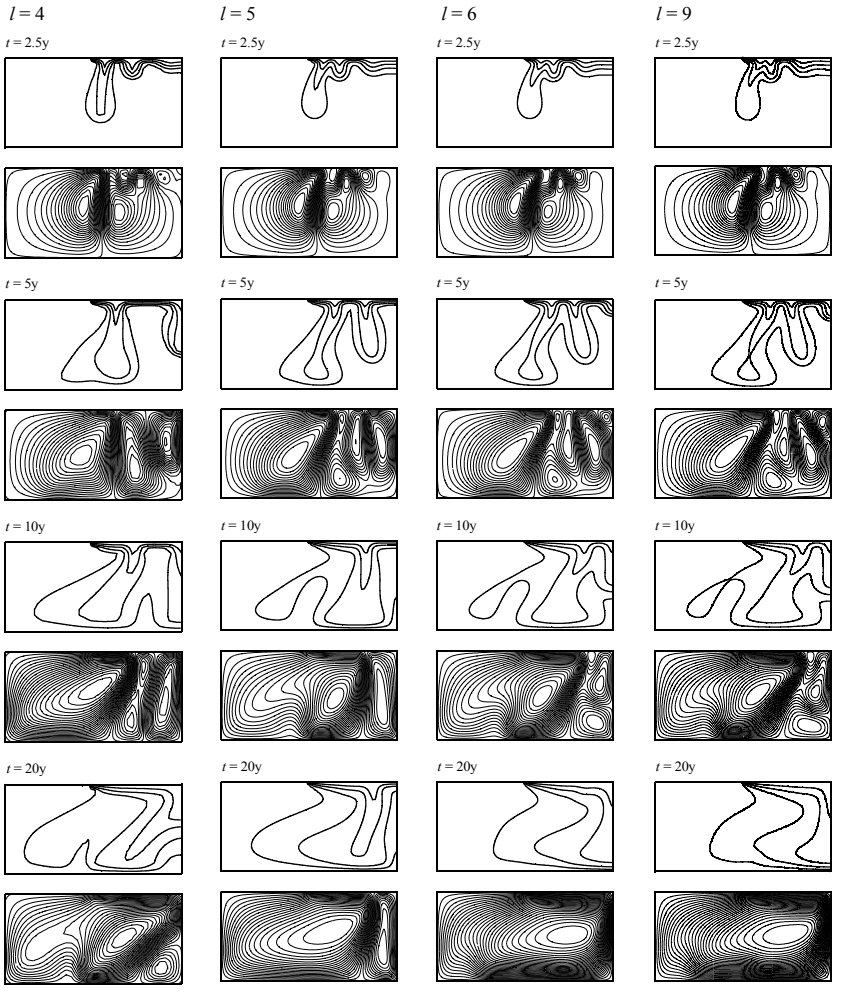

Figure 1.14 Computed salinities (0.2, 0.4, 0.6 and 0.8 isolines) and streamline patterns for four times *t* (2.5, 5, 10, 20 yrs) and for four mesh levels *l* (4,5,6,9): FEFLOW simulations using a Galerkin-FEM on quadrilateral uniform meshes of the half domain without perturbations and an automatic AB/TR predictor-corrector time stepping with the Frolkovic-Knabner algorithm to compute consistent velocity fields.

1.5.3.3 Thermohaline Elder problem

The two-dimensional saline Elder problem expands to a thermohaline convection process if the salinity field is augmented by a thermal distribution as defined in Fig. 1.15. While the homogeneous aquifer is permanently heated from below, the salinity gradient acts from above. As stated above, such a formulation of the thermohaline Elder problem can be considered as a mixed DDC regime where a finger regime dominates at the beginning (cool salinity sinks down) and a more diffusive regime occurs (downsunk salinity is heated from below) later.

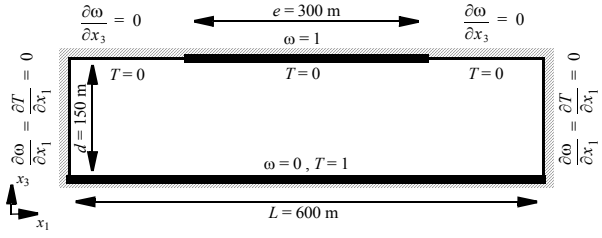

Figure 1.15 Definition of the two-dimensional thermohaline Elder problem[49].

Diersch and Kolditz[49] studied the thermohaline Elder problem for different Turner numbers $B = \infty, 5, 4, 3, 2$ at a Lewis number Le of unity. While the results for $B = 5$ are still rather similar to the pure (asymptotic) saline convection, beginning with $B = 4$ the influence of the superimposed thermal convection on the salinity distribution becomes apparent (Fig. 1.16). Now the fingers are sheared as a result of the opposing forces due to heat and salinity effects and the central upwelling flow changes to a downwelling in the late time scale. There are no monotonic changes in the salinity pattern. Surprisingly, salinity distributions reveal asymmetric characteristics at later times when the influence of thermal convection becomes stronger at $B \leq 2$. There no apparent physical reason for a broken symmetry and mesh effects are likely responsible for such an asymmetric evolution[49]. Note, the Rayleigh number is in a range (> 400) where solutions become sensitive to (numerical) perturbations. Clearly, the reasons of instabilities for this type of problem has to be studied in more detail.

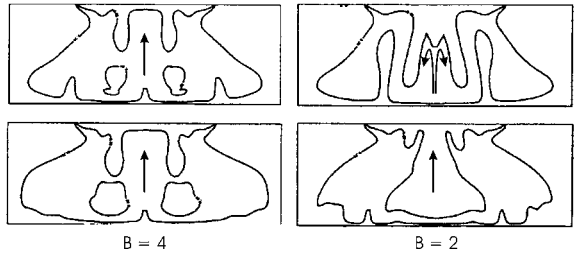

Figure 1.16 Onset of thermohaline effects: computed salinity distributions of 0.2 and 0.6 normalized isochlors at 10 (top) and 20 years (bottom) for different Turner numbers of $B = 4$ (left) and $B = 2$ (right).

Recently, Kaiser[121] and Thorenz[218] revisited the thermohaline Elder problem using AMR techniques. They used slightly different thermal boundary conditions. The constant temperature condition was imposed not along the entire cell bottom but only on a 300 m section at the bottom centre (i.e. as the constant salinity condition on the cell top). The simulation results corresponding to a Turner number of $B = 2$ are depicted in Fig. 1.17. The vertical mesh Peclet number for the smallest elements is $Pe = 2.43$ which is comparable to the fine mesh results by Diersch and Kolditz[49]. The

changes in the thermal boundary conditions result in completely different flow pattern. Now for $B = 2$ there is again a central upwelling flow similar to the original saline Elder problem. The AMR algorithm is embedded as a method in the object-oriented finite-element simulator ROCKFLOW[127] making AMR techniques available to several kinds of multi-field problems such as multi-phase flow[218] and multi-componental transport[88].

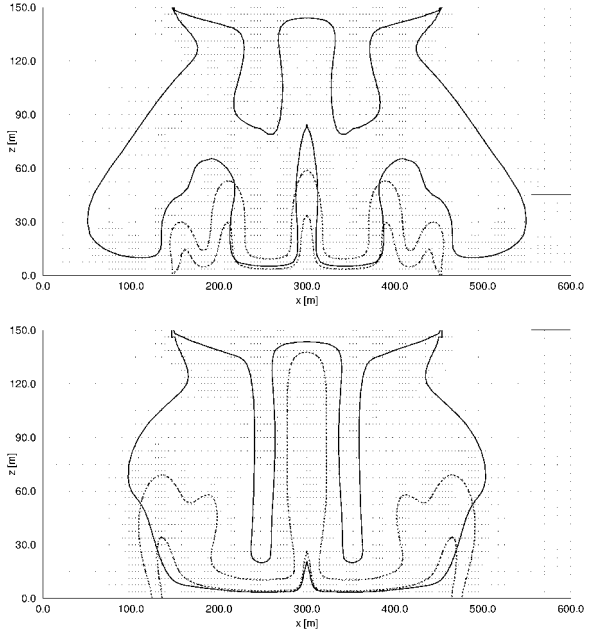

Figure 1.17 Computed salinity distributions of 0.2 and 0.6 normalized isochlors at 10 (top) and 20 years (bottom) for a Turner number of $B = 2$.

1.5.3.4 Three-dimensional Elder problem

Diersch and Kolditz[49] extended the originally two-dimensional Elder problem to three dimensions for studying both the saline convection and the DDC processes. The three-dimensional counterpart consists of a porous box with a square base ($L \times L$) and height d. This box has the same cross-sections along the Cartesian axes as defined in Fig. 1.12 for the two-dimensional sketch. Salinity is held constant, in an areal extent, on the top of the porous box. The parameters correspond to those given in Tab. 1.2. In Diersch and Kolditz's simulations a Galerkin-FEM and an AB/TR time stepping was used, where only the symmetric quarter of the domain is discretized by 48,000 hexahedral elements with 51,701 nodes (Fig. 1.18). In comparison with the mesh requirements we have seen for the two-dimensional problem, such a three-dimensional discretization is considered a 'moderate' resolution.

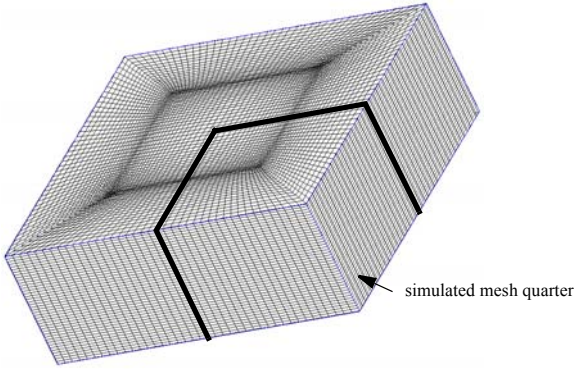

Figure 1.18 Finite element mesh of the three-dimensional Elder problem.

The three-dimensional free convection process is similar to its two-dimensional counterpart, except for some interesting new features. Similar to the 2D case one also finds an upwelling salinity pattern in the centre of the box at later times. The three-dimensional influence becomes apparent in the two horizontal views at an upper elevation of $0.9d$ (135 m) and the middle horizon of $0.5d$ (75 m). At the beginning, the quadratic geometry of the intrusion area on top is visible in the convection pattern (Fig. 1.19a). Fingers appear around the border of the intrusion area and 'blobs' grow down at the four corners. The quadratic pattern evolves into more complicated multi-cellular formations via a number of characteristic stages. More 'blobs' appear until the salinity reaches the bottom (Fig. 1.19b). Then, the structures begin to fuse and the pattern is completely reformed. After this phase a convection pattern remains which has a characteristic diagonal 'star' form (Fig. 1.19c). This 'star' is a result of the geometry of the square intrusion area. It becomes clear that the final formations have a strong dependency on the geometric relations.

The three-dimensional thermohaline Elder problem has been simulated for a Turner number of $B = 5$, where the solutal Rayleigh number Ra_s is again 400 and the Lewis number Le is unity. The complete three-dimensional evolution patterns of the computed salinities and temperatures for simulation times up to 20 years can be found in Diersch and Kolditz[49]. In contrast to the single-diffusive formation the salinity pattern appears more diffusive at later times when the temperature field affects the convection system. Then, the thermally buoyant forces accelerate the contraction process of the sinking salinity plume in the centre. In the final stage, while the single-diffusive convection still provides a central upwelling flow, the thermohaline convection process reveals a single downwelling characteristic (Fig. 1.20).

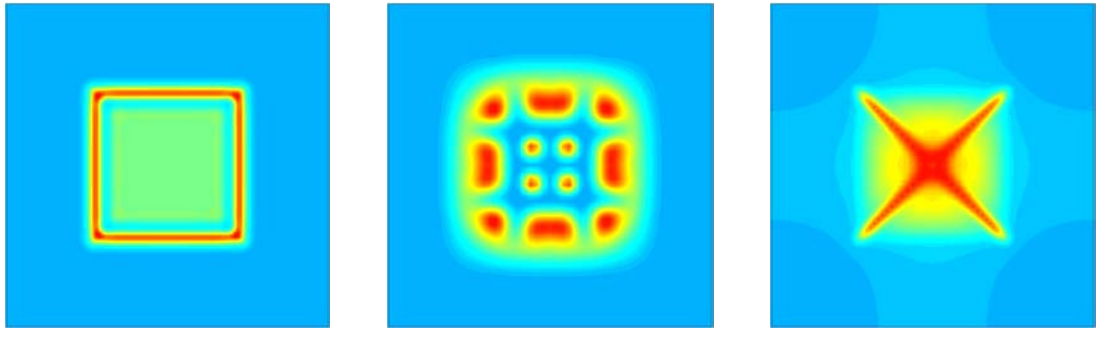

Figure 1.19 Computed salinity patterns of the three-dimensional Elder problem[49].

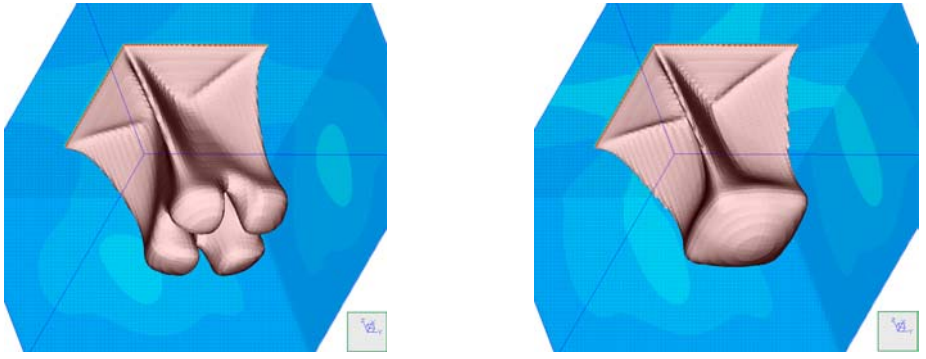

Figure 1.20 Computed isosurfaces of 50% salinity for the three-dimensional Elder problem at t = 20 years: saline convection (left) and thermohaline convection (right).

1.5.4 Salt dome problem

This benchmark was proposed by the participants of the international HYDROCOIN project for the verification of groundwater models (Swedish Nuclear Power Inspectorate 1986). This test case is designed to model variable-density groundwater flow over a hypothetical salt dome, where the geometry is largely simplified. The geometry and boundary conditions of the test problem are shown in Fig. 1.21. The cross-section of the model extends horizontally 900m and vertically 300m. The aquifer is considered to be homogeneous and isotropic. The pressure varies linearly on the top of the aquifer. The other sides are impervious to flow. The concentration on the top is set to zero at the inflow domain. The middle section of the base represents the top of the salt dome with normalized mass concentration of solute equal to unity. On all the remaining parts of the boundary, the normal concentration gradient was set to zero. The simulation parameters are listed in Tab. 1.4. The results are compared for the steady-state solutions.

1.5.4.1 Recirculation versus swept-forward solutions

The salt dome was investigated by several authors (Herbert *et al.*[101], Leijnse[138], Oldenburg and Pruess[161], Oldenburg *et al.*[163], Johns and Rivera[119], Kolditz *et al.*[126], Konikow *et al.*[129], Holzbecher[108] and Younes *et al.*[246], among others). Kolditz *et al.*[126] obtained the same stratified system as Herbert *et al.*[101] already found. A freshwater region with higher velocities is observed in the upper part, where flow is driven by the superimposed pressure gradient on the top of the aquifer (Fig. 1.21a). There is a brine pool along the bottom, where flow with small velocities recirculates (Fig.

1.21b). The outflow of the saltwater is focused on the upper right-hand corner (Fig. 1.21c). Johns and

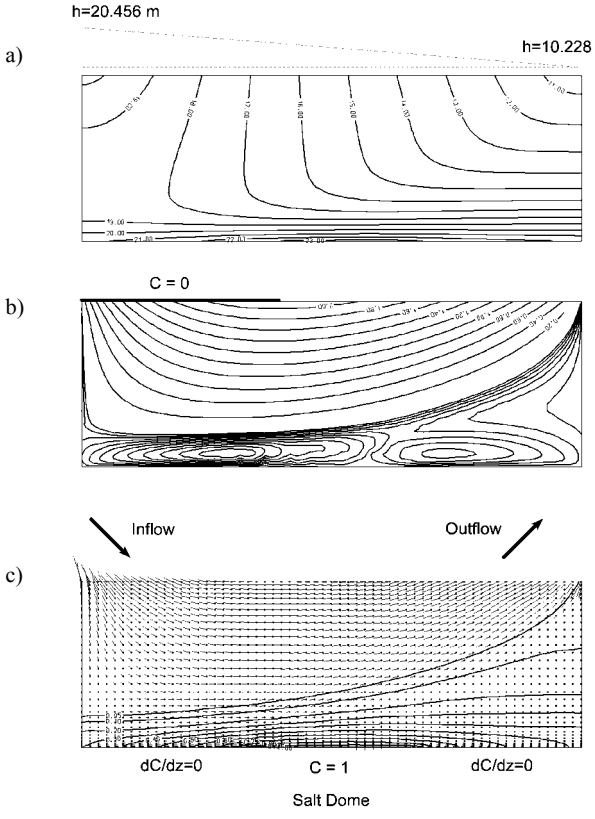

Figure 1.21 Definition of the salt dome problem (HYDROCOIN Level 1 Case 5) - domain and boundary conditions: a) hydraulic head, b) streamline, c) velocity and salinity distributions.

Rivera[119] has reproduced the prior NAMMU results by Herbert *et al*.[101]. In contrast, different results have been presented by Oldenburg and Pruess[161], which has led to a broad discussion on the role of boundary conditions and mechanical dispersion[108,129,163,246]. The conflicting results are summarized in Fig. 1.22 for the case of $D_d = 1.39 \cdot 10^{-8}\ \mathrm{m}^2 s^{-1}$ and $\beta_L = \beta_T \cdot 10 = 20\ \mathrm{m}$. Note that the results by Herbert *et al*.[101] correspond to values of $D_d = 1.39 \cdot 10^{-8}\ \mathrm{m}^2 s^{-1}$ (Fig. 1.22a), whereas Oldenburg and Pruess[161] used a zero molecular diffusivity (Fig. 1.22b). We computed the models for both values of molecular diffusivity (Figs 1.22c and 1.22d) and found nearly identical salinity distributions.

Oldenburg and Pruess[161] called their results a 'fully swept-forward' pattern (Fig. 1.22b). At a first glance the results seem to be quite similar the previous solution, but there is a substantial difference in the hydrodynamic regime concerning the number of convection cells. This swept-forward solution covers only one instead of two recirculating cells near the aquifer bottom (Fig. 1.21b). Oldenburg and Pruess[161] argued that for large dispersive fluxes ($D_d > 2 \cdot 10^{-7}\ \mathrm{m}^2 s^{-1}$) the amount of brine rising from the bottom source is sufficient to cause a clockwise recirculation against the overall counterclockwise flow imposed by the pressure difference along the aquifer top. In contrast, the buoyancy forces are insufficient to overwhelm the pressure-driven flow for small dispersive fluxes when $D_d < 10^{-7}\ \mathrm{m}^2 s^{-1}$. As a consequence, the brine is swept forward from left to right with the overall flow. Younes *et al*.[246] could show that both a swept-forward and a recirculation (Herbert-like) solution can be produced. This depends on the numerical representation of boundary conditions (either salt concentration or salt mass flux) and the magnitudes of D_d, β_L and β_T. They concluded that '*the discussion between swept forward or recirculation remains open but it should be focused on the computation of dispersive fluxes*'.

Table 1.4 Simulation parameters for the salt dome problem

Symbol	Quantity	Value	Unit
L	base length	900	m
d	aquifer thickness (height)	300	m
e	extent of intrusion	300	m
ω_0	reference mass fraction	0	1
μ	dynamic viscosity	$8.9 \cdot 10^{-4}$	$kgm^{-1}s^{-1}$
g	gravitational acceleration	9.80665	ms^{-2}
Δp	pressure difference on top	10^2	kPa
k	permeability of porous medium	10^{-12}	m^2
K	hydraulic conductivity	$1.0986 \cdot 10^{-5}$	ms^{-1}
α	solutal expansion coefficient	0.2036	-
D_d	coefficient of molecular diffusion	$(0, 1.39) \cdot 10^{-8}$	m^2s^{-1}
ε	porosity	0.2	-
β_L	longitudinal dispersivity	20	m
β_T	transverse dispersivity	2	m

Table 1.4 Simulation parameters for the salt dome problem (continued)

Symbol	Quantity	Value	Unit
ρ_0, ρ_s	density of water and solute	$(0.997, 1.2) \cdot 10^3$	kgm^{-3}

In order to examine whether the simplifications invoked by the OB approximation are responsible for the differing results, Kolditz *et al.*[126] employed different levels of the approximation of density variation, i.e., the extended OB approximation (Fig 1.22c) and a full density approximation (Fig. 1.22d). The good agreement between these simulation results indicates that the different levels of density approximations have no influence on the steady-state salinity distribution for this type of problem.

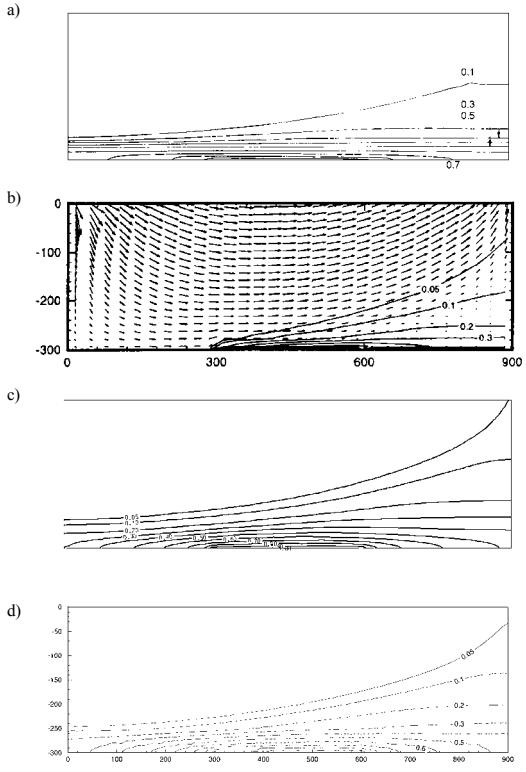

Figure 1.22 Results for the salt dome problem: steady-state salinity contours simulated by a) Herbert *et al.*[101], b) Oldenburg and Pruess[161], c) FEFLOW[126], d) ROCKFLOW[126].

1.5.4.2 Thermohaline salt dome problem

In deep aquifers the saltwater upconing process is subject to the buoyancy influences by a thermal gradient. Diersch and Kolditz[49] studied a thermohaline extension of the salt dome problem. Simulated results of the salt dome problem at a time of 100 years for different buoyancy ratios B are shown in Fig. 1.23, demonstrating that the temperature effect on the saltwater distribution remains negligible or small if compared with the single-diffusive results at higher Turner numbers B. However, as seen for $B = 2$, if the Turner number becomes smaller, vigorous temperature influences on the brine pattern result in form of a 'wavy' salinity field caused by the thermal buoyancy. The 'wavy' salinity characteristics are triggered in front of the salt wedge by thermally driven eddies. As expected, this leads to an increased saltwater effluent on top of the aquifer. Note that a buoyancy ratio of $B = 2$ implies large temperature difference for a high-concentration brine and represents an extreme situation. For the real site behind the present salt dome problem such high temperatures corresponding to $B = 2$ may be unlikely to occur. However, the variants can be valuable as test cases to study the effects of high temperatures, which may, for instance, arise in the vicinity of a disposal facility for heat-emitting waste or in geothermal areas.

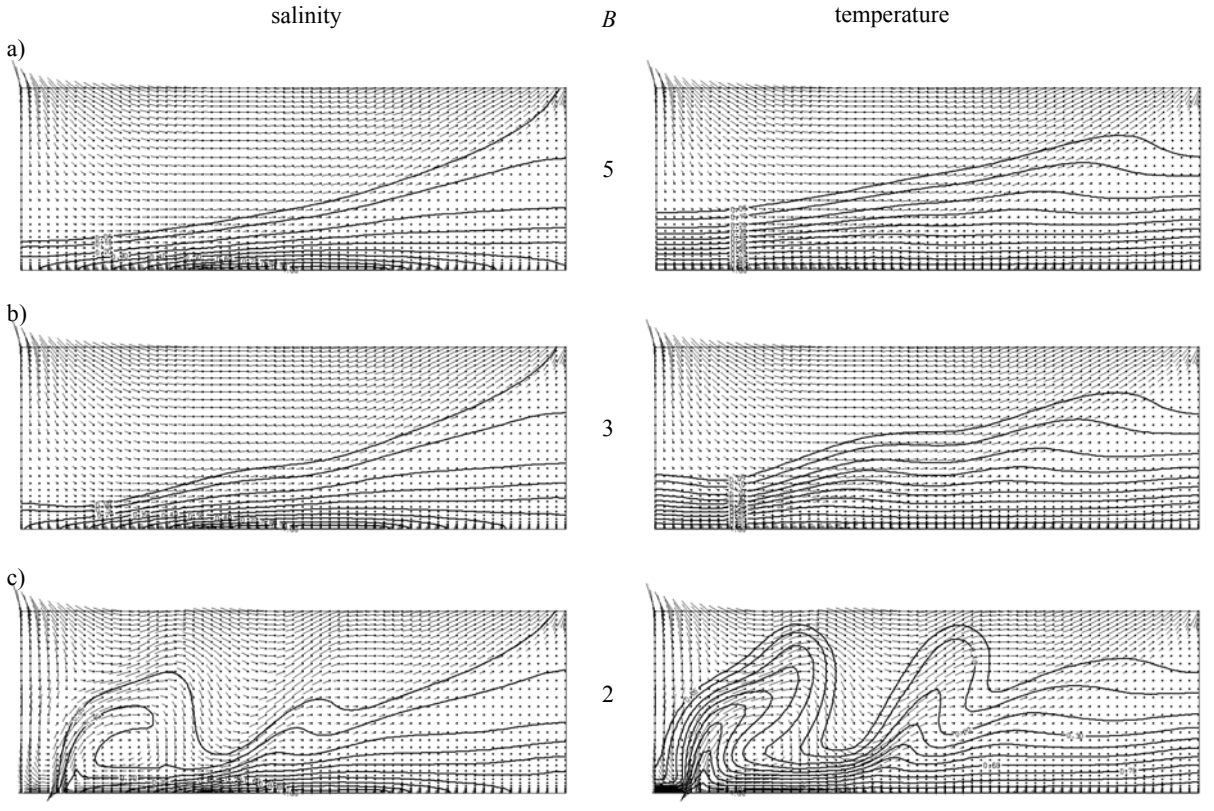

Figure 1.23 Evolution of the thermohaline convection system: computed salinity and temperature distributions at 100 years for different buoyancy ratios (a) $B = 5$, (b) $B = 3$, and (c) $B = 2$.

1.5.5 High concentration flow through a column

High concentration-gradient experiments in a column of glass beads[98,198] have shown that the nonlinear dispersion law (1-9) gives very good agreements with measured breakthrough curves for brines. It is found that the HC dispersion coefficient (1-9), (1-51) $\mathfrak{I}_H$ varies inversely with the flow velocity $\boldsymbol{q}$. Schotting *et al.*[198] have summarized their fitted experiments in the following approximate expression for $\mathfrak{I}_H = \mathfrak{I}_H(\boldsymbol{q})$ as

$$\Im_H(\boldsymbol{q}) = \frac{0.0125}{\|\boldsymbol{q}\|^{1.76}}[\mathrm{s\,m^2/kg}] \qquad (1\text{-}120)$$
$$\text{for} \quad 9\cdot 10^{-5} < \|\boldsymbol{q}\| < 3\cdot 10^{-3}[\mathrm{m/s}]$$

Schotting *et al.*[198] have derived analytical solutions in one dimension, which can be used to verify a simulator for the non-Fickian dispersion law (1-9). We consider the displacement of a high concentration through a column with constant properties. The parameters are summarized in Tab 1.5.

Table 1.5 Simulation parameters for the high concentration displacement experiment

Quantity	Symbol	Magnitude	Unit
Length of column $(-0.5\,\mathrm{m} \le z \le 4.0\,\mathrm{m})$	L	4.5	m
Flow rate	q_o	$3.209\cdot 10^{-5}$	$\mathrm{m\,s^{-1}}$
Porosity	ε	0.2	1
Boundary concentration (brine input)	ω_s	$2.85714\cdot 10^{-1}$	1
Molecular diffusion	D_d	0.0	$\mathrm{m^2 s^{-1}}$
Longitudinal dispersivity	β_L	1.0	m
HC-dispersion coefficient	$\Im_H$	10^4	$\mathrm{m^2 s\,kg^{-1}}$

The column is initially filled with freshwater ρ_o, $\omega = 0$. At $t = 0$ brine $\rho_s = \rho_s(\omega_s)$ starts entering the column with a uniform specific discharge q_o. This implies the following initial condition

$$\omega(z,0) = \begin{cases} \omega_s & \text{for} \quad z < 0 \\ 0 & \text{for} \quad z \ge 0 \end{cases} \qquad (1\text{-}121)$$

A natural gradient boundary condition $\nabla\omega|_{z=4\,\mathrm{m}} \approx 0$ is imposed on the outflowing boundary. For the computations the FEFLOW simulator[44] was employed. The column is discretized by 900 linear quadrilateral elements resulting in a spatial increment of $\Delta z = 0.005\,\mathrm{m}$. For the temporal approximation the AB/TR predictor-corrector scheme with adaptive time stepping (error tolerance 10^{-4}) was used. It required 144 time steps to simulate the displacement process for a dimensionless time t_D defined as

$$t_D = t\frac{q_o^2}{\varepsilon\|\boldsymbol{D}\|} \rightarrow \frac{tq_o}{\varepsilon\beta_L} \qquad (1\text{-}122)$$

up to $t_D = 1.0$. The numerical results are in a very good agreement with the analytical results given by Schotting *et al.*[198] as shown in Fig. 1.24.

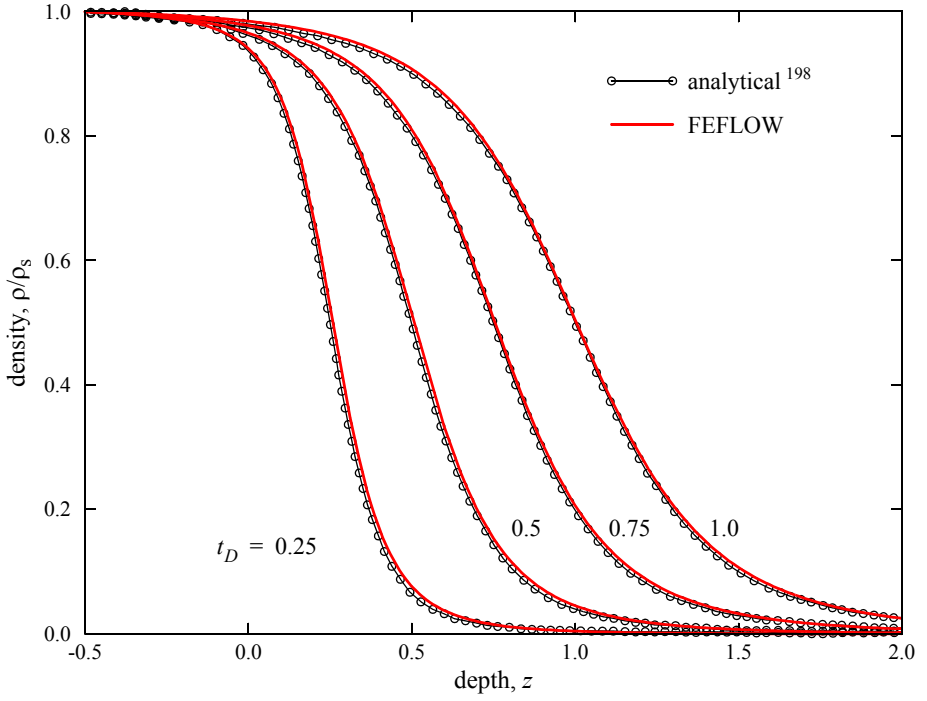

Figure 1.24 Numerical density profiles simulated by FEFLOW at selected dimensionless times t_D in comparison with the semi-explicit analytical solutions given by Schotting *et al.*[198] for a brine displacement in a column at nonlinear dispersion.

1.5.6 Salt lake problem

The salt lake problem as a test case for density-dependent groundwater flow and solute transport was introduced by Simmons *et al.*[207]. It represents convection processes below an idealized evaporating salt lake. The evaporation process results in dense brine overlying less dense fluid leading to a downward convection of salt fingers. The numerical results were compared with those from a laboratory Hele-Shaw cell developed by Wooding *et al.*[242,243]. Fig. 1.25 gives the layout of the experimental Hele-Shaw cell. The tilted cell has a slope at an angle of 5° to the horizontal. The model parameters are listed in Tab. 1.6.

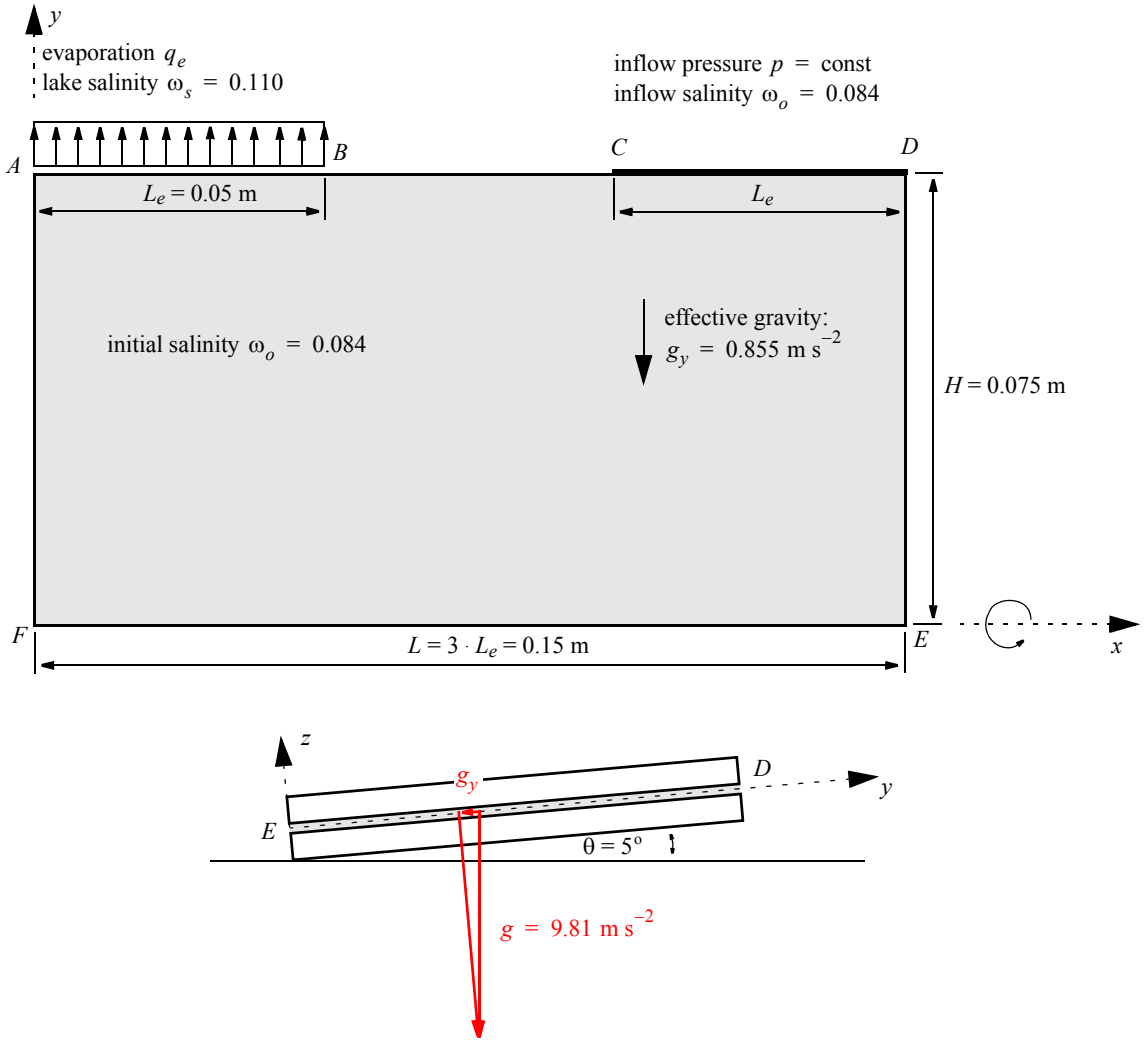

Figure 1.25 Definition of the salt lake problem.

Wooding *et al.*[242,243] described the observations from their experiments as follows: '*At early times many small plumes grow from the evaporating boundary layer. These plumes descend under gravity and tended to coalesce to form larger-scale fingers. Differential growth and coalescence as seen from the Hele-Shaw cell results ... are plausible mechanisms which allow for the growth of millimeter- or centimeter-scale wavelength, corresponding to wavelengths of meters or tens of meters or more which might be possible in nature. These larger plumes tended to maintain their identity during growth. By (dimensionless time)* $t_D = 15.99$ *the leading plume had encountered the lower impermeable boundary and had begun to spread.*'

Table 1.6 Simulation parameters for the salt lake problem

Symbol	Quantity	Value	Unit
H, L	cell height, length	$7.5 \cdot 10^{-2}$, $1.5 \cdot 10^{-1}$	m
L_e	cell evaporation length	$5 \cdot 10^{-2}$	m
b	cell plate spacing	$2.1 \cdot 10^{-4}$	m
θ	cell angle to the horizontal	5	°
ω_0	salinity at inflow and at initial time	$8.4 \cdot 10^{-2}$	1
ω_s	salinity of the lake	$1.1 \cdot 10^{-1}$	1
D_d	coefficient of molecular diffusion	$9 \cdot 10^{-10}$	$m^2 s^{-1}$

Table 1.6 Simulation parameters for the salt lake problem (continued)

Symbol	Quantity	Value	Unit
g_y	effective gravity: $g \sin\theta$	0.855	ms^{-2}
k	permeability of porous medium	$3.68 \cdot 10^{-9}$	m^2
K	hydraulic conductivity	$3.045 \cdot 10^{-3}$	ms^{-1}
ε	porosity	1	-
q_e	evaporation rate	$1.03 \cdot 10^{-6}$	ms^{-1}
γ	compressibility of fluid	$4.5 \cdot 10^{-10}$	Pa^{-1}
α	solutal expansion coefficient	$1.9 \cdot 10^{-2}$	-
β_L	longitudinal dispersivity	$9 \cdot 10^{-10}$	m
β_T	transverse dispersivity	$9 \cdot 10^{-10}$	m
μ	dynamic viscosity	$1.1 \cdot 10^{-3}$	$kgm^{-1}s^{-1}$
ρ_0	fluid density at inflow (at 293.15 K)	$1.0646 \cdot 10^3$	kgm^{-3}
ρ_s	fluid density at saturation (at 293.15 K)	$1.0814 \cdot 10^3$	kgm^{-3}
Ra_s	solutal Rayleigh number $\frac{\alpha K H}{\varepsilon(D_d + \beta_T q_e)}$	4821	-

Simmons *et al*.[207] used two numerical codes for the analysis of the salt lake problem: the SUTRA simulator developed by Voss[231], and a stream-function based finite difference model developed by Wooding *et al*.[242,243]. Simmons *et al*.[207] obtained a reasonable spatial and temporal agreement between the numerical and experimental outcomes. The criteria they choose for comparing the results were: (i) qualitative comparison of the fingering pattern and coalescence with time, (ii) examination of the effect of background advection on the movement of the finger sequence to the left of the cell, (iii) comparison of vertical growth rates of fingers as they move downwards, and (iv) representation of the entrainment of smaller fingers by the larger leading plume that originates at the boundary of the salt lake.

We have revisited the salt lake problem with the FEFLOW simulator[44] using several structured and unstructured meshes with different resolutions in combination with various numerical options. The nearest similarity to the SUTRA findings using an identical spatial resolution (4876 nodes and 4725 elements) was obtained with an AB/TR time stepping scheme and a full upwind technique (Figs 1.26). However, the salt fingers arrive at the cell bottom earlier than in the SUTRA simulations. Additionally, the development of smaller scale fingers at the salt lake boundary is suppressed. Refined meshes (we used up to 169,621 triangular elements with 85,401 nodes) seem to confirm the general features as upwelling-downwelling pattern and the formation of small fingers at the right lake boundary, but the evolution and number of intermediate convection cells is different (Figs 1.27). These results seem to compare better to the experimental findings by Wooding *et al*.[242,243].

Mazzia *et al*.[144] attempted a mesh convergence study for the salt lake problem by using a mixed hybrid FEM. Three meshes were studied, with the finest one consisting of 40,000 triangles with 20,301 edges. Their results have a close similarity with our predictions shown in Fig. 1.27. In agreement with our observations they also found that the predicted finger patterns agree paradoxically much better with the laboratory observations, when simulated on coarse, instead on fine meshes. A mesh convergence was not achieved and they critically concluded that such an assessment is problematic.

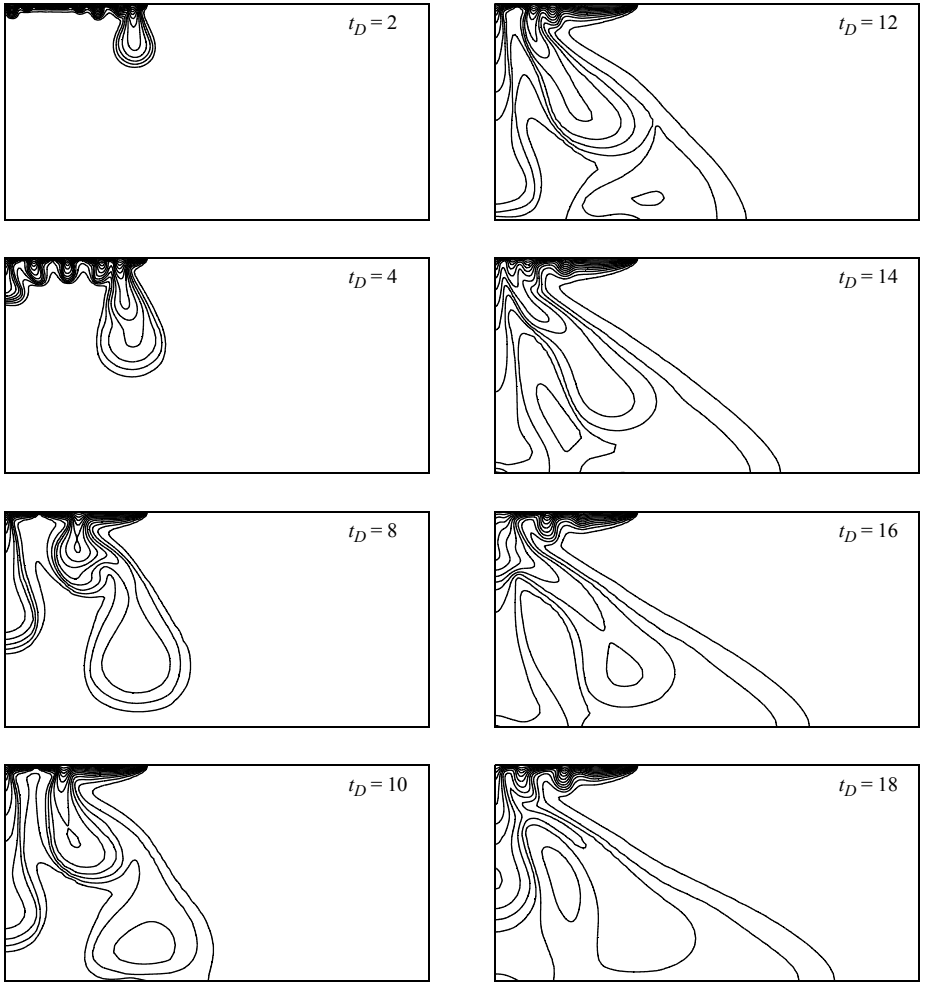

Figure 1.26 Salinities for different dimensionless times t_D. One unit in dimensionless times is equivalent to 21.4 minutes real time. Contour interval is $2 \cdot 10^{-3}$. FEFLOW simulations on a coarse mesh (4733 quadrilateral elements), full upwinding and AB/TR time stepping. Total number of adaptive times steps is 290.

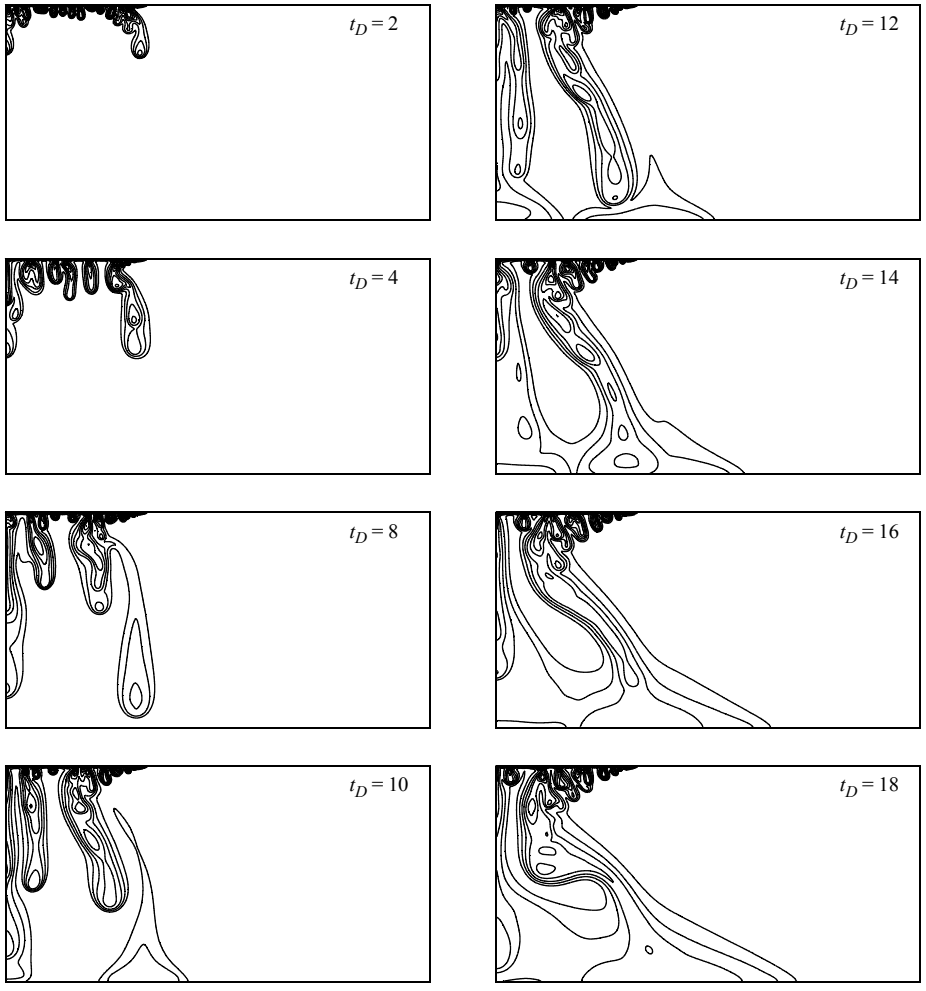

Figure 1.27 Salinities for different dimensionless times t_D. One unit in dimensionless times is equivalent to 21.4 minutes real time. Contour interval is $2 \cdot 10^{-3}$. FEFLOW simulations on a fine mesh (169,621 triangular elements), Galerkin-FEM and AB/TR time stepping. Total number of adaptive times steps is 2700.

Again, it becomes clear that the simulations significantly depend on the discretization and numerical features. Perhaps a new discussion on accurate modeling of the salt lake test case is called for. We should take into account that the Rayleigh number of about 4800 for the salt lake problem is more than ten times larger than for the Elder problem, and we recall that a convection process with a Rayleigh number $Ra > 1000$ is in a range where different branches of flow regimes may exist. The Elder problem thus appears rather simple, compared to the salt lake problem. As the numerical requirements for the Elder problem were already quite expensive, the salt lake problem indeed appears to be a challenge for numerical modelers. Fortunately, (in contrast to many prior benchmarks) experimental results are available here. The main difficulty can be expected in the extremely dynamic behavior of the convection process, where physical perturbations caused by laboratory-scale heterogeneities that trigger instabilities must be mimicked in a numerical simulation. Taking that into account we tend to conclude that the salt lake problem is at the moment essentially unsolved.

1.5.7 Saltpool problem

The saltpool problem was introduced by Oswald[167] and Oswald *et al.*[168]. It represents a three-dimensional saltwater upconing process in a cubic box under the influence of density and hydrodynamic dispersion. A stable layering of saltwater below freshwater is considered in time for two cases: (1) low density case (1% salt mass fraction) and (2) high density case (10% salt mass fraction).

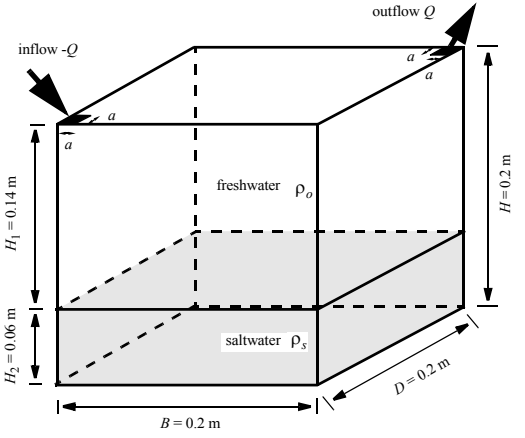

Figure 1.28 Definition of the saltpool problem.

The experimental set-up consists of a cubic container covered by plexiglass walls and filled with dry silica glass beads (average diameter 1.2 mm). At the beginning of the experiment, saltwater is layered below freshwater, forming a horizontal narrow transition zone. Inflow and outflow were possible only via small holes in the corners of the test cube (Fig. 1.28). The box is recharged with freshwater through a single inflow opening at a constant rate Q. Water discharges through the outlet with a variable salinity. In the experiments, salinity breakthrough curves at the outflow opening were measured. The measured mixing concentration at the outflow is in fact very small, i.e. in the order of $\frac{1}{100}$ and $\frac{1}{1000}$ related to the maximum salinity ω_s for the low and high density cases, respectively. The position of the saltwater-freshwater interface was determined by use of the nuclear magnetic resonance (NMR) technique. For a complete description of the

experiments see[167,168].

The saltpool problem has been investigated by various authors with different success (Ackerer *et al.*[2], Thiele[217], Oswald *et al.*[168], Johannsen *et al.*[118], Diersch[47]). The numerical modeling is complicated due to the extremely small dispersivities and a large density contrast particularly for the high density case with 10% mass fraction of salt. The best agreements with the measurements have been recently achieved by Johannsen *et al.*[118], who used the Frolkovic-Knabner algorithm for the consistent velocity approximation in the d^{3}f code. To fit both experiments, however, they had to adjust some parameters within accepted bounds given in parentheses: permeability (20%), porosity (4%) and transverse dispersivity (50%). They studied mesh convergence by using a hierarchy of regular meshes consisting of hexahedral elements, up to mesh level $l = 8$, where the total number of elements is $\mathrm{NE} = 8^l$. It was shown that extremely fine meshes (up to about 17 million nodal points with an element length of 0.78125 mm!) are required to model the high density case with sufficient accuracy. In addition, salinity-dependent viscosity effects had to be taken into account.

We here present results simulated with FEFLOW, where meshes of only moderate sizes are employed. Both, a structured mesh of hexahedral elements with a mesh level of $l = 6$ (mesh A consisting of 274,625 nodes), and an unstructured mesh of pentahedral elements for only the symmetric half, which is partially refined at the outlet (mesh B consisting of 140,010 nodes), were employed. For the computations the Galerkin-FEM without any upwind and the AB/TR adaptive time stepping combined with a one-step Newton were applied, thus ensuring that the numerical results will be second order accurate, both in time and in space. The model parameters are summarized in Tab. 1.7.

Table 1.7 Simulation parameters of the saltpool problem

Quantity	Symbol	Magnitude		Unit
		low density	high density	
cell height	H	0.2		m
cell width	B	0.2		m
cell depth	D	0.2		m
opening width	a	10^{-3}		m
initial freshwater height	H_1	0.14		m
initial saltwater height	H_2	0.06		m
hydraulic conductivity	K	$9.773 \cdot 10^{-3}$		ms^{-1}

Table 1.7 Simulation parameters of the saltpool problem (continued)

Quantity	Symbol	Magnitude		Unit
		low density	high density	
solute expansion coefficient	α	$7.6 \cdot 10^{-3}$	$7.35 \cdot 10^{-2}$	1
diffusion coefficient	D_d	$1.0 \cdot 10^{-9}$		$m^2 s^{-1}$
longitudinal dispersivity	β_L	$1.2 \cdot 10^{-3}$		m
transverse dispersivity	β_T	$1.2 \cdot 10^{-4}$		m
porosity	ε	0.372		1
fluid compressibility	γ	0.0		Pa^{-1}
inflow/outflow rate	Q	$1.89 \cdot 10^{-6}$	$1.83 \cdot 10^{-6}$	$m^3 s^{-1}$
variable fluid viscosity	$\mu = \mu_o(1 + 1.85\omega - 4.1\omega^2 + 44.5\omega^3)$			

The results for both the low (1) and high density cases (2) are presented in Fig 1.29. It reveals the role of density effects in mixing, and in dilution of saltwater, which is mainly controlled by the hydrodynamic dispersion process. In the high density case, the transition zone between saline and freshwater is significantly widened, forming a 'diffusive upcone' below the outlet at very low concentrations. This mixing process is considerably influenced by the advective and dispersive forces acting locally on the saltwater-freshwater interface, which is initially very narrow.

The simulation of the low density case agrees well with the measurements. However, differences in the long-term behavior remain (Fig. 1.29c, left). A previous solution based on the local-projection technique of the velocity approximation completely failed for the high density case, as the saltwater mixing concentration at the outlet is significantly overestimated (Oswald *et al.*[168], Diersch[47]). Using the Frolkovic-Knabner algorithm for the consistent velocity approximation, the computation of the breakthrough curves is now in a reasonable agreement with the experiment (Fig. 1.29c, right). This emphasizes the importance of a consistent velocity approximation for high density situations, which has proven to be a fundamental requirement for the successful solution of the saltpool problem at large density contrasts. Small inconsistencies in the velocity field would have dramatic consequences on the computational results. The data fit can be improved by re-adjusting parameters, in particular the transverse dispersivity β_T, porosity ε, and conductivity K as shown by Johannsen *et al.*[118]. They have also shown in their mesh convergence study that a mesh level of $l = 6$ represents a minimum spatial resolution required for an accurate simulation of the high density case.

The saltpool experiment provides reliable quantitative results for a three-dimensional saltwater mixing process under density effects, which were not available before Oswald's work[167]. From the physical point of view it is interesting to note that the matching of the saltpool experiment, as achieved by Johannsen *et al*.[118] did not require other than common constitutive relationships. Nonlinear (non-Fickian) dispersion effects did not have to be considered. From their results one could implicitly conclude that nonlinear dispersion effects would not play an important role for the saltpool problem at the high density case (10% salinity). This is in contradiction to displacement experiments in columns, where nonlinear dispersion effects have to be introduced to explain the breakthrough behavior of HC brines[98,198]. Further studies seem to be needed in order to evaluate the quantitative effects of nonlinear dispersion on the transverse mixing of dense saltwater along a saltwater-freshwater interface. It is still an open question if the saltpool experiment could be simulated by using the nonlinear dispersion relationship without adjusting independently measured parameters like β_T, ε, K and others. Taking the observations for column brine displacement into account, it is unlikely that the nonlinear dispersion effects can be disregarded in the saltpool experiment. One explanation could be that the convective time scale of the saltpool experiment is much shorter than the time scale of the action of gravity to cancel out horizontal density gradients due to local heterogeneities in the porous medium, which give rise to a reduction of the effective dispersivities. Details about these time scales can be found in Duijn *et al*.[55].

From the practical point of view, the numerical studies[118] have shown that fine and extremely dense meshes are required to attain a reasonable agreement with the measurements. Consequently, three-dimensional brine transport (upconing) problems in practical large-scale applications with correspondingly small dispersivities would require huge models, which cannot be handled on available computers, unless the requirements in the quantitative accuracy are significantly reduced. On the other hand, regularly structured meshes, such as the ones used by Johannsen *et al*.[118], represent a limitation for the modeling of natural systems with complex geometry. In order to study mesh effects in more detail, results for structured and unstructured meshes should be compared.

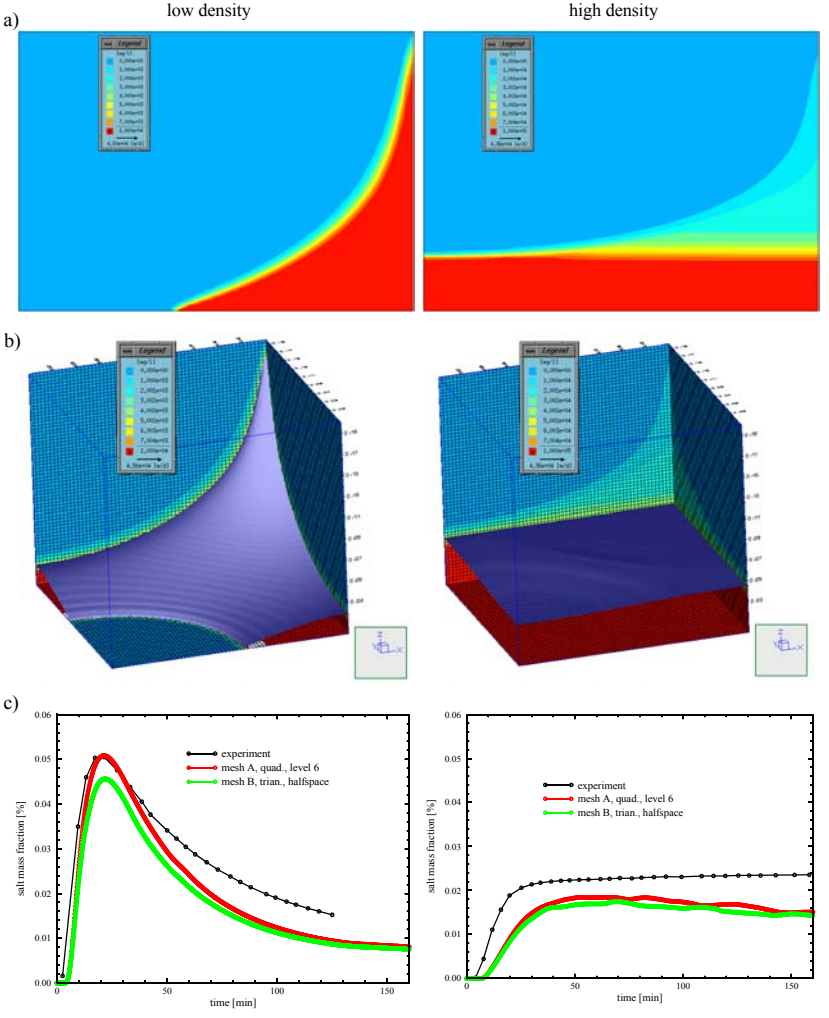

Figure 1.29 Computational results (FEFLOW) of the saltpool problem for the low (left) and high density cases (right): a) cross-sectional salinity distribution, b) 50% salinity surface at t = 160 min, c) salinity breakthrough curves at the outlet obtained for meshes A and B, circles correspond to experimental results.

1.5.8 Variably saturated flow cell

The benchmark cases in the preceding sections are about water-saturated systems. This test case refers to density-dependent flow in a variably saturated porous medium. The experimental and numerical investigations were carried out by Thorenz *et al.*[219]. Figure 1.30 shows a sketch of the experimental set-up consisting of a sand box with dimensions of 0.958 m length, 0.478 m height and 0.105 m width. It was equipped with sixteen perforated tubes for tracer injection and sample extraction. Tracer injection (red dye) was conducted to visualize the flow behavior. The filling material was a clean, natural, silica sand local to the Rehovot (Israel) area. Before conducting the experiments, the sand box was prepared by CO_2 flooding through the lower row of injection tubes to remove as much air as possible. As CO_2 dissolves easily in water, the system becomes almost free of bubbles during subsequent water saturation. Several imbibition-drainage cycles were performed to minimize hysteresis effects. The flow process was controlled by the hydraulic boundary conditions applied: a chamber filled with saltwater (ρ = 1097 kg/m^3) at the right hand side and a chamber filled with freshwater (ρ = 1067 kg/m^3) at the left hand side. The hydrostatic boundary conditions for fluid pressures at the saltwater and freshwater sides were adjusted by corresponding water levels, which were about half of the height of the flow cell. Therefore, a saturated (fresh/saltwater) zone in the lower half and an unsaturated zone in the upper half were established.

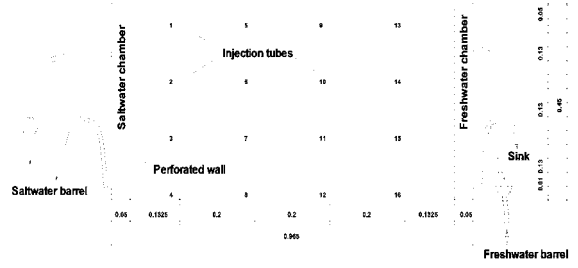

Figure 1.30 Sketch of the experimental set-up (Thorenz *et al.*[219]).

The parameters of the system are summarized in Tab. 1.8. The intrinsic permeability was determined from flux measurements for a small pressure gradient under saturated conditions. The measured capillary pressure/saturation relationship fits very well to a van Genuchten-type curve. The longitudinal dispersion length was set to the diameter of the largest sand grains, while the transverse dispersion length was assumed to be 1/10 of the longitudinal one. Solute density was assumed to be a linear function of salt concentration. The diffusion coefficient is in fact the only calibration parameter of the model.

The experiments were prepared based on numerical simulations dealing with different boundary conditions at two sides of the flow cell (inlet and outlet chambers). As a result of the experimental design, those boundary conditions could be identified for the principal flow patterns: freshwater flushing, saltwater tongue with freshwater counter flow, and saltwater flushing. Therefore, experiments could be focused on case studies of convection cell building. Within the selected experi-

ment, different cases were tested: set-up A - equal bottom pressure at both sides of the flow cell (i.e. at salt and freshwater inlet chambers), set-up C - equal water table at both sides of the flow cell, and an intermediate situation. In these experiments, tracer injections (red dye) at 16 tubes were conducted to visualize the flow pattern. During the experiments, picture series of the tracer movement were taken with a digital still camera.

Table 1.8 Simulation parameters for the variably saturated flow cell problem

Symbol	Quantity	Value	Unit
D_d	coefficient of molecular diffusion (tracer and salt)	$4 \cdot 10^{-6}$	$m^2 s^{-1}$
k	permeability of porous medium	$5 \cdot 10^{-11}$	m^2
k_r	relative permeability	$[(s - s_r)/(s_{max} - s_r)]^4$	-
ε	porosity	0.36	-
β_L	longitudinal dispersivity	$5 \cdot 10^{-4}$	m
β_T	transverse dispersivity	$5 \cdot 10^{-5}$	m
μ	dynamic viscosity	10^{-3}	$kgm^{-1}s^{-1}$
ρ_0	density of water	$1.067 \cdot 10^3$	kgm^{-3}
ρ_s	density of solute	$1.097 \cdot 10^3$	kgm^{-3}
s_r	residual saturation	0.15	-
s_{max}	maximum saturation	1.0	-

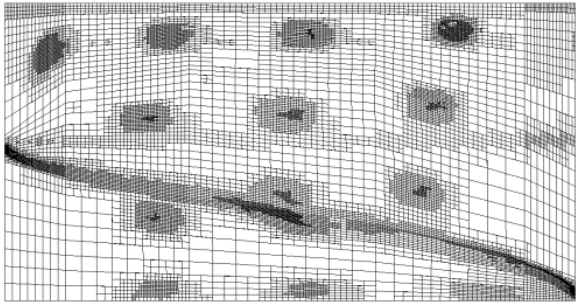

Figure 1.31 Dynamically adapted finite element mesh used for simulating the variably saturated flow cell problem (ROCKFLOW model).

The numerical challenge for this problem is to model density-dependent, as well as multiphase flow processes, i.e. to deal with two nonlinear effects simultaneously. Moreover, the numerical simulations were performed based on an AMR finite-element method, which in turn is based on error indicators for multiple field quantities, such as pressure, saturation, and salt and tracer concentrations[121]. The refinement/coarsening algorithm is hierarchical, i.e. in the two-dimensional case the next level produces four new child elements from a starting parent element and vice versa. A maximum of allowed refinement levels can be defined to control the numerical expense. The initial mesh for the variably saturated flow cell was built with only 25 elements, and during the AMR process up to 14000 quadrilateral elements were generated (Fig. 1.31). This resolution was necessary in order to satisfy a certain error norm. The mesh convergence process can be observed by successively increasing the number of maximum refinement levels. The refined mesh indicates areas with large gradients, e.g. tracer injection

areas, the capillary fringe, and the saltwater-freshwater interface (Fig. 1.31). More details of the numerical method for multi-phase and density-driven flows are described by Thorenz[218]. A direct comparison of the experiments and associated numerical simulations are presented by Thorenz *et al*.[219] in two ways: first, by qualitative analysis of tracer migration from the injection points, and second, by quantitative analysis of streamline patterns extracted from the photographs. The flow system can be separated into two main regions. In the lower area, a saltwater tongue along with a convection cell establishes itself. In the upper area, a significant counter flow develops, which transports freshwater through both the saturated, and unsaturated zones. The experiments show a quite different flow behavior in the upper part. Set-up A shows a significant flow in the unsaturated zone too, whereas set-up C is characterized by a fast movement of saltwater in the saturated zone, and slow anti-clockwise convection of freshwater in the unsaturated zone. In all simulations, the position of the saltwater tongue as well as the significant flow features could be reproduced very well. As an example, we show the computed tracer distribution in the flow cell (Fig. 1.32).

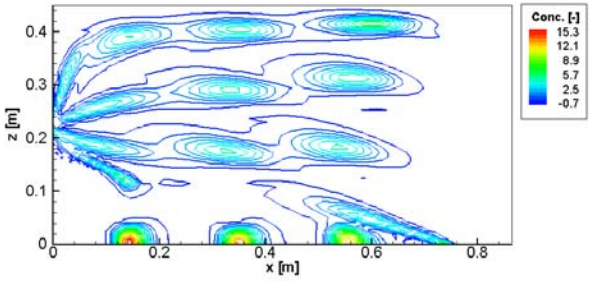

Figure 1.32 Simulated tracer distribution in the variably saturated flow cell.

1.6 Field-related Large-scale Applications

There is an increasing desire in modeling density-dependent problem for real site and large-scale applications. Of great interest in water resources are saltwater intrusion processes, for which many computational studies at a regional scale were performed in the past, e.g.,[5,26,41,75,81,117,128,135,158,169,173,182,202,204,205,209,225,232,244]. Models were also used for simulating flow, brine, and heat transport in large sedimentary basins, rifts and

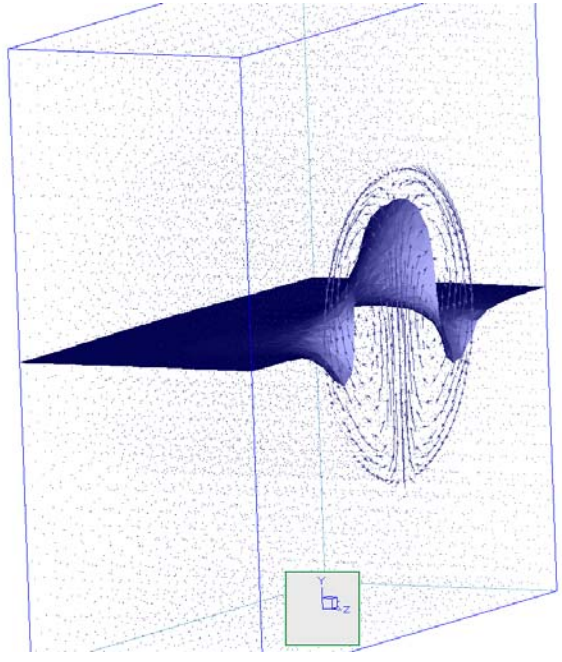

Figure 1.33 Simulated HDR recirculation process: three-dimensional flow field and temperture isosurface in the fracture and rock formation (FEFLOW model).

deep formations, e.g.,[30,50,124,162,178,238]. For the latter we illustrate three examples of recent concern. The modeling of heat extraction from hot dry rocks (HDR) is three-dimensional and covers far-field and local field effects in hydraulically fractured rock massifs. In the cracked rock a fluid circulation system is established and heat exchanges at the surfaces of the fractures. Figure 1.33 exhibits simulation results for flow and heat transport in a HDR system. In a holistic finite element model for a fractured-porous medium, fractures (represented by two-dimensional elements) and the contacted rock mass (represented by three-dimensional elements) are explicitly coupled. The thermally driven recirculation regime in the single fracture is described by a Hagen-Poiseuille law (1-54). The advantage of such a holistic three-dimensional approach is that the interaction between fracture and rock can be modeled more realistically.

The second example is in the domain of geophysics and refers to the study of a large sedimentary basin in Northern Germany involving geothermal buoyancy and brines in deep locations. Clausnitzer *et al*.[30] used a two-dimensional FVM to model the geothermal (without salinity) effects in the layered geologic system. The cross-sectional domain they studied measured 230 km in the length and 8 km in the depth. A geothermal gradient of 35 K/km has been imposed. An unstructured mesh consisting of about 10^5 triangular elements was used. A typical outcome is shown in Fig. 1.34, revealing a complex multicellular convection behavior in higher permeability layers. The mesh used is much finer than the simulated convection cells. Future modeling must be based on a fully thermohaline formulation and extension to three dimensions. The third example shown in Fig. 1.35 concerns two simulations of density-coupled flow through a strongly heterogeneous medium representing the caprock over salt formations in Northern Germany. The displayed variations in the velocity field symbolize the heterogeneity of the hydraulic conductivity very well. Due to the specific layering, flow channelling occurs above the salt dome. Another significant implication concerns the flow field itself. Figure 1.35a illustrates the velocity distribution if density effects are neglected, whereas Fig. 1.35b shows a convective cellular pattern occurring if density effects are taken into account. Note that this convection cell is entrapped in a layer with a larger

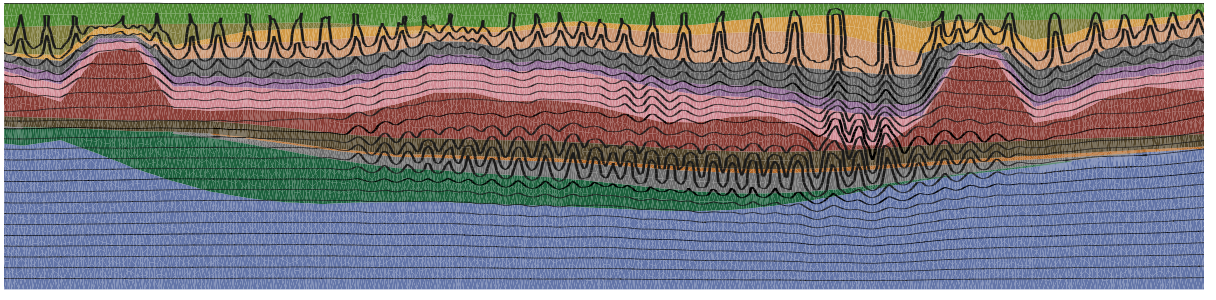

Figure 1.34 Cellular convection pattern in a large-scale geothermal application: two-dimensional FVM model of a sedimentary basin, cross-sectional layer structure and simulated isotherms (from Clausnitzer *et al*.[30]).

hydraulic conductivity as in the adjacent formations. This indicates that the evolution of convection cells, and in particular, its extensions may depend to a large extent on the heterogeneity of the subsurface system.

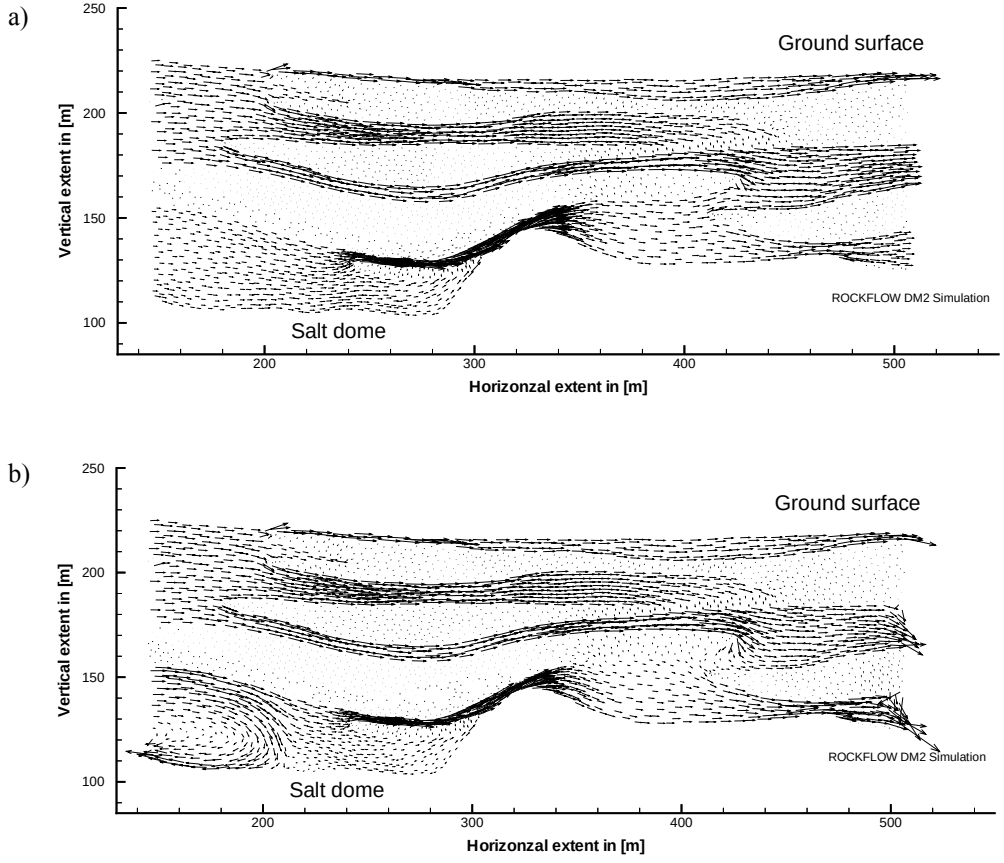

Figure 1.35 Groundwater flow through the caprock of a glacial aquifer: a) neglecting density effects and b) including density effects.

Large-scale density-variable simulations that are to accommodate natural heterogeneity together with strong buoyancy forces and steep gradients have an inherent need for expensive numerical meshes. In reality, the computational power of the available hardware often dictates a discretization for large problems that is rather coarse, compared to that of academic and laboratory studies, such as the saltpool problem discussed earlier. The numerical compromise thus implied, typically involves *damping* and *smoothing*. In some codes the user will not (or never) notice that this internally occurs: *He solves the problem by changing the physics of the problem*. Robustness is then obtained at the expense of accuracy. Indeed, the preferable approach would be to do any necessary changes in a deliberate and educated manner. For instance, Voss[232] recommends an increase in the dispersivity in those locations where critical oscillation artefacts arise (this represents a localized streamline upwinding (1-113)), while tolerating all wiggles that do not seriously affect the rest of the simulated field, especially if the area of interest is sufficiently distant from the numerical instability. A perhaps extreme position (well-known in the community of computational fluid mechanics) is taken by Gresho and Sani[86] who oppose, in principle, any artificial damping measures: '*Don't suppress the wiggles - they're telling you something!*'. There is, unfortunately, no panacea, but the practitioner should be aware of the necessary compromises involved, and use a given method with due caution and 'healthy skepticism'.

Moreover, heterogeneity occurs in each geologic system, which is a general concern in subsurface modeling. Particularly, transport phenomena in natural porous media are controlled by the spatial variations in heterogeneous conductivity fields; for a broad discussion of this topic see Dagan[35]. Heterogeneity can also have serious consequences for density-dependent processes. A natural system is self-perturbing. As discussed by Simmons *et al*.[206], heterogeneity in hydraulic properties can perturb flow over many length scales (from slight differences in pore geometry to larger heterogeneities at the regional scale), triggering instabilities in density stratified systems. This is particularly true for physically unstable situations (dense over light mass fractions, hot below cold temperatures), but also important in potentially stable situations (brine water underneath freshwater). The mixing process along a saltwater-freshwater interface can be significantly affected by the nonuniform velocities, which can produce instabilities at the local scale, resulting in a corrugated interface. At a large(r) scale this appears as an additional smoothing (mixing) effect and is often interpreted as enlarged mechanical dispersion for a stable layering. As it is indeed impossible to resolve these local-scale effects in a regional model, the idea has been presented, to extend the phenomenological law of mixing to a higher-order, non-Fickian law (1-9), in which the density effects are incorporated (Hassanizadeh and Leijnse[98] and Hassanizadeh[92]). The HC dispersion coefficient $\mathfrak{I}_H$ appears as an additional 'free' dispersion parameter and it remains for future work to assess and quantify that relation for field applications.

Interfacial instabilities in relation to contamination problems are another serious concern. A dense plume in a less dense liquid creates complex patterns of fingering, which significantly enhances the plume mixing. The fingers can become widespread and careful modeling is needed to resolve them within a numerical framework. Schincariol *et al*.[195,196] and Fan and Kahawita[62] have simulated this type of fingering insta-

bilities in a tank experiment. They showed that small-scale heterogeneities play an important role in controlling instability growth. Their simulations suggest that low-permeability lenses can effectively dampen instability growth or, in the case of only a weakly unstable plume, completely stabilize any perturbations. It is obvious that the characteristics of the permeability field must be incorporated in stability assessments for natural and field-scale porous media. It is a topic of future research to better describe the onset of instabilities and their subsequent growth or decay in heterogeneous media. Simmons *et al.*[206] pointed out that the Rayleigh number should be questioned in their application at the field scale in heterogeneous porous media. Here, an average hydraulic property is not representative, and the choice of an appropriate non-dimensional length scale d is rather problematic in practical cases.

1.7 Critical Aspects and Challenges

The role of numerical modeling in density-dependent problems is at least twofold. Modeling is a tool of prediction and interpretation in real-site applications. On the other hand, it is required to improve our understanding of the processes. Paradigmatic and laboratory problems are applied to study the convection phenomena in detail via numerical methods. The modeling is based on a theoretical and conceptual idealization. Due to the numerical approach, the solutions are approximative and discretization errors inevitably occur. The consequences of those errors on the complexity of the solutions is often not sufficiently clear. Benchmark tests can provide assessments with respect to accuracy and reliability of numerical approaches. There is progress in this field; however, various open questions remain and the modeling of density-dependent and convective processes is a difficult and challenging task.

Satisfactory agreements between the different solution strategies and methods have been attained for problems with small or moderate density effects (e.g., Henry, Elder, salt dome problem). Differences in the solutions are caused more by inconsistent boundary conditions in the benchmarks than by the chosen numerical methods. It is now accepted that density-dependent problems require a certain degree of refinement in the numerical solutions. New solution techniques (e.g. mixed hybrid FEM) that match the previous findings on similar (or slightly coarser) meshes have been applied. Oswald's saltpool problem[167] has provided a new platform for testing three-dimensional density model codes. It has pushed developments that finally led to improved techniques of computing consistent velocities, such as in the form of the Frolkovic-Knabner algorithm[72,131]. Such techniques are required to accurately model strong density contrasts in narrow transition zones.

From the physical point of view, there is a seeming contradiction between the saltpool observations for the dense case, and those which have been found for brine displacement experiments in columns[198]. Johannsen *et al.*[118] could fit the model predictions to the saltpool measurements without resorting to a higher order non-Fickian dispersion model. For a good match they changed parameters (porosity, transverse dispersivity, permeability) within tolerable bounds. Further studies are needed to clarify the interrelation of parameter variability, which controls the mixing under density influences. Johannsen *et al.*[118] have shown that three-

dimensional variable density problems require very fine, structured meshes. Adaptive methods on fully unstructured meshes could provide a more efficient alternative. They have yet to be examined for the salt-pool problem. An alternative strategy to overcome the difficulties and computational burden associated with adaptive meshing in three (and two) dimensions is found in meshless methods (see, Belytschko *et al*.[19] for an overview). Prax *et al*.[181] have already shown the applicability of meshless methods for two-dimensional free convection problems in porous media.

The simulating of convection processes with high Rayleigh numbers, i.e., distinctly above the second critical limit Ra_{c2}, is a challenging problem. The salt lake problem belongs to that category. It has been claimed[207] that the salt lake problem can be a very powerful new benchmark and that models being tested are in good agreement with laboratory experiment. Being cautious, we do not fully agree. The simulated convective patterns[144,207] have, indeed, a certain similarity with the experiment, but they depart distinctly from the observations with respect to the finger number, extent and behavior of the fingers. Mazzia *et al*.[144] have expressed their difficulties with the salt lake problem as follows: '*... grid convergence cannot be considered achieved, even if a very fine grid has been used. This behavior is mainly due to perturbations induced by the local truncation error that prompts the formation of fingers because of the highly unstable character of physical process. ... small perturbation of the initial data cause large perturbations in the final solution.*'

Schincariol *et al*.[195] observed in their density plume problem that the perturbations created by propagation of numerical errors are virtually uncontrollable. Small alterations to the dispersion parameters, or spatial and temporal discretization can cause different types of instabilities to form. Schincariol *et al*.[195] required the control of numerical perturbations by reducing (minimizing) numerical errors. This must lead to fine meshes and small timesteps when using common numerical approaches. The questions that arise naturally are what perturbation is no longer significant for a convection process, and what error in the numerical scheme can be tolerated. Indeed, the danger in simulating such highly nonlinear convection problems has two faces: A scheme which is only conditionally stable, but of higher accuracy, is prone to create nonphysical perturbations due to small wiggles in the solutions, unless the element size and the timestep are sufficiently small. On the other hand, a scheme which is unconditionally stable, but possesses a lower accuracy, smooths out physically-caused perturbations, unless the element size and the timestep are sufficiently small. It seems that a high spatial and temporal resolution is unavoidable if high-density convection processes are to be modeled.

1.8 Summary

Modeling of density-dependent flow and transport in porous media is of importance in a number of disciplines, including groundwater hydrology, reservoir mechanics, underground nuclear engineering, geophysics, and material science. We have described its current status with emphasis on both physical, and numerical aspects. The modeling framework is based on a set of continuum balance equations, which has to be closed by phenomenological laws, EOS, and constitutive relations. The set of governing equations describing den-

sity-dependent flow and transport in porous media is strongly coupled and nonlinear, due to the dependence of material behavior on salt concentration and temperature. The OB approximation and its (non-Boussinesq) extension for density dependent terms has been considered. In a generalized approach the model formulation includes thermal and solute density effects, DDC phenomena, fluid viscosity and compressibility effects, saturated and unsaturated porous media, non-Darcian and non-Fickian effects.

Physical instability is an important aspect in density-driven flow and transport. Perturbation approaches, linear stability theory, and bifurcation theory give insight into the dynamic behavior of a convection process. For large Rayleigh numbers, different evolutions in the solution appear that are triggered and controlled by perturbations. Such perturbations can have true physical meaning or can be purely numerical. The conditions occurred initially, and subsequently influence and determine the behavior of a convection process. The transition between different modes can be sudden. At large Rayleigh numbers, it becomes questionable whether the process is predicable by a completely deterministic approach. It seems of questionable merit to apply refined and perfect numerical techniques, such as direct numerical simulation (DNS), where all of relevant length scales are resolved with highly refined meshes, without also incorporating the probabilistic character of the dynamic behavior. This includes an analysis of the influence of a representative set of random perturbations on the evolution of solutions. We recall once more Horne and Caltagirone[111] who more than 20 years ago advised '... *to avoid solutions mathematically correct but physically unlikely.*'

The numerical approach of the related conservation equations for mass, momentum, and energy should be appropriately formulated with respect to actual extensive balance quantities in a conservative form. An error in the discrete conservativity can result in an artificially enhanced non-Boussinesq influence relative to the physically correct solution. Local consistency in the velocity approximation at high density contrasts has proven a fundamental requirement. Essential, for example, in the solution of the three-dimensional salt-pool experiment, it was successfully implemented in the Frolkovic-Knabner algorithm, while standard techniques such as local or global projection as a 'natural' weighted-integral form in FEM lead to a significant overestimation of mixing salinities at high concentrations. Consistency represents an additional requirement for an accurate velocity approximation satisfying the hydrostatic equilibrium. The error-based AMR technique can be applied to improve numerical accuracy. Mesh convergence studies are most interesting to become aware of critical states during the evolution of convection processes.

Benchmarking plays an important role in modeling variable-density flow and transport. Analytical solutions for those problems are clearly limited to simplified cases. When choosing reference laboratory experiments for physical benchmarks, the dynamic character of a convection process has to be considered. For example, flow in a Hele-Shaw cell concerns a pure fluid and is not really through a porous medium. There are also technical difficulties involved in obtaining experimental information on the flow patterns in a real porous medium. The established benchmark tests, such as the Henry, Elder, salt dome, and saltpool problems,

have been understood and solved quite well. At the same time, we note that the presence of non-unique stationary solutions, as stated in the Elder problem[74], causes obvious difficulties for mesh convergence studies. As the central upwelling pattern is only one solution of many (perhaps three), it cannot by itself be considered as proof of correctness for a numerical solution of the Elder problem. Moreover, fingering experiments at high Rayleigh numbers, such as the salt lake problem, are fundamentally prone to a propagation of instabilities triggered by small perturbations, which can be neither measured nor simulated. Mesh refinement and unstructured meshes can significantly perturb a solution, and we can find the paradox that finer meshes result in greater deviations from observations than coarser discretizations, and that regular coarse meshes seem more accurate than fine irregular meshes.

A particularly challenging problem is the description of dense solute and heat transport in areas of heterogeneity. The process of mixing across interfaces subject to density effects remains to be studied in greater detail. Microscopic models can contribute to validation and quantification of non-Fickian mechanisms in a continuum approach. Heterogeneity is a key problem, particularly for fingering processes. Heterogeneity plays an important role concerning a possible damping or amplification of perturbations through the system. It has to be clarified, what level of schematization is permissible, and what type of stability criterion is representative for given heterogeneous conditions.

Large-scale density-variable simulations have an inherent need for expensive numerical meshes. Adaptive techniques, unstructured meshes, and parallel processing are most promising in the maturation of real-field modeling. However, adaptive and unstructured irregular geometries are prone to uncontrollable perturbations with consequences on the conditioning of the resulting matrix systems. Therefore, robust, efficient, and accurate solving strategies are required, particularly for three-dimensional applications.

Acknowledgements

The authors acknowledge C.P. Jackson (Serco Group, UK) and three anonymous reviewers for their suggestions and critical discussions of the work. We are grateful to S.M. Hassanizadeh (Delft University) for its constructive comments on the manuscript. HJGD thanks P. Frolkovic (IWR Heidelberg) for his support and useful discussions regarding consistent velocity approximations. V. Clausnitzer (WASY Berlin) is thanked for providing his field-modeling results of the large sedimentary basin in Northern Germany. OK wishes to acknowledge his former PhD students from the Groundwater Modeling Group of the Institute of Fluid Mechanics in Hannover, Germany, C. Thorenz, R. Kaiser, and A. Habbar, for providing material from their theses for this paper. The authors acknowledge J. de Jonge for checking and improving the English phrasing of the manuscript.

References

1. Ackerer P, Younes A, Mosé R. Modeling variable density flow and solute transport in porous medium: 1. Numerical model and verification. Transport in Porous Media 1999;35(3):345-373.
2. Ackerer P, Younes A, Oswald SE, Kinzelbach W. On modeling of density driven flow. In Stauffer *et al*., editors. Calibration and

reliability in groundwater modeling, Proc. ModelCARE 99 Conf Zurich, IAHS Publ no 265;2000:377-384.
3. Aidun CK. Stability of convection rolls in porous media. In: Bifurcation phenomena in thermal processes and convection. Amer Soc Mech Engrs ASME HTD 1987;94:31-36.
4. Aidun CK, Steen PH. Transition of oscillatory convective heat transfer in a fluid-saturated porous medium. AIAA J Thermophys Heat Transfer 1987;1:268-273.
5. Aliewi AS, Mackay R, Jayyousi A, Nasereddin K, Mushtaha A, Yaqubi A. Numerical simulation of the movement of saltwater under skimming and scavenger pumping in the pleistocene aquifer of Gaza and Jericho areas, Palestine. Transport in Porous Media 2001;43(1):195-212.
6. Al-Lawatia M, Sharpley RC, Wang H. Second-order characteristic methods for advection-diffusion equations and comparisons to other schemes. Adv Water Resour 1999;22(7):741-768.
7. Babuska I. Reliability of computational mechanics. In: Whiteman JR, editor. The mathematics of finite elements and applications- Highlights 1993. Chichester: J Wiley; 1994;26-44.
8. Badon-Ghyben W. Nota in verband met de voorgenomen putboring nabij Amsterdam (Notes on the probable results of well drilling near Amsterdam). In: Tijdschrift van het Kononklijk Instituut van Ingenieurs. The Hague 1888;9:8-22.
9. Baker AJ. Finite element method. In: Johnson RW, editor. The handbook of fluid dynamics, Chapter 28. CRC Press, Springer; 1998.
10. Bank RE, Sherman AH, Weiser A. Refinement algorithms and data structure for regular local mesh refinement. In: Steplemen R at al. editors. Scientific computing. IMACS, North Holland; 1983.
11. Barten W, Lücke M, Kamps M, Schmitz R. Convection in binary fluid mixtures. I. Extended traveling-wave and stationary states. Physical Review 1995;Part A 51(6):5636-5661.
12. Bear J. Dynamics of fluids in porous media. New York: McGraw-Hill; 1972.
13. Bear J. Conceptual and mathematical modeling. In: Bear J, Cheng AHD, Sorek S, Quazar D, Herrera I, editors. Seawater intrusion in coastal aquifers. Dordrecht: Kluwer Publ; 1999:127-161.
14. Bear J, Bachmat Y. Introduction to modeling of transport phenomena in porous media. Dordrecht: Kluwer Publ; 1991.
15. Bear J, Tsang C-F, Marsily de G. (eds.) Flow and contaminant transport in fractured rock. Academic Press, San Diego; 1993.
16. Beck, JL. Convection in a box of porous material saturated with fluid. Phys Fluids 1972;15:1377-1383.
17. Beckie R, Wood EF, Aldama AA. Mixed finite element simulation of saturated groundwater flow using a multigrid accelerated domain decomposition technique. Water Resour Res 1993;29(9):3145-3157.
18. Bejan A. Convective heat transfer in porous media. New York: J Wiley; 1984.
19. Belytschko T, Krongauz Y, Organ D, Fleming M, Krysl P. Meshless methods: an overview and recent developments. Comput Meth Appl Mech Eng 1996;139:4-47.
20. Brandt A, Fernando HJS (eds.) Double-diffusive convection. Geophysical Monograph 94, American Geophysical Union, Washington DC; 1995.
21. Brezzi F, Fortin M. Mixed and hybrid finite element methods. New York:Springer; 1991.
22. Bués MA, Oltean C. Numerical simulations for saltwater intrusion by the mixed hybrid finite element method and discontinuous finite element method. Transport in Porous Media 2000;40(2);171-200.
23. Caltagirone JP, Fabrie P. Natural convection in a porous medium at high Rayleigh numbers. Part 1 - Darcy's model. Eur J Mech B/Fluids 1989;8:207-227.
24. Caltagirone JP, Fabrie P, Combarnous M. De la convection naturelle oscillante en milieu poreux au chaos temporel? CR Acad Sci Paris 1987;Ser II 305:549-553.
25. Caltagirone JP, Meyer G, Mojtabi A. Structural thermoconvectives tridimensionnelles dans une couche poreuse horizontale. J Mecan 1981;20:219-232.
26. Carabin G, Dassargues A. Modeling groundwater with ocean and river interaction. Water Resour Res 1999;35(8):2347-2358.
27. Chavent G, Jaffe J. Mathematical models and finite elements for reservoir simulation. New York; North Holland; 1986.
28. Cheng AHD, Quazar D. Analytical solutions. In: Bear J, Cheng AHD, Sorek S, Quazar D, Herrera I, editors. Seawater intrusion in coastal aquifers. Dordrecht: Kluwer Publ; 1999:163-191.
29. Cheng P. Heat transfer in geothermal systems. Adv Heat Transfer 1978;14:1-105.

30. Clausnitzer V, Bayer U, Fuhrmann J. Large-scale thermal-convective instability in sedimentary basins. European Geophysical Soc; Geophysical Research Abstracts HS02-02: 2001.
31. Combarnous MA, Borries SA. Hydrothermal convection in saturated porous media. Adv Hydroscience 1975;10:231-307.
32. Combarnous MA, Le Fur B. Transfert de chaleur par convection naturelle dans une couche poreuse horizontale. CR Acad Sci Paris 1969;269B:1009-1012.
33. Croucher AE, O'Sullivan MJ. The Henry problem for saltwater intrusion. Water Resour Res 1995;31(7):1809-1814.
34. Cushman JH. Dynamics of fluids in hierarchical porous media. Academic Press, London; 1990.
35. Dagan G. Flow and transport in porous formations. New York; Springer; 1989.
36. Debéda V, Caltagirone JP, Watremez P. Local multigrid refinement method for natural convection in fissured porous media. Numer Heat Transfer 1995:PartB 28:455-467.
37. Desai CS, Contractor DN. Finite element analysis of flow, diffusion, and salt water intrusion in porous media. In: Bathe KJ *et al*. editors. Formulation and comp algorithms in finite element analysis. MIT Cambridge, Massachusetts; 1977.
38. Diersch HJ. Primitive variables finite element solutions of free convection flows in porous media. Zschr Angew Math Mech (ZAMM) 1981;61:325-337.
39. Diersch HJ. Study of free convective flows in porous media and effects of mechanical dispersion using finite element methods. Gerlands Beiträge zur Geophysik 90;1981:489-506.
40. Diersch HJ. On finite element upwinding and its numerical performance in simulating coupled convective transport processes. Zschr Angew Math Mech (ZAMM) 1983;63:479-488.
41. Diersch HJ. Finite element modeling of recirculating density driven saltwater intrusion processes in groundwater. Adv Water Resour 1988;11(1):25-43.
42. Diersch HJG. A shock-capturing finite-element technique for unsaturated-saturated flow and transport problems, In: Burganos VN *et al*. editors. Computational Methods in Water Resources XII, Vol 1 Computational Methods in Contamination and Remediation of Water Resources, Southampton; Computational Mechanics Publications; 1998: 207-214.
43. Diersch HJG. Note to the opposing flow regime at mixed convection around a heated cylinder in a porous medium. Transport in Porous Media 2000;38(3):345-352.
44. Diersch, HJG. FEFLOW finite element subsurface flow and transport simulation system - User's manual/Reference manual/ White papers. Release 5.0. WASY Ltd, Berlin; 2002.
45. Diersch, HJG. Discrete feature modeling of flow, mass and heat transport processes by using FEFLOW. White Papers Vol. I, Chapter 9; WASY Ltd, Berlin; 2002:147-190.
46. Diersch, HJG. The Petrov-Galerkin least square method (PGLS). White Papers Vol. I, Chapter 13; WASY Ltd, Berlin; 2002:219-262.
47. Diersch, HJG. Consistent velocity approximation in the finite-element simulation of density-dependent mass and heat transport. White Papers Vol. I, Chapter 16; WASY Ltd, Berlin; 2002:275-306.
48. Diersch HJG, Kolditz O. On finite-element analysis of spatio-temporal buoyancy-driven convection processes in porous media. In: Kovar K, van der Heijde P. editors. Calibration and reliability in groundwater modelling, (Proceedings of the ModelCARE 96 Conference held at Golden, Colorado, September 25-27, 1996), IAHS Publ. no. 237:407-415
49. Diersch HJG, Kolditz O. Coupled groundwater flow and transport: 2. Thermohaline and 3D convection systems. Adv Water Resour 1998;21:401-425.
50. Diersch HJG, Kolditz O, Jesse J. Finite element analysis of geothermal circulation processes in hot dry rock fractures. Zschr Angew Math Mech (ZAMM) 1989;69(3):139-153.
51. Diersch HJ, Nillert P. Saltwater intrusion processes in groundwater: novel computer simulations, field studies and interception techniques. Int Symp on Groundwater Monitoring and Management 1987, Dresden, IAHS Publ, no 173; 1990:319-329.
52. Diersch HJG, Perrochet P. On the primary variable switching technique for simulating unsaturated-saturated flows. Adv Water Resour 1999;23:271-301.
53. Diersch HJ, Prochnow D, Thiele M. Finite-element analysis of dispersion-affected saltwater upconing below a pumping well. Appl Math Modelling 1984;8:305-312.
54. Donea J. A Taylor-Galerkin method for convective transport problems. Int J Numer Meth Eng 1984;20:101-119.
55. Duijn van CJ, Peletier LA, Schotting RJ. Brine transport in porous media: self-similar solutions. Adv Water Resour 1998;22(3):285-297.

56. Duijn van CJ, Schotting RJ. Brine transport in porous media: on the use of Van Mises and similarity transformations. Computational Geosciences 1998;2:125-149.
57. Durlowski LJ. Accuracy of mixed and control volume finite element approximations to Darcy velocity and related quantities. Water Resour Res 1994;30(4):965-973.
58. Elder JW. Steady free convection in a porous medium heated from below. J Fluid Mech 1967;27:29-48.
59. Elder JW. Transient convection in a porous medium. J Fluid Mech 1967;27:609-623.
60. Engelman MS, Strang G, Bathe KJ. The applications of quasi-Newton methods in fluid mechanics. Inter J Numer Meth Eng 1981;17:707-718.
61. Evans GE, Nunn JA. Free thermohaline convection in sediments surrounding a salt column. J Geophys Res 1989;94:2707-2716.
62. Fan Y, Kahawita R. A numerical study of variable density flow and mixing in porous media. Water Resour Res 1994;30(10):2707-2716.
63. Farthing MW, Miller CT. A comparison of high-resolution, finite-volume, adaptive-stencil schemes for simulating advective-dispersive transport. Adv Water Resour 2001;24(1):29-48.
64. Faust CR, Mercer JW. Theoretical analysis of fluid flow and energy transport in hydrothermal systems. US Geological Survey Open-File Report 77-69; 1977.
65. Ferziger JH, Peric M. Computational methods for fluid dynamics. Springer, Berlin; 1996.
66. Finlayson BA. Numerical methods for problems with moving fronts. Seattle; Ravenna Park Publ; 1992.
67. Fletcher CAJ. Computational techniques for fluid dynamics. Vol I and II. Berlin; Springer; 1988.
68. Fournier RO. Double-diffusive convection in geothermal systems: the Salton Sea, California, geothermal system as a likely candidate. Geothermics 1990;19(6):481-496.
69. Franca A, Haghighi K. Adaptive finite element analysis of transient thermal problems. Numer Heat Transfer Part B 1994;26:273-292.
70. Franca A, Haghighi K. Error estimate and adaptivity in finite element analysis of convective heat transfer problems, Part I: Theoretical considerations. Numer Heat Transfer Part B 1996;29:479-490, Part II: Calibration and applications. Numer Heat Transfer Part B 1996;29:491-508.
71. Frind E. Simulation of long-term transient density-dependent transport in groundwater. Adv Water Resour 1982;5:73-88.
72. Frolkovic P. Consistent velocity approximation for density driven flow and transport. In: R. Van Keer *et al*. editors. Advanced Computational Methods in Engineering, Part 2, Maastrich; Shaker Publishing; 1998:603-611.
73. Frolkovic P. d^3f documentation - the discretization. In: User's manual (compiled by E. Fein), Gesellschaft für Anlagen- und Reaktorsicherheit mbH, Braunschweig; 1998.
74. Frolkovic P, De Schepper H. Numerical modelling of convection dominated transport with density driven flow in porous media. Adv Water Resour 2001;24(1):63-72.
75. Gambolati G, Putti M, Paniconi C. Three-dimensional model of coupled density-dependent flow and miscible salt transport. In: Bear J, Cheng AHD, Sorek S, Quazar D, Herrera I, editors. Seawater intrusion in coastal aquifers. Dordrecht: Kluwer Publ; 1999:315-362.
76. Galeati G, Gambolati G, Neumann SP. Coupled and partially coupled Eulerian-Lagrangian model of freshwater-seawater mixing. Water Resour Res 1992;28:149-165.
77. Gartling DK, Hickox CE. Numerical study of the applicability of the Boussinesq approximation for a fluid-saturated porous medium. Int J Numer Methods Fluids 1985;5:995-1013.
78. Gebhart B, Jaluria Y, Mahajan RL, Sammakia B. Buoyancy-induced flows and transport. Washington: Hemisphere Publishing Cor; 1988.
79. George PL. Automatic mesh generation. Masson. J Wiley; 1991.
80. Georgiadis, JG, Catton I. Dispersion in cellular thermal convection in porous layers. Int J Heat Mass Transfer 1988;31:1081-1091.
81. Ghassemi F, Jakeman AJ, Jacobson G, Howard KWF. Simulation of seawater intrusion with 2D and 3D models: Nauru island case study. Hydrogeology J 1996;4(3):4-22.
82. Goyeau B, Songbe J-P, Gobin D. Numerical study of double-diffusive convection in a porous cavity using the Darcy-Brinkman formulation. Int J Heat Mass Transfer 1996;39:1363-1378.
83. Gray WG. Thermodynamics and constitutive theory for multiphase porous-media flow considering internal geometric constraints. Adv Water Resour 1999;22(5):521-547.

84. Gray WG, Leijnse A, Kolar RL, Blain CA. Mathematical tools for changing spatial scales in the analysis of physical systems. CRC Press, Boca Raton, Florida; 1993.
85. Green T. Scales for double-diffusive fingering in porous media. Water Resour Res 1984;20:1225-1229.
86. Gresho PM, Sani RL. Incompressible flow and the finite element method. J Wiley, Chichester; 1999.
87. Griffiths RW. Layered double-diffusive convection in porous media. J Fluid Mech 1981;102:221-248.
88. Habbar A. Direkte und inverse geochemische Mehrkomponentenmodelle (direct and inverse geochemical multispecies models). in German. PhD thesis, Institute of Fluid Mechanics, University of Hannover, Germany, forthcoming; 2001.
89. Hansen U., Yuen DA. Formation of layered structures in double-diffusive convection as applied to the geosciences. In[20]: 135-149.
90. Hassanizadeh SM. Derivation of basic equations of mass transport in porous media, Part 1. Macroscopic balance laws. Adv Water Resour 1986:9:196-206.
91. Hassanizadeh SM. Derivation of basic equations of mass transport in porous media, Part 2. Generalized Darcy's and Fick's laws. Adv Water Resour 1986;9:207-222.
92. Hassanizadeh SM. On the transient non-Fickian dispersion theory. Transport in Porous Media 1996;23:107-124.
93. Hassanizadeh SM, Gray WG. General conservation equations for multi-phase systems: 1. Averaging procedure. Adv Water Resour 1979;2(3):131-144.
94. Hassanizadeh SM, Gray WG. General conservation equations for multi-phase systems: 2. Mass, momenta, energy, and entropy equations. Adv Water Resour 1979;2(4):191-203.
95. Hassanizadeh SM, Gray WG. General conservation equations for multi-phase systems: 3. Constitutive theory for porous media flow. Adv. Water Resour 1980;3(1):25-40.
96. Hassanizadeh SM, Gray WG. Mechanics and thermodynamics of multiphase flow in porous media including interface boundaries. Adv Water Resour 1990;13:169-186.
97. Hassanizadeh SM, Leijnse A. On the modeling of brine transport in porous media. Water Resour Res 1988;24(3):321-330.
98. Hassanizadeh SM, Leijnse A. A non-linear theory of high-concentration-gradient dispersion in porous media. Adv Water Resour 1995;4:203-215.
99. Henry HR. Effects of dispersion on salt encroachment in coastal aquifers. In: Sea water in coastal aquifers. US Geol Surv, Water Supply Pap 1964;1613-C:70-84.
100. Helmig R. Multiphase flow and transport processes in the subsurface. Berlin:Springer; 1997.
101. Herbert AW, Jackson CP, Lever DA. Coupled groundwater flow and solute transport with fluid density strongly dependent on concentration. Water Resour Res 1988;24:1781-1795.
102. Herzberg A. Die Wasserversorgung einiger Nordseebäder (The water supply of parts of the North Sea coast in Germany). Z Gasbeleucht Wasserversorg 1901;44:815-819 and 1901;45:842-844.
103. Hickox GE, Gartling DK. A numerical study of natural convection in a horizontal porous layer subjected to an end-to-end temperature difference. J Heat Transfer 1981;103:797-802.
104. Holst PH, Aziz K. Transient three-dimensional natural convection in confined porous media. Int J Heat Mass Transfer 1972;15:73-90.
105. Holstad A. Temperature-driven fluid flow in porous media using a mixed finite element method and a finite volume method. Adv Water Resour 2001;24(8):843-862.
106. Holzbecher E. Modeling of saltwater upconing. In: Wang S, editor. II. Int Conf Hydro-Science and Hydro-Engin, Proc Vol 2, Part A, Beijing 1995:858-865.
107. Holzbecher E. Modeling density-driven flow in porous media. Berlin: Springer; 1998.
108. Holzbecher E. Comments on 'Constant-concentration boundary condition: Lessons from the HYDROCOIN variable-density groundwater benchmark problem' by Konikow LF, Sanford WE, Campbell PJ. Water Resour Res 1998;34(10):2775-2778.
109. Holzbecher E., Yusa Y. Numerical experiments on free and forced convection in porous media. Int J Heat Mass Transfer 1995;11:2109-2115.
110. Horne RN. Three-dimensional natural convection in a confined porous medium heated from below. J Fluid Mech 1979;92:751-766.
111. Horne RN, Caltagirone JP. On the evolution of thermal disturbances during natural convection in a porous medium. J Fluid Mech 1980;100:385-395.
112. Horne RN, O'Sullivan MJ. Oscillatory convection in a porous medium heated from below. J Fluid Mech 1974;66:339-352.

113. Horne RN, O'Sullivan MJ. Origin of oscillatory convection in a porous medium heated from below. Phys Fluids 1978;21:1260-1264.
114. Horton CW, Rogers, FT. Convective currents in a porous medium. J. Appl Phys 1945;16:367-370.
115. Huyakorn PS, Pinder GF. Computational methods in subsurface flow. Academic Press, San Diego; 1983.
116. Huyakorn PS, Taylor C. Finite element models for coupled groundwater flow and convective dispersion. In: Gray WG *et al*., editors. Proc. 1st Int Conf Finite Elements in Water Resour 1976; Princeton Univ, Pentech Press, London:1.131-1.151.
117. Huyakorn PS, Anderson PF, Mercer JW, White Jr HO. Saltwater intrusion in aquifers: development and testing of a three-dimensional finite element model. Water Resour Res 1987;23:293-312.
118. Johannsen K, Kinzelbach W, Oswald S, Wittum G. The saltpool benchmark problem - numerical simulation of saltwater upconing in a porous medium. Adv Water Resour 2002;25(3):335-348.
119. Johns RT, Rivera A. Comment on 'Dispersive transport dynamics in a strongly coupled groundwater-brine flow system' by Oldenburg CM, Pruess K. Water Resour Res 1996;32(11):3405-3410.
120. de Josselin de Jong G. Singularity distributions for the analysis of multiple-fluid flow through porous media. J Geophys Res 1960;65(11):3739-3758.
121. Kaiser R. Gitteradaption für gekoppelte Prozesse in klüftig-porösen Medien. PhD thesis, No. 63, Institute of Fluid Mechanics, University of Hannover, Germany; 2001.
122. Katto Y, Masuoka T. Criterion for the onset of convective flow in a fluid in a porous medium. Int J Heat Mass Transfer 1967;10:297-309.
123. Kimura S, Schubert G, Straus JM. Route to chaos in porous-medium thermal convection. J Fluid Mech 1986;166:305-324.
124. Kolditz O. Strömung, Stoff- und Wärmetransport im Kluftgestein (flow, contaminant and heat transport in fractured rock). in German. Gebr. Borntraeger, Berlin; 1997.
125. Kolditz O. Computational methods in environmental fluid mechanics. Berlin; Springer: 2002.
126. Kolditz O, Ratke R, Diersch HJG, Zielke W. Coupled groundwater flow and transport: 1. Verification of variable-density flow and transport models. Adv Water Resour 1998;21:27-46.
127. Kolditz O, Habbar A, Kaiser R, Rother T, Thorenz C. ROCKFLOW - theory and user's manual. Release 3.6, Institute of Fluid Mechanics, University of Hannover, Germany; 2001.
128. Konikow LF, Reilly TE. Seawater intrusion in the United States. In: Bear J, Cheng AHD, Sorek S, Quazar D, Herrera I, editors. Seawater intrusion in coastal aquifers. Dordrecht: Kluwer Publ; 1999:463-506.
129. Konikow LF, Sanford WE, Campbell PJ. Constant-concentration boundary condition: Lessons from the HYDROCOIN variable-density groundwater benchmark problem. Water Resour Res 1997;33(10):2253-2261.
130. Kimura S, Schubert G, Straus JM. Instabilities of steady, periodic and quasi-periodic modes of convection in porous media. ASME J Heat Transfer 1987;109:350-355.
131. Knabner P, Frolkovic P. Consistent velocity approximation for finite volume or element discretizations of density driven flow in porous media. In: Aldama AA *et al*, editors. Computational Methods in Water Resources XI, Vol 1 - Computational Methods in Subsurface Flow and Transport Problems, Southampton: Computational Mechanics Publications; 1996:93-100.
132. Kvernvold O, Tyvand PA. Nonlinear thermal convection in anisotropic porous media. J Fluid Mech 1979;90:609-624.
133. Kvernvold O, Tyvand PA. Dispersion effects on thermal convection in porous media. J Fluid Mech 1980;99:673-686.
134. Kvernvold O, Tyvand PA. Dispersion effects on thermal convection in a Hele-Shaw cell. Int J Heat Mass Transfer 1981;24:887-890.
135. Lahm TD, Bair ES, VanderKwaak J. Role of salinity-derived variable-density flow in the displacement of brine from a shallow, regionally extensive aquifer. Water Resour Res 1998;34(6):1469-1480.
136. Lapwood ER. Convection in a fluid in a porous medium. Proc Cambridge Phil Soc 1948;44:508-521.
137. Leijnse A. Three-dimensional modeling of coupled flow and transport in porous media. PhD thesis, University of Notre Dame, Indiana; 1992.
138. Leijnse A. Comparison of solution methods for coupled flow and transport in porous media. In: Peters A *et al*. editors. Computational Methods in Water Resources X. Vol 1, Dordrecht; Kluwer Acad Publ, 1994: 489-496.
139. Leijnse A, Oostrom M. The onset of instabilities in the numerical simulation of density-driven flow in porous media. In: Rus-

sell TF *et al*. editors. Computational Methods in Water Resources IX. Vol 2, Mathematical Modeling in Water Resources, London; Elsevier, 1992: 273-280.

140. Lever DA, Jackson CP. On the equations for the flow of concentrated salt solution through a porous medium. UK DOE Report No DOE/RW/85.100; 1985.
141. Löhner R. Applied computational fluid dynamics techniques. J Wiley, Chichester; 2001.
142. Mackinnon RJ, Carey GF. Superconvergent derivatives: a Taylor series analysis. Int J Numer Methods Eng 1989;28:489-509.
143. Marsily de G. Quantitative hydrogeology. Academic Press; 1981.
144. Mazzia A, Bergamaschi L, Putti M. On the reliability of numerical solutions of brine transport in groundwater: analysis of infiltration from a salt lake. Transport in Porous Media 2001;43(1):65-86.
145. McKibbin R, O'Sullivan MJ. Onset of convection in a layered porous medium heated from below. J Fluid Mech 1980;96:375-393.
146. McKibbin R, O'Sullivan MJ. Heat transfer in layered porous medium heated from below. J Fluid Mech 1981;111:141-173.
147. McKibbin R, Tyvand PA. Anisotropic modelling of thermal convection in multilayered porous media. J Fluid Mech 1982;118:315-339.
148. McKibbin R, Tyvand PA. Thermal convection in a porous medium composed of alternating thick and thin layers. Int J Heat Mass Transfer 1983;26:761-780.
149. McKibbin R, Tyvand PA. Thermal convection in a porous medium with horizontal tracks. Int J Heat Mass Transfer 1984;27:1007-1023.
150. Miller CT, Christakos G, Imhoff PT, McBride JF, Pedit JA, Trangenstein JA. Multiphase flow and transport modeling in heterogeneous porous media: challenges and approaches. Adv Water Resour 1998;21(2):77-120.
151. Murray BT, Chen CF. Double-diffusive convection in a porous medium. J Fluid Mech 1989;201:147-166.
152. Neuman SP. A Eulerian-Lagrangian numerical scheme for the dispersion convection equation using conjugate space time grids. J Comput Phys 1981;41(2):270-291.
153. Nield DA. Onset of thermohaline convection in a porous medium. Water Resour Res 1968;11:553-560.
154. Nield DA. The stability of convective flows in porous media. In: Kakac S, Kilkis B, Kulacki FA, Arinc F, editors. Convective heat and mass transfer in porous media. Dordrecht: Kluwer Publ; 1990:79-122.
155. Nield DA. Estimation of an effective Rayleigh number for convection in a vertically inhomogeneous porous medium or clear fluid. Int J Heat Fluid Flow 1994;15:337-340.
156. Nield DA. Some pitfalls in the modelling of convective flows in porous media. Transport in Porous Media 2001;43(3):597-601.
157. Nield DA, Bejan A. Convection in porous media. New York: Springer; 2nd edition;1999.
158. Nishikawa T. Testing alternative conceptual models of seawater intrusion in a coastal aquifer using computer simulation, southern California, USA. Hydrogeology J 1997;5(3):60-74.
159. Oden JT. Error estimation and control in computational fluid dynamics. In: Whiteman JR, editor. The mathematics of finite elements and applications- Highlights 1993. Chichester: J Wiley; 1994:1-23.
160. Oden JT, Bass JM, Huang CY, Berry CW. Recent results on smart algorithms and adaptive methods for two- and three-dimensional problems in computational fluid mechanics. Comput Structures 1990;35:381-396.
161. Oldenburg CM, Pruess K. Dispersive transport dynamics in a strongly coupled groundwater-brine flow system. Water Resour Res 1995;31:289-302.
162. Oldenburg CM, Pruess K. Layered thermohaline convection in hypersaline geothermal systems. Transport in Porous Media 1998;33(1/2):29-63.
163. Oldenburg CM, Pruess K, Travis BJ. Reply to: Comment on 'Dispersive transport dynamics in a strongly coupled groundwater-brine flow system' by Johns RT, Rivera A. Water Resour Res 1996;32(11):3411-3412.
164. Oltean C, Bués MA. Coupled groundwater flow and transport in porous media. A conservative or non-conservative form? Transport in Porous Media 2001;44(2):219-246.
165. Onate E, Bugeda G. Mesh optimality criteria for adaptive finite element computations. In: Whiteman JR, editor. The mathematics of finite elements and applications- Highlights 1993. Chichester: J Wiley; 1994:121-135.
166. Ophori DU. Flow of groundwater with variable density and viscosity, Atikokan research area, Canada. Hydrogeology J 1998;6(2):193-203.

167. Oswald SE. Dichteströmungen in porösen Medien: Dreidimensionale Experimente und Modellierungen (Density driven flows in porous media: three-dimensional experiments and modeling). Dissertation ETH Zurich, Switzerland; 1998.
168. Oswald SE, Scheidegger MB, Kinzelbach W. A three-dimensional physical benchmark test for verification of variable-density flow models. Water Resour Res 2000; submitted.
169. Oude Essink GHP. Salt water intrusion in a three-dimensional groundwater system in the Netherlands: a numerical study. Transport in Porous Media 2001;43(1):137-158.
170. Palliser C, McKibbin R. A model for deep geothermal brines, I. T-p-X state-space description. Transport in Porous Media 1998;33(1/2):65-80.
171. Palliser C, McKibbin R. A model for deep geothermal brines, II. thermodynamic property - density. Transport in Porous Media 1998;33(1/2):129-154.
172. Palliser C, McKibbin R. A model for deep geothermal brines, III. thermodynamic properties - enthalpy and viscosity. Transport in Porous Media 1998;33(1/2):155-171.
173. Paniconi C, Khlaifi I, Lecca G, Giacomelli A, Tarhouni J. Modeling and analysis of seawater intrusion in the coastal aquifer of Eastern Cap-Bon, Tunisia. Transport in Porous Media 2001;43(1):3-28.
174. Patankar SV, Karki KC, Kelkar KM. Finite volume method. In: Johnson RW, editor. The handbook of fluid dynamics, Chapter 27. CRC Press, Springer; 1998.
175. Perrochet P. A streamline-upwind-full-Galerkin method for space-time convection dominated transport problems. Int J Num Meth Eng 1993;36:4165-4183.
176. Perrochet P, Azérad P. Space-time integrated least-squares: solving a pure advection equation with a pure diffusion operator. J Comput Phys 1995;117:183-193.
177. Perrochet P, Bérod D. Stability of the standard Crank-Nicolson-Galerkin scheme applied to the diffusion-convection equation: some new insights. Water Resour Res 1993;29(9)3291-3297.
178. Perrochet P, Tacher L. Mathematical modeling of hydro-thermal processes in Mururoa Atoll. Research Report GEOLEP-EPFL-DGC, Univ. Lausanne, Switzerland; 1997.
179. Pinder GF, Cooper HH. A numerical technique for calculating the transient position of the saltwater front. Water Resour Res 1970;6(3):875-882.
180. Prasad V, Kladias N. Non-Darcy natural convection in saturated porous media. In: Kakac S, Kilkis B, Kulacki FA, Arinc F, editors. Convective heat and mass transfer in porous media. Dordrecht: Kluwer Publ; 1990:173-224.
181. Prax C, Sadat H, Salagnac P. Diffuse approximation method for solving natural convection in porous media. Transport in Porous Media 1996;22(2):215-223.
182. Putti M, Paniconi C. Picard and Newton linearization for the coupled model of saltwater intrusion in aquifer. Adv Water Resour 1995;18(3):159-170.
183. Raviart PA, Thomas JM. A mixed finite element method for the second order elliptic problems. In: Mathematical Aspects of the Finite Element Method, Lect Notes Math, New York: Springer; 1977:292-315.
184. Reddy JN, Gartling DK. The finite element method in heat transfer and fluid dynamics. 2nd edition. CRC Press, Boca Raton; 2001.
185. Reilly TE, Goodman AS. Quantitative analysis of saltwater-freshwater relationships in groundwater systems - A historical perspective. J Hydrology 1985;80:125-160.
186. Reilly TE, Goodman AS. Analysis of saltwater upconing beneath a pumping well. J Hydrology 1987;89:169-204.
187. Riley DS, Winters KH. Modal exchange mechanisms in Lapwood convection. J Fluid Mech 1989;204:325-358.
188. Rubin H. Onset of thermohaline convection in a cavernous aquifer. Water Resour Res 1976;12:141-147.
189. Rubin H, Roth C. On the growth of instabilities in groundwater due to temperature and salinity gradients. Adv Water Resour 1979;2:69-76.
190. Rubin H, Roth C. Thermohaline convection in flowing groundwater. Adv Water Resour 1983;6:146-156.
191. Sanford WE, Konikow LF. A two constituent solute transport model for groundwater having variable density. US Geol Surv Water Resour Invest 1985; 85-4279: 88 pp.
192. Sarler B, Gobin D, Goyeau B, Perko J, Power H. Natural convection in porous media - dual reciprocity boundary element method solution of the Darcy model. Int J Numer Meth Fluids 2000;33:279-312.
193. Schincariol RA. Dispersive mixing dynamics of dense miscible plumes: natural perturbation initiation by local-scale heterogeneities. J Contam Hydrol 1998;34:247-271.

194. Schincariol RA, Schwartz FW. An experimental investigation of variable density flow and mixing in homogeneous and heterogeneous media. Water Resour Res 1990;26(10):2317-2329.
195. Schincariol RA, Schwartz FW, Mendoza CA. On the generation of instabilities in variable density flow. Water Resour Res 1994;30(4):913-927.
196. Schincariol RA, Schwartz FW, Mendoza CA. Instabilities in variable density flows: stability and sensitivity analyses for homogeneous and heterogeneous media. Water Resour Res 1997;33(1):31-41.
197. Schneider KJ. Investigation on the influence of free thermal convection on heat transfer through granular material. Proc 11th Int Cong of Refrigeration. Oxford: Pergamon Press; Paper 11-4,1963:247-253.
198. Schotting RJ, Moser H, Hassanizadeh SM. High-concentration-gradient dispersion in porous media: Experiments, analysis and approximations. Adv Water Resour 1999;22:665-680.
199. Schubert G, Straus JM. Three-dimensional and multicellular steady and unsteady convection in fluid-saturated porous media at high Rayleigh numbers. J Fluid Mech 1979;94:25-38.
200. Schubert G, Straus JM. Transitions in time-dependent thermal convection in fluid-saturated porous media. J Fluid Mech 1982;121:301-313.
201. Segol G. Classic groundwater simulations - Proving and improving numerical models. Englewood Cliffs; PTR Prentice Hall; 1994.
202. Segol G, Pinder GF. Transient simulation of saltwater intrusion in southeastern Florida. Water Resour Res 1976;12(1):65-70.
203. Segol G, Pinder GF, Gray WG. A Galerkin-finite element technique for calculating the transient position of the saltwater front. Water Resour Res 1975;11(2):343-347.
204. Sherif MM. Nile delta aquifer in Egypt. In: Bear J, Cheng AHD, Sorek S, Quazar D, Herrera I, editors. Seawater intrusion in coastal aquifers. Dordrecht: Kluwer Publ; 1999:559-590.
205. Sherif MM, Hamza KI. Mitigation of seawater intrusion by pumping brackish water. Transport in Porous Media 2001;43(1):29-44.
206. Simmons CT, Fenstemaker TR, Sharp Jr JM. Variable-density groundwater flow and solute transport in heterogeneous media: approaches, resolutions and future challenges. J Contam Hydrol 2001; submitted.
207. Simmons CT, Narayan KA, Wooding RA. On a test case for density-dependent groundwater flow and solute transport models: the salt lake problem. Water Resour Res 1999;35(12):3607-3620.
208. Simmons CT, Pierini ML, Hutson JL. Laboratory investigation of variable-density flow and solute transport in unsaturated-saturated porous media. Transport in Porous Media 2001; in press.
209. Sorek S, Borisov V, Yakirevich A. A two-dimensional areal model for density dependent flow regime. Transport in Porous Media 2001;43(1):87-105.
210. Spena FR, Vacca A. A potential formulation of non-linear models of flow through anisotropic porous media. Transport in Porous Media 2001;45(3):407-423.
211. Strack ODL. Groundwater mechanics. Englewood; Prentice Hall; 1989.
212. Straus JM. Large amplitude convection in porous media. J Fluid Mech 1974;64:51-63.
213. Straus JM, Schubert G. Three-dimensional convection in a cubic box of fluid-saturated porous material. J Fluid Mech 1979;91:155-165.
214. Straus JM, Schubert G. Modes of finite-amplitude three-dimensional convection in rectangular boxes of fluid-saturated porous material. J Fluid Mech 1981;103:23-32.
215. Taunton JW, Lightfoot EN, Green T. Thermohaline instability and salt fingers in a porous medium. Phys Fluids 1972;15:748-753.
216. Taylor A, Hulme P, Hughes A, Foot S. Benchmarking of variable model codes against Henry's problem. First Intern Conf on saltwater intrusion in coastal aquifers - monitoring, modeling and management. Essaouira, Marocco, April 23-25; 2001.
217. Thiele K. Adaptive finite volume discretization of density driven flows in porous media. PhD thesis, Institute of Applied Mathematics, University of Erlangen-Nürnberg, Germany; 1999.
218. Thorenz C. Model adaptive simulation of multiphase and density driven flow in fractured and porous media. PhD thesis, No. 62, Institute of Fluid Mechanics, University of Hannover, Germany; 2001.
219. Thorenz C, Kosakowski G, Kolditz O, Berkowitz B. An experimental and numerical investigation of saltwater movement in partially saturated systems. Water Resour Res 2001; submitted.

220. Tien CL, Vafai K. Convective and radiative heat transfer in porous media. Adv Applied Mech 1990;27:225-281.
221. Trevisan OV, Bejan A. Natural convection with combined heat and mass transfer buoyancy effects in a porous medium. Int J Heat Mass Transfer 1985;28(8)1597-1611.
222. Turner JS. Buoyancy effects in fluids. Chapter 8, Cambridge Univ. Press, Cambridge; 1973.
223. Turner JS. Laboratory models of double-diffusive processes. In[20]: 11-29.
224. Tyvand PA. Thermohaline instability in anisotropic porous media. Water Resour Res 1980;16:325-330.
225. Uchiyama Y, Nadaoka K, Rölke P, Adachi K, Yagi H. Submarine groundwater discharge into the sea and associated nutrient transport in a sandy beach. Water Resour Res 2000;36(6):1467-1479.
226. Vadasz P. Local and global transitions to chaos and hysteresis in a porous layer heated from below. Transport in Porous Media 1999;37(2):213-245.
227. Vadasz P, Olek S. Weak turbulence and chaos for low Prandtl number gravity driven convection in porous media. Transport in Porous Media 1999;37(1):69-91.
228. Vadasz P, Olek S. Computational recovery of the homoclinic orbit in porous media convection. Int J Nonlinear Mech 1999;34:89-93.
229. Vadasz P, Olek S. Route to chaos for moderate Prandtl number convection in a porous layer heated from below. Transport in Porous Media 2000;41(2):211-239.
230. Volker RE, Rushton KR. An assessment of the importance of some parameters for seawater intrusion and a comparison of dispersive and sharp-interface modeling approaches. J Hydrol 1982;56:239-250.
231. Voss CI. A finite-element simulation model for saturated-unsaturated fluid-density-dependent ground-water flow with energy transport or chemically-reactive single-species solute transport. US Geol Surv, Water Resour Invest 1984; Rep 84-4369:409pp.
232. Voss CI. USGS SUTRA Code - History, practical use, and application in Hawaii. In: Bear J, Cheng AHD, Sorek S, Quazar D, Herrera I, editors. Seawater intrusion in coastal aquifers. Dordrecht: Kluwer Publ; 1999:249-313.
233. Voss CI, Souza WR. Variable density flow and solute transport simulation of regional aquifers containing a narrow freshwater-saltwater transition zone. Water Resour Res 1987;26:2097-2106.
234. Walker K, Homsy GM. A note on convective instabilities in Boussinesq fluids and porous media. ASME J Heat Transfer 1977;99:338-339.
235. Watson SJ, Barry DA, Schotting RJ, Hassanizadeh SM. On the validity of Darcy's law for stable high-concentration displacements in granual porous media. Transport in Porous Media - Special Issue 2002;47(2), forthcoming.
236. Watson SJ, Barry DA, Schotting RJ, Hassanizadeh SM. Validation of classical density-dependent solute transport theory for stable high-concentration-gradient brine displacements in coarse and medium sands. Adv Water Resour 2002, forthcoming.
237. Weatherill NP. Generalised mesh and adaptivity techniques for computational fluid dynamics. In: Onate E *et al*, editors. Finite elements in the 90's. Barcelona: Springer/CIMNE; 1991:398-409.
238. Wiek J, Person M, Strayer L. A finite element method for simulating fault block motion and hydrothermal fluid flow within rifting basins. Water Resour Res 1995;31(12):3241-3258.
239. Whitaker S. The Forchheimer equation: a theoretical development. Transport in Porous Media 1996;25(1):27-61.
240. Whitaker S. The method of volume averaging. Dordrecht: Kluwer Publ; 1999.
241. Wooding, RA. Steady state free thermal convection of liquid in a saturated permeable medium. J Fluid Mech 1957;2:273-285.
242. Wooding RA, Tyler SW, White I. Convection in groundwater below an evaporating salt lake, 1, Onset of instability. Water Resour Res 1997;33(6):1199-1217.
243. Wooding RA, Tyler SW, White I, Anderson PA. Convection in groundwater below an evaporating salt lake, 2, Evolution of fingers or plumes. Water Resour Res 1997;33(6):1219-1228.
244. Xue Y, Xie C, Wu J, Liu P, Wang J, Jiang Q. A three-dimensional miscible transport model for seawater intrusion in China. Water Resour Res 1995;31(4):903-912.
245. Yeh GT. On the computation of Darcian velocity and mass balance in the finite element modelling of groundwater flow. Water Resour Res 1981;17(5):1529-1534.
246. Younes A, Ackerer P, Mosé R. Modeling variable density flow and solute transport in porous medium: 2. Re-evaluation of the

salt dome flow problem. Transport in Porous Media 1999;35(3):375-394.

247. Zienkiewicz OC, Taylor RL. The finite element method. Vol 1 and 2, McGraw-Hill, London; 1989 and 1991.
248. Zienkiewicz OC, Zhu JZ. A simple error estimator and adaptive procedure for practical engineering analysis. Int J Num Meth Eng 1987;24:337-357.
249. Zienkiewicz OC, Zhu JZ. The superconvergent patch recovery and a-posteriori error estimates. Part 1: The recovery technique. Int J Numer Meth Eng 1992;33:1331-1364. Part 2: Error estimates and adaptivity. Int J Numer Meth Eng 1992;33:1365-1382.

1. Variable-density flow and transport in porous media: approaches and challenges

Subject Index

U

V

W

Subject Index

Author Index

Author Index